UNIVERSITY OF CALIFORNIA
RIVERSIDE

Electronic Transport Studies of Diamond and Diamond-on-Graphene Heterostructures and Potential Device Applications

A Dissertation submitted in partial satisfaction
of the requirements for the degree of

Doctor of Philosophy

in

Physics

by

Adrian Nosek

December 2019

Dissertation Committee:

Prof. Marc Bockrath, Co-Chairperson
Prof. Shan-Wen Tsai, Co-Chairperson
Prof. Naveen Reddy

The Dissertation of Adrian Nosek is approved:

Committee Co-Chairperson

Committee Co-Chairperson

University of California, Riverside

Acknowledgments

First and foremost, I would like to thank my advisor Marc Bockrath for giving me the opportunity to work in his lab. Marc has been a constant source of knowledge that has helped me through my journey of gradschool. I would like to thank Juan and Dexter who both have introduced me into the intricacies of working in a cleanroom. Without the help of those two, the learning curve in the cleanroom would have been considerably slower. Furthermore I would like to thank all my classmates and labmates and friend that have participated through my journey of grad school. Thanks to Oleg, Yong, Bin, Yi, Cheng, Tengfei, Peng, Sean, Lukasz for being great labmates. Thanks to Chris, Max, Nate, Petr, Oleg, Jack and Jasmine and all the rest of my classmates and friend for being supportive and understanding of the intense amount of work that grad school has been for me.

To my mom,

to my brother,

to my family, and my friends,

thank you for making this happen.

ABSTRACT OF THE DISSERTATION

Electronic Transport Studies of Diamond and Diamond-on-Graphene Heterostructures and Potential Device Applications

by

Adrian Nosek

Doctor of Philosophy, Graduate Program in Physics
University of California, Riverside, December 2019
Prof. Marc Bockrath, Co-Chairperson
Prof. Shan-Wen Tsai, Co-Chairperson

This dissertation investigated the electronic transport properties of diamond and diamond-on-graphene heterostructures. I obtained three main results during the course of my studies, one regarding the electronic transport in polycrystalline diamond films, and two regarding its potential device applications. First, I observed dissipative quantum tunneling in lowly boron-doped polycrystalline diamond by collapse of current-voltage characteristics onto a single curve, exhibiting universal scaling behavior. One of our main outcomes was the observation of a quasi-classical to quantum transition of the transport behavior of localized charge carriers within a series of quantum wells. Within our experiment, quantum mechanical tunneling was mediated by a composite quasiparticle, consisting of an instanton and anti-instanton, referred to as the bounce solution within this quantum field theoretical tunneling model. Second, I realized the first diamond-on-graphene barristor, which exhibits an optimal operation behavior between room temperature and 100°C. At room temperature the tunability of the Schottky barrier is the largest, but with increasing temperature

the tunability degrades and is eventually lost. At 100°C the diode characteristics of the diamond-graphene interface is most clearly pronounced. My work layed out the first steps towards high temperature diamond and graphene based electronics for high power switching applications. Third, I fabricated the first diamond-based memristor which acts as an inorganic synapse. My diamond-based memristive inorganic synapse showed effects of a psychological human memory model with filtering, learning, remembering and forgetting of incoming signals. Spike-timing dependent plasticity in our inorganic synapse displayed the frequency dependent effect on learning. Last but not least, I observed that my inorganic synapse mimicks a refractory period commonly observed when neurons fire off action potentials between neuron cells. My diamond-based memristor has potential device applications in neuromorphic computing for novel non-traditional computer architectures for in-memory information processing.

Contents

List of Figures

List of Tables

Chapter 1

Introduction into Graphene and Diamond

1.1 Graphene: Lattice and Bandstructure

Graphene's Lattice

Graphene is a two-dimensional, one atom thick, single layer of carbon atoms. It was for the first time isolated and identified in 2004 by Geim and Novoselov [1]. This discovery very quickly resulted in the Noble Prize of physics in 2010 by the Swedish academy of sciences, mainly due to the rich physics in graphene and its widereached potential applications not only in electronics but also in chemistry and biotechnology.

Carbon is the sixth element in the periodic table and has 6 electrons distributed in the s- and p-orbitals in a $1s^2 2s^2 2p^2$ configuration. The carbon atoms of graphene are arranged in a triangular Bravais lattice, also called hexagonal lattice, with two atoms in

its unit cell and sp^2 hybridized interatomic bonds [2]. The length of the unit vector of the triangular lattice is $\mid \vec{a}_1 \mid = \mid \vec{a}_2 \mid = \sqrt{3}\ 0.142$ nm=0.246 nm and the length of the interatomic bond is 0.142 nm. Each carbon atom has 3 nearest neighbours arranged in a trigonal planar geometry with a bond angle of 60° between any two neighbouring bonds. Figure 1.1 shows the graphene real space lattice with its lattice vectors $\vec{a}_1$ and $\vec{a}_2$ to left. To the right it shows its reciprocal lattice with high symmetry points K, K' and Γ.

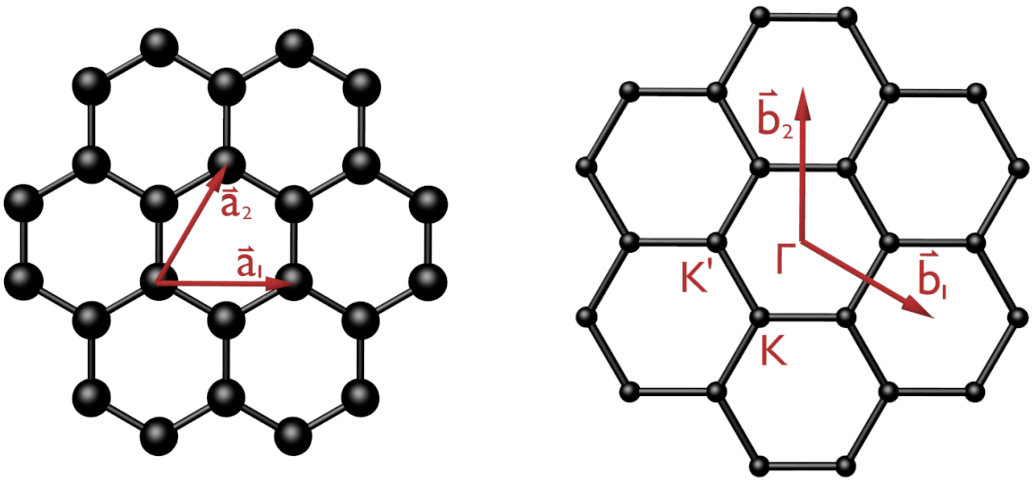

Figure 1.1: Real space and reciprocal lattice of graphene. Left: Real space lattice of graphene with its lattice vectors $\vec{a}_1$ and $\vec{a}_2$. Right: Reciprocal lattice of graphene with high symmetry points K, K' and Γ and reciprocal lattice vectors $\vec{b}_1$ and $\vec{b}_2$.

The lattice vectors $\vec{a}_1$, $\vec{a}_2$ and the recirpocal lattice vectors $\vec{b}_1$, $\vec{b}_2$ satisfy orthonormality $\vec{a}_i \cdot \vec{b}_j = 2\pi\delta_{ij}$, where δ_{ij} is the Kronecker delta, and are given as

$$\vec{a}_1 = a \begin{pmatrix} 1 \\ 0 \end{pmatrix} , \vec{a}_2 = \frac{a}{2} \begin{pmatrix} 1 \\ \sqrt{3} \end{pmatrix} , \vec{b}_1 = \frac{2\pi}{\sqrt{3}a} \begin{pmatrix} \sqrt{3} \\ -1 \end{pmatrix} , \vec{b}_2 = \frac{4\pi}{\sqrt{3}a} \begin{pmatrix} 0 \\ 1 \end{pmatrix} \tag{1.1}$$

Linear combinations of lattice vectors $\vec{a}_1$ and $\vec{a}_2$ give access to any point of graphene's triangular lattice. At each point of the triangular lattice, graphene's unit cell will be attached, where the positions of the unit cell's atoms are $\vec{0}$ and $d \cdot \hat{\mathbf{y}}$, with $\hat{\mathbf{y}}$ the unit vector in y direction.

Graphene's Bandstructure

Electronic charge transport in graphene occurs through delocalized π charge carriers originating from p_z orbitals of the lattice. Graphene's electronic band structure can be derived from a tight-binding Hamiltonian approach with nearest neighbour hopping transport. The eigenenergies derived from diagonalizing the tight-binding Hamiltonian are given by

$$\varepsilon(k_x, k_y) = \pm t\sqrt{1 + 4\cos\left(\frac{\sqrt{3}k_x a}{2}\right)\cos\left(\frac{k_y a}{2}\right) + 4\cos^2\left(\frac{k_y a}{2}\right)} \tag{1.2}$$

where t is the hopping energy with t $\simeq$ 2.7 eV, k_x and k_y are the reciprocal space lattice vectors, and a is the lattice constant with $a = \sqrt{3}c = 0.246$ nm where c is the inter carbon distance of length 0.142 nm.

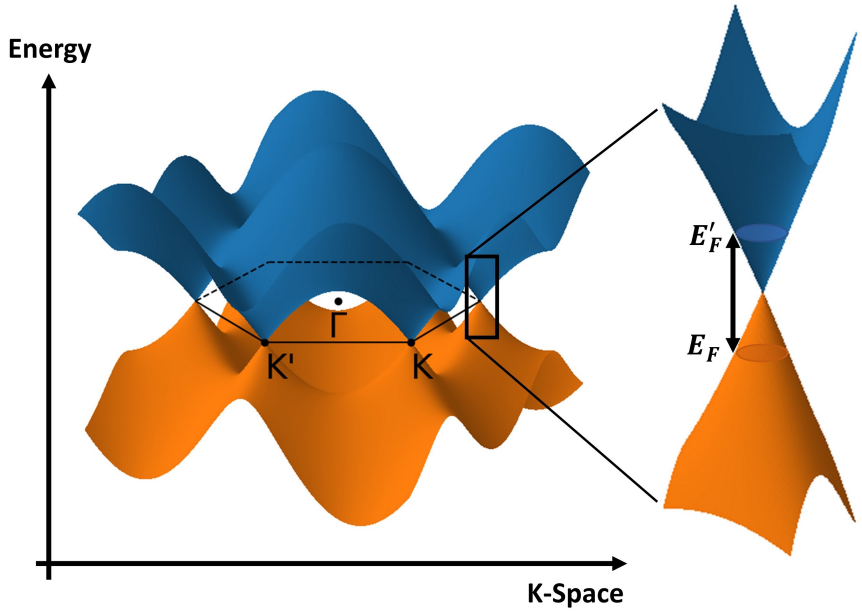

Figure 1.2: Left: Bandstructure of graphene. Right: Enlarged structure of a Dirac cone at the K' point. The position of the Fermi level can be tuned between different positions E_F and E'_F through an external electric field.

The K and K' point at the edge of the Brillouin zone of the band structure exhibit a cone like structure that precisley intersects at K and K', widely known as the Dirac point. It is for this Dirac cone that graphene is referred as a gapless semimetal. A plot of the eigenenergies is presented in figure 1.2. Interestingly, the Fermi energy of graphene can be placed below or above the Dirac point by applying an external gate electric field, thereby effectively choosing whether electrons or holes are the conductive charge carriers of the system.

1.2 Single Crystal Diamond: Lattice, Bandstructure and Impurities

Diamond's Lattice

Single crystal diamond, just like graphene, solely consists of carbon atoms. Unlike graphene, single crystal diamond forms sp^3 hybridized bonds between carbon atoms. Each carbon atom has 4 nearest neighbours forming, a tetrahedral bond geometry with a bond angle of 109.47° between any two neighbouring bonds.

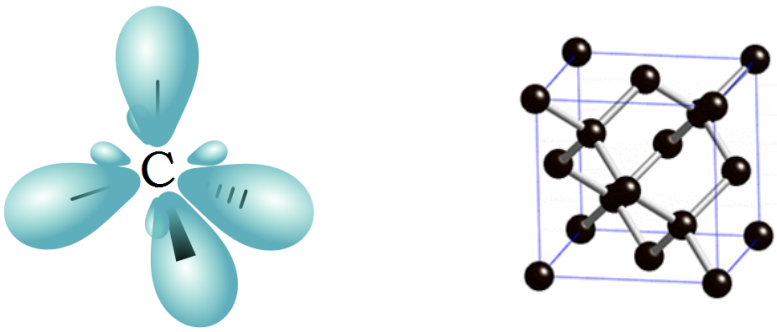

Figure 1.3: Left: Carbon-carbon sp^3 hybridization in diamond [3]. Middle: Diamond lattice structure [4].

The length of the bonds is 0.154 nm. Single crystal diamond has a 3-dimensional lattice structure. A face centered cubic (fcc) lattice is positioned at the origin and another fcc lattice is positioned at one fourth of the first cubes diagonal at a/4 $(\hat{\mathbf{x}} + \hat{\mathbf{y}} + \hat{\mathbf{z}})$, where a is the length of the cube edge and $(\hat{\mathbf{x}} + \hat{\mathbf{y}} + \hat{\mathbf{z}})$ are the coordinate unit vectors, see figure 1.3. In other words, one can describe the diamond lattice as a fcc lattice with a 2 point basis. The two positions of the diamond's unit cell atoms are $\vec{0}$ and a/4 $(\hat{\mathbf{x}} + \hat{\mathbf{y}} + \hat{\mathbf{z}})$. The primitive lattice vectors $\vec{a}_1$ and $\vec{a}_2$ and $\vec{a}_3$ are positioned at the faces of the fcc lattice and are given by

$$\vec{a}_1 = \frac{a}{2}\begin{pmatrix} 1 \\ 1 \\ 0 \end{pmatrix}, \vec{a}_2 = \frac{a}{2}\begin{pmatrix} 1 \\ 0 \\ 1 \end{pmatrix}, \vec{a}_3 = \frac{a}{2}\begin{pmatrix} 0 \\ 1 \\ 1 \end{pmatrix}. \tag{1.3}$$

Diamond's Bandstructure

Undoped single crystal diamond is a wide bandgap insulator and optically transparent. At room temperature its indirect and direct bandgap are 5.47 eV and 5.8 eV, respectively. For simplicity, only a schematics of the bandstructure is shown in figure 1.4. A in-depth band structure diagram can be found in [5, 6]. It is possible to incorporate impurities into the diamond lattice and effectively dope diamond from insulating to semiconductive to metallic to superconducting behavior. Impurities can be either of acceptor (p-type) or donor (n-type) nature. Most prominently diamond can be doped with boron, its slightly smaller and lighter neighbour element in the periodic table. Boron acts as an acceptor in diamond with an actication energy positioned around 0.37 eV above the valence band [7], as shown in the right of figure 1.4. In an atomistic picture it captures an electron

from the neighbouring carbon and creates a hole for charge transport.

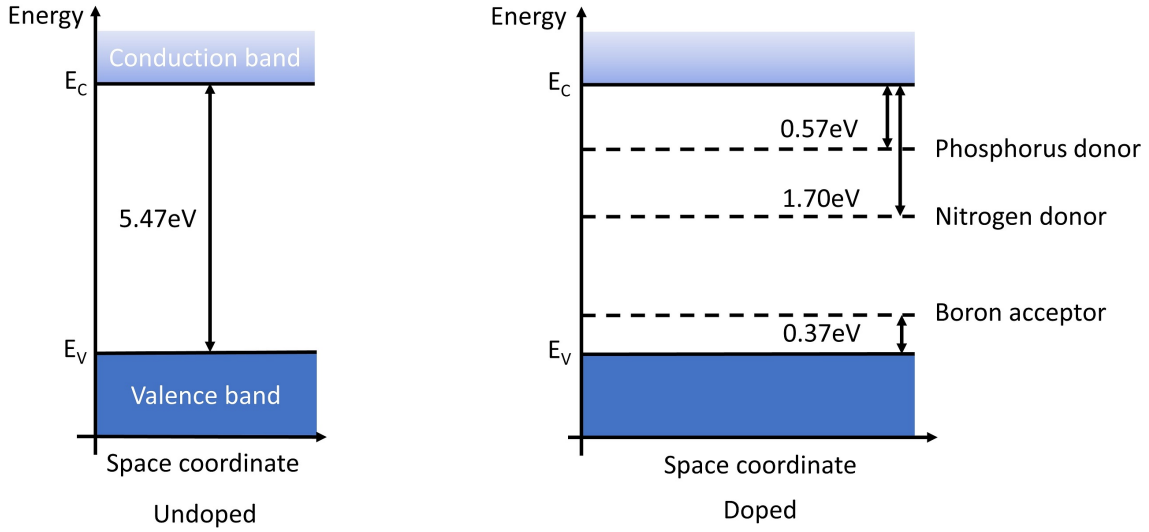

Figure 1.4: Schematic band structure of undoped and doped diamond, to the left and right, respectively. For high doping levels, an impurity band can be formed with a certain bandwidth. Dashed lines represent localized energy levels of donor or acceptor dopants.

Likewise, other elements can be introduced into the diamond lattice to achieve a similiar effect. Nitrogen is the most common donor impurity with an activation energy of around 1.7 eV below the conduction band [8]. Furthermore, it is possible to use phosphorus as a donor, with an activation energy of 0.57 eV below the conduction band [9]. Practically, it has been proven rather hard to incorporate phosphorus because its low solubilty during the chemical vapour deposition (CVD) process. Nitrogen is the most common impurity for single-crystal diamonds and natural diamonds. The Fermi level in doped diamond will be pinned to the impurity dopant level if only one dopant is present in the material. For example, if only boron is present in the film the Fermi level would be positioned roughly 0.37 eV above the valence band. If multiple dopants are present, e.g. boron and nitrogen, then the Fermi level will be pinned at the most abundant impurity level [10]. It is noted, that other forms of deviation from the ideal single crystal lattice structure, such as dislocations,

vacancies, etc., can lead to charge trapping and hence charge transport. Dopants can be introduced into single crystal diamond as well as polycrystalline CVD diamond, which is more easily accessible due to faster growth rates.

1.3 Polycrystalline Diamond and its Mesoscopic Crystal Structures

Polycrystalline diamond consists of single crystal diamond grains, oriented spatially in different directions and interconnected via grain boundaries. At first the grains will be discussed, followed by a short summary of the composition of the grain boundaries.

1.3.1 Morphology of Diamond Grains

Single crystal diamond grains differ in size and morphology. Grain sizes [11, 12, 13] range from ultrananocrystalline (∼3-15 nm), nanocrystalline (∼100-200 nm) to microcrystalline (>1 μm). The morphology can vary from a ball-like structure with a cauliflower texture [14] to polyhedra with atomic flat surfaces. A micrograph of different polyhedra grains is shown in figure 1.5. Many different types of polyhedra with flat surfaces and surfaces with varying step size can be observed. Effects like twinning and creation of stacking faults are of importance in the description polycrystalline diamond films. Such a large variation in grain size and orientation can be attributed to the relative thin film thickness of just 500-600 nm of our diamond films. While it was observed that the {111} and {100} crystallographic faces are grown most commonly in polycrystalline diamond films [15], this is not the case for our samples. The facet with the fastest growth rate should outgrow all

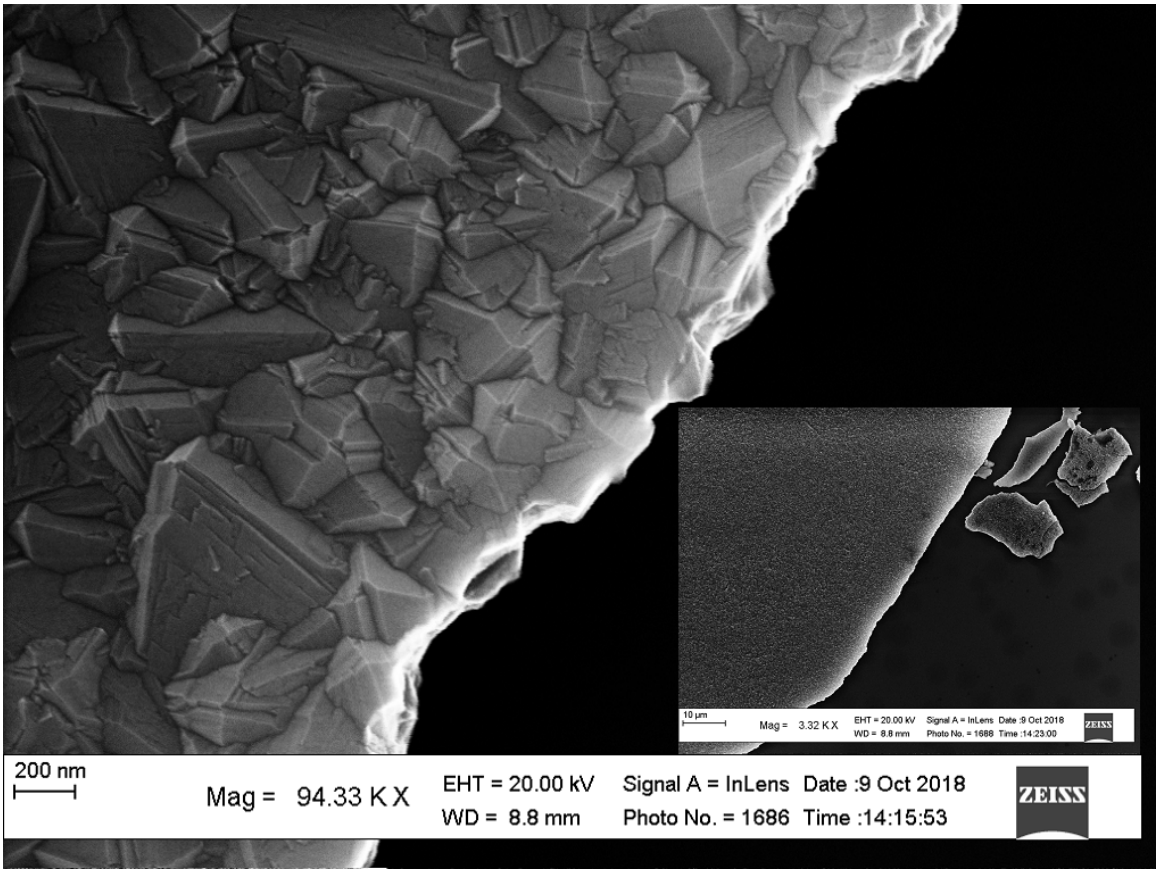

Figure 1.5: In-lens scanning electron micrograph of a top surface of a polycrystalline diamond foil desposited on Si/SiO_2, showing the crystalline composition of the film. Scale bar 200 nm. Inset: Large area scan of the foil showing illuminated edges. Scale bar 10 μm.

other faces, though this is only possible for sufficiently thick films, usually several μm thick, which is not the case for our films. Zhou et al [16] presented that carefully choosing the methane to hydrogen ratio for diamond growth on very densely seeded diamond nanocrystals on single crystal Ni surfaces, results in polycrystalline diamond films with a preferred facet, either the {111} or {100}. Though, results change with different substrates and will depend on specific temperature and pressure in the growth chamber [17]. For the case of crystal growth along different facets, a unitless growth parameter α can be determined from the shape of diamond grains (figure 1.6) that describes the shape of the diamond grain and

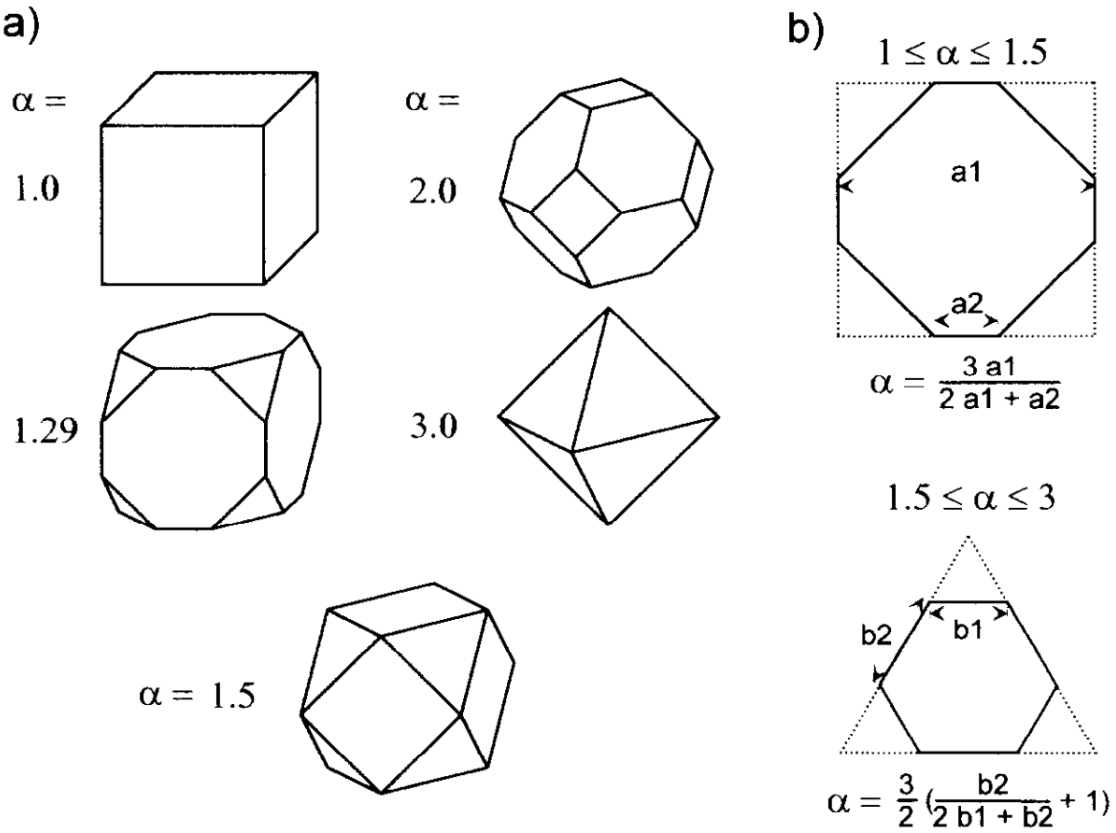

Figure 1.6: Morphology of Diamond Grains. a) Growth parameter α and corresponding polyhedral shapes. b) Diamond {100} ($1 \leq \alpha \leq 1.5$) and {111} ($1.5 \leq \alpha \leq 3$) faces and their relations to α. Reprinted with permission from [17].

relates to the ratio of the growth rates v_{111} and v_{100} as

$$\alpha = \sqrt{3}\,\frac{v_{100}}{v_{111}} \tag{1.4}$$

In figure 1.6a, $\alpha = 1$, $\alpha = 1.5$, and $\alpha = 3$ correspond to a cubic, cubo-octahedral and octahedral grain shape, respectively. Figure 1.6b dotted lines on the top part show the square shape of the {100} crystallographic face and on the bottom part the triangular shape of the {111} crystallographic face with repsective lengths and mathematical relations to α.

1.3.2 Grain Boundaries

In solids, grain boundaries are forming whenever crystals with different lattice parameters or orientations with respect to each other intertwine. In polycrystalline films, grain boundaries seperate two grains of different size or orientation. Scanning electron micrographs (SEM) are commonly used to obtain information about the surface morphology of such films. Figure 1.7 shows a SEM image collected by the in-lens detector of elastically backscattered electrons. In general, a SEM beam of incoming high energy electrons interacts with a solid in various ways. In one of them, electrons scatter elastically with the nuclei of the solid to within a certain depth into the material. Those electrons are referred to as backscattered electrons and are in general sensitive to the atomic number Z of the nucleus. A higher atomic number leads to more backscattered electrons and thus appears brighter in a SEM picture, compared to electrons scattered off atoms with a lower atomic number.

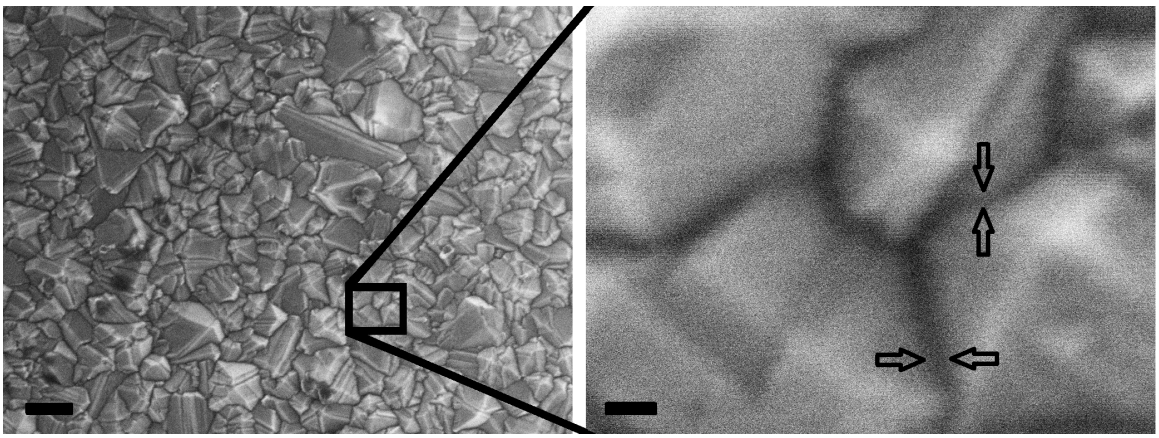

Figure 1.7: Grain boundary dimensions. Left: In-lens scanning electron micrograph of the top side of a diamond film. Scale bar: 220 nm. Right: Enlarged scan showing the dimensions of the grain boundaries. Scale bar: 20 nm. The horizontal and vertical arrows indicate a grain boundary width of 9.1±1 nm and 4.7±1 nm, respectively.

Although, spots appearing brighter in a SEM image can have different origins. For example, a more conductive pathway could capture electrons instead of backscattering

them and thus effectively reducing the number of electrons received by the in-lens detector. The right SEM image in figure 1.7 shows an enlarged scan with arrows indicating grain boundaries and their size. Grain boundaries as wide as 10 nm can be found on the top surface of this specific diamond foil and they appear darker on the SEM image then grains themselves, indicating a change in the mass density. An important question arises now on the specific chemical structure of the grain boundaries and the type of conductivity they exhibit, which is still an open question of study nowadays. During the CVD growth process, ultrananocrystalline grains grow in a columnar structure, intertwine and facets with the fastest growth prevail. In general, diamond films can be composed of a rich variety of chemical structures discussed next.

1.4 Composition of Polycrystalline Diamond Films

Even the most purest CVD polycrystalline diamond films contain slight traces of different amorphous carbons. Ferrari and Robertson [18] presented a ternary phase diagram for amorphous carbon structures in diamond, shown in figure 1.8. In general, pure graphite or pure diamond can be found in the corners of the phase diagram. A mix of sp^2 to sp^3 type of bonds can lead to amourphous carbon (a-C), tetrahedral a-C (ta-C), amorphous hydrogenated carbon (a-C:H) and tetrahedral a-C:h (ta-C:H), referred to as diamond-like carbon (DLC). A sp^3 content of more than 50% is referred to as tetrahedral, either ta-C or ta-C:H. Ferrari and Robertson present additional ternary phase diagrams where hydrogen is replaced with nitrogen, and they note that the phase diagrams should include a fourth dimension that considers clustering of sp^2 sites. Such clusters can form small ring or chain

like structures, while larger structures can form three-dimensional cage-like structures of sp^2 bonds with inclusion of sp^1 chains [18].

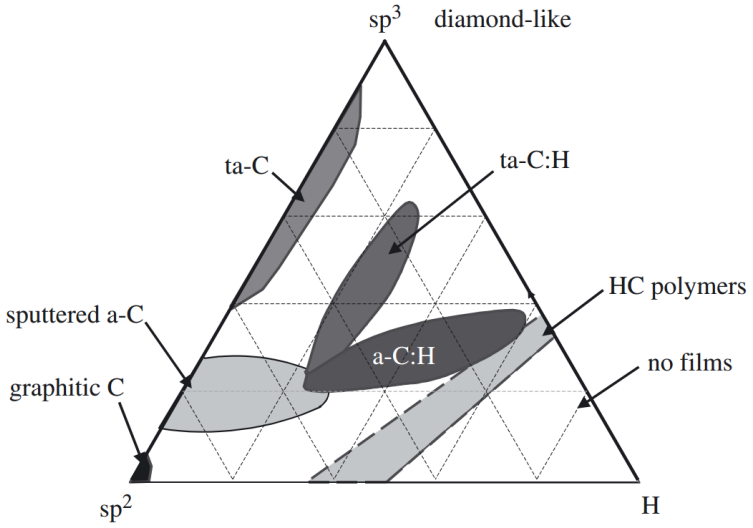

Figure 1.8: Amorphous carbons ternary phase diagram. Any point in the diagram correspond to a ratio of sp^3 : sp^2 : H components in a material. The corners at 1:0:0, 0:1:0 correspond to diamond and graphite, respectively. Pure hydrogenic films (0:0:1) are not possible, instead a band of hydrocarbon polymers can be formed, for example polyacetylene structures. Source [18].

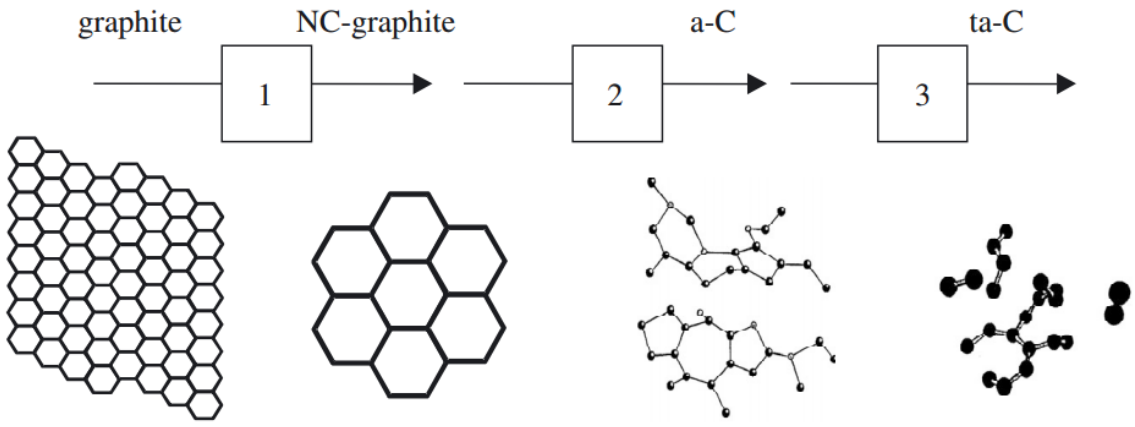

Figure 1.9: Amorphization trajectory showing the three-stage model. Reverse direction along 3→2→ 1 can be understood in terms of an ordering trajectory. Source [18].

In 1999 Ferrari and Robertson published a paper on the interpretation of Raman spectra of disordered and amorphous carbons [19]. They introduced a three-stage model

for introducing defects into a graphite sheet and named it amorphization trajectory. The role of hydrogen is neglected in this model due to the lack of C-H bond signature in the G or D peak. The classification of carbons and its degree of graphitization or amorphization dates back to initial works presented by Lespade et al in 1983 [20].

1.5 Metastability of Diamond

Diamond exhibits metastability with respect to graphite [21]. From diagram 1.10 one can see that graphite is the more stable configuration of carbon bonding and if the barrier is overcome, then a diamond bond transforms into a graphite bond and vice versa.

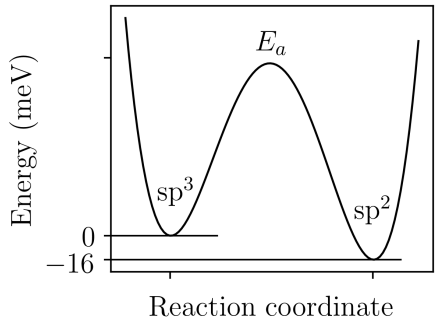

Figure 1.10: Metastability of diamond.

This somewhat contradicts the common experience that diamond is among the most hardest and stable materials, especially since graphite is 'weaker' then diamond in terms of hardness and durability. Very high activation energies for bond transformation of a relatively defect free diamond result in extremely low rates of bond transformation such that within the life time of a human being, transformations from diamond to carbon bonds are extremely rare if not negligible, but certainly possible. Reznik et al [22] studied the kinetics of conversion of broken diamond sp^3 bonds to graphitic sp^2 and extracted

an activation energy of 0.7 eV for this transformation. Diamond bonds were broken by bombaring the diamond lattice with high energy Xe ions (320 keV) with a total dosage $D = 5 \cdot 10^{14}$ cm^{-2}, hereby introducing a considerable density of defects (vacancies) N. Earlier studies by Uzan-Saguy [23] found a critical density of defects $N_C(N_0, D_C) = 10^{22}$ vacancies/cm^3, such that if

$$N > N_C \overset{\text{Annealing}}{\Longrightarrow} \text{Graphitization of broken bonds}$$

$$N < N_C \overset{\text{Annealing}}{\Longrightarrow} \text{Recovery of broken diamond bonds.}$$

If the density of defects is above N_C, graphitization occurs upon annealing, while broken diamond bonds recover if $N < N_C$. This approach has been used to create ohmic graphitic contacts to diamond. An activation energy of (0.7±0.1) eV for graphitization was measured upon annealing between 300-600°C [22].

While it is possible to create graphite from diamond, diamond can also be created from graphite.

For this, Palnichenko [24] demonstrated, that by applying and intense voltage pulse (1000 A) in vacuum between two graphitic contacts seperated by 5-10 mm and of 0.5 mm diameter, diamond microcrystals can be found on a subtrate beneath the contacts with sizes ranging from 10 μm to 100 μm. All in all, switching between diamond and graphitic bonds is possible, but it requires extreme conditions in the laboratory.

Chapter 2

Material Growth and Device Fabrication

2.1 Overview

This chapter describes the growth of graphene and polycrystalline diamond as well as sample fabrication procedures for a diamond-on-graphene heterostructure with comments and observations on common problems. During the initial stages of this project chemical vapor deposited (CVD) graphene was grown in a furnace (section 2.2.1). Later on, CVD graphene was commercially purchased [from Graphenea]. Thin polycrystalline diamond foils were grown by our collaborateurs in a plasma enhanced chemical vapour deposition (PECVD) process with the option of incorporating boron as a dopant into the diamond lattice (section 2.2.2). Device fabrication can be split into following steps. Firstly, transfer (section 2.3.4) of graphene onto a preferred substrate (section 2.3.1). Secondly, patterning

of graphene into a desired shape in an oxygen environment in an inductive coupled plasma (ICP) (section 2.3.9) or reactive ion etching (RIE) chamber. Thirdly, successive transfer of a diamond flake onto a patterned graphene sample (section 2.3.7). Fourthly, evaporation of metallic leads onto the diamond-on-graphene device through an electron-beam lithography (EBL) (section 2.3.8) shaped polymer mask in an electron beam evaporator (section 2.3.10). Lastly, after a successful lift-off process of the shaped polymer mask, the device is capped off with a few layers off a protective polymer material (section 2.3.3). Additional EBL is required to open up windows to the bonding pads on the device substrate for wire bonding of macroscopic wires which finalizes the device fabrication.

2.2 Material Growth

2.2.1 Chemical Vapor Deposition of Graphene

Chemical vapor deposition of graphene on commercially available 25 µm thick copper foils (10950 Alfa Aesar) was performed in a Lindberg/BlueM TF55035A quartz tube furnace. A one-inch quartz tube was connected on one end to a vacuum pump to achieve a low pressure growth. On the other end, a pressure-based mass MKS Flow Controller was connected, which regulates the low pressure gas flow. The outcoming gas from the vacuum pump exhaust was redirected to a fume hood for proper disposal of flammable gases.

Our copper foils were electropolished before graphene growth. Electropolished copper exhibits higher individual single crystal graphene grains compared to unpolished samples with intrinsic properties similar to exfoliated graphene [25], which is attributed to a reduced surface roughness. Electropolishing is performed in an electrochemical cell, which

consists of two copper foils (the anode and the cathode), suspended in a phosphoric acid based electrolyte. Details of the electropolishing process can be found in [26].

The electropolished copper was rolled-up into a tubular structure and placed in the middle of the furnace. Our growth process consists of a ramp stage, an anneal stage, a growth stage, and a cool down stage. Before the ramp stage was started, the hydrogen flow rate was set to 50 sccm and the vacuum pump was turned on reaching a pressure of 0.65 Torr. Next, the temperature was ramped up to 1030°C within 30 minutes where it stayed constant at 1030°C for 60 minutes. The growth stage starts by turning on the methane flow and lasts for 30 mintues with a 0.1 sccm flow rate. During this period the CVD graphene grows on the copper surface. After 30 minutes the methane flow rate and the furnace heater were turned off. The furnace was allowed to cool down to around 600°C before it is opened to accelerate the cool down time. It is important to keep the heated CVD graphene on copper within the hydrogen flow since at these elevated temperatures the graphene would easily oxidize when exposed to atmospheric gases. Once room temperature is reached, the vacuum pump is turned off.

2.2.2 Microwave Plasma Assisted Chemical Vapor Deposition of Polycrystalline Diamond

Growth recipe and parameters

Polycrystalline diamond can be grown at reduced temperature in a microwave plasma chemical vapor deposition (MPCVD) process. Diamond foils used in this work were synthesized in a MPCVD system (SEKI Technotron AX5400S) on mirror-polished

tantalum foils (Sigma-Aldrich Chemie, 0.025 mm thick, 99.9+ % metal basis) by Robert Bogdanowicz's group at the Gdansk University of Technology in Poland. Prior to growth, a diamond slurry was spin-coated (section 2.3.2) on the mirror-polished tantalum foils with nanodiamond particles of 4-7 nm size.

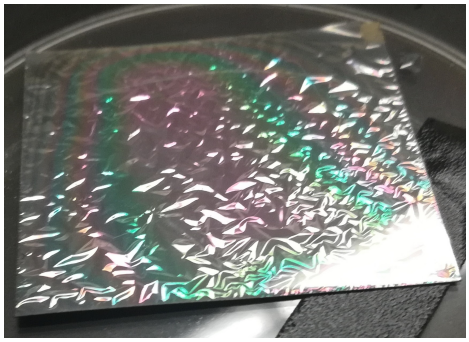

Figure 2.1: Diamond film on a tantalum substrate.

Nanodiamonds were suspended in a dimethyl sulfoxide (DMSO) with 1 % of polyvinylalcohol (PVA) solution. During the growth process the temperature of the graphite stage is kept at 500°C, the microwave power is set at 1000 W and diborane, B_2H_6, is used as the dopant precurser. The total gas flow rate is held at 300 sccm with a 1:99 gas ratio of CH_4:H_2. A growth time of 120 minutes results in diamond foil film thickness of 600 nm. Figure 2.1 shows a 600 nm thin diamond film on a 2.5 cm x 2.5 cm tantalum substrate. In this case, the boron level in the gas phase was 10k ppm of boron to carbon atoms.

The growth mechanics

CVD diamond can be grown by three main growth processes. High pressure high temperature growth, hot filament activated CVD growth or plasma activated CVD growth. In this work the plasma activated method is utilized. In general, a diamond or a non-diamond substrate can be used for CVD diamond growth. If a non-diamond substrate is

chosen, then nucleation phenomena and seeding need to be taken into consideration. Growing CVD diamond can be performed with as little as two gases, hydrogen (H_2) and methane (CH_4), though other gases can be included to either dope diamond or suppress growth of sp^2 bonded carbons. Matsumoto et al. were the first to present a diamond growth on different substrates in a hydrogen-methane gas environment in a hot filament activated CVD [27]. A year later Muto et al. [28], as well as Saito et al. [29], independently showed that plasma activated CVD of a hydrogen-methane gas mixture works for growing diamond. In a plasma environment, hydrogen gas molecules dissociate into hydrogen atoms fulfilling two main functions. Once, hydrogen atoms terminate diamonds surface by forming a CH group to stabilize diamond against growth of graphitic carbon at elevated temperatures. Secondly, they react with the hydrocarbon source gas (methane) to produce additional hydrogen atoms and hydrocarbon species, some of which act as highly reactive radicals. Both, hydrogen atoms and radical hydrocarbon species will interact with the hydrogen terminated diamond species, sometimes 'knocking out' a H atom from the surface. Most frequently, another hydrogen atom adsorbs to maintain the hydrogen termination. Occasionally, a hydrocarbon radical attaches to the dangling C bond to progress the diamond growth. This is the atomistic standard model for diamond CVD growth.

Although, somewhat of a controversy remains around this growth model. Jeon et al. [14] showed that larger clusters of hundreds to thousands of atoms can exist in a CVD diamond growth process, growing in traditional form with flat surfaces and edges or in a spherical shape with a cauliflower like texture [14]. Hwang et al. [30] proposed the possibility that diamond growth can also occur through charged clusters that form in the gas

environment, instead of an atom by atom approach. The necessity for such an alternative growth process originated from inconsistencies in the standard model for diamond CVD growth. The latter process includes irreversible simultanous etching of the more stable carbon phase and deposition of the less stable diamond phase. Hwang argued that such a process violates the second law of thermodynamics [31, 32]. Such an inconsistency is avoided, if diamond nucleates in the gas phase and attaches to the substrate in larger clusters. Similar observations of particles forming clusters have been observed in previous works by Glasner [33] on the precipitation of molecules in aqueous solutions and by Sunagawa's work [34]. Sunagawa pointed out that low pressure grown diamond shows step heights of up to 100 nm and that the {100} face can grow larger than the {111} face, which led him to the conclusion that the growth units could not only be atomic or molecular but must include larger building blocks, like clusters of atoms grown in the vapor phase. Furthermore, succesful synthesis of diamond in vacuum through an intense heat pulse [24] has been demonstrated, which further supports formation of clustered unit growth. A more in depth review of this alternative growth process can be found in [32, 35].

2.3 Methods of Heterostructure Fabrication

2.3.1 Substrates

Our experiments, unless otherwise stated, focused mainly on two substrate materials, silicon with a 300 nm thick insulating silicon dioxide layer, denoted as Si/SiO_2 from hereon, and ST-cut quartz. The 300 nm thick insulating layer has two functions. It acts as a insulating dielectric for applying a gate voltage to a heterostructure and it provides a

contrast between the substrate and graphene for enhanced visibility, see figure 2.2. Blake [36] analyzed the visibility of graphene on a substrate based on Fresnel theory to show that graphene on Si/SiO_2 is particularly visible within specific bands of wavelengths and thickness of the insulating dielectric. For example, white light illumination of a 200 nm thick SiO_2 does not provide good visibility of graphene, while 300 nm thick SiO_2 shows a good contrast for graphene and multilayers of graphene. In such a way graphene can be identified and distinguished from the substrate and multilayer graphene flakes through a simple optical microscope.

The second material is insulating ST-cut quartz. ST specifies the crystallographic orientation along which the quartz substrate is cut and polished. For this substrate, if desired, a top gate needs to be fabricated for applying a gate voltage to a heterostructure. It is possible to identify graphene on quartz through an optical microscope under high illumination and a black background below the quartz substrate, see right plot of figure 2.2.

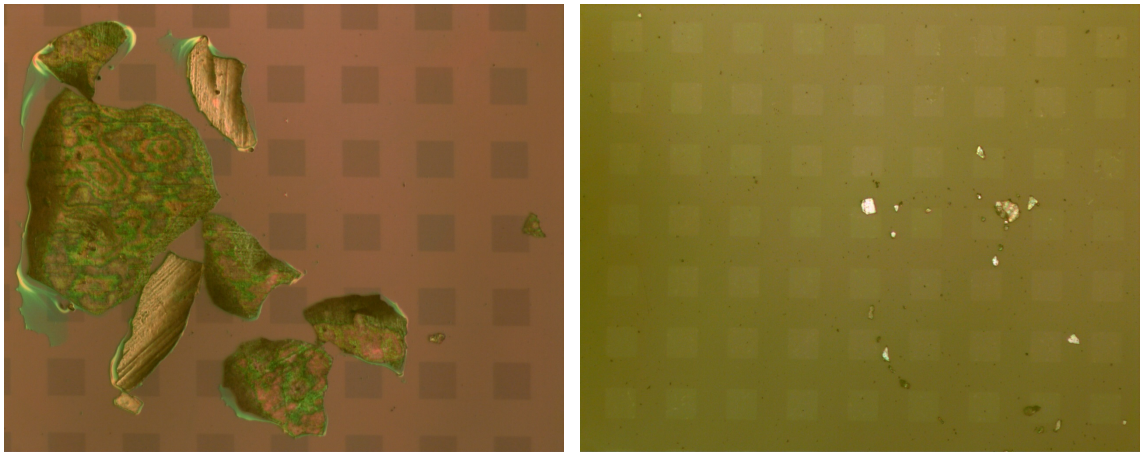

Figure 2.2: Graphene etched into squares on top of which one can find diamond flakes on a Si/SiO_2 (left) or ST-cut quartz (right) substrate.

Furthermore, it was observed that if the background below the quartz substrate was reflecting light well, it was not very easily possible to distinguish graphene from the

quartz substrate. Hence, we conclude that graphene's intrinsic reflectance is enough to provide visibility, albeit it is more pronounced when a thin layer with well chosen thickness is used for constructive interference between incoming and reflected light, like for Si/SiO_2. Quartz was the preferred substrate for memristor studies in this work, since it allowed to apply high voltages without worrying about leakage currents towards the backgate.

2.3.2 Spin-Coating

Spin-coating is the process of depositing a thin layer of a viscous solution on top of a substrate by spinning. The substrate is positioned on the spinner, a droplet of the viscous solution is drop-casted on top of the substrate. The spin-coating starts by steadily ramping up to a constant spin-velocity. The ramping stage ensures that the viscous solution uniformly spreads over the substrate and the constant spin-velocity stage is maintained long enough for the viscous film to reach its final thickness.

For the case of spin coating Poly(methyl methacrylate) (PMMA) onto a substrate, we ramped up for 3 seconds with 1000 rpms (rounds per minute per second). A constant spin velocity of 4000 rpm leads to a thickness of roughly 250 nm. Consecutively, the film is baked for 2 minuntes at 180°C in ambient environment on a hot plate. For thicker films the process of spinning and baking is repeated and it is important to not skip the baking process, since additional PMMA after the second layer will spin-off completely, not adding to the total thickness. Lift-off process of 400 nm thick metallic contacts onto 600 nm thick diamond samples required a PMMA lift-off mask thickness of around 2 μm. PMMA can be removed in an acetone bath within a few minutes but usually it remained in the acetone bath overnight to ensure proper removal of the polymer mask on the mesoscopic scale.

Writing of metallic contact leads onto quartz requires an additional layer on top of the finished PMMA because of charge accumulation during electron beam lithography. AR-PC 5090 (Electra 92) is used as such an additional conducing layer with the purpose of removing accumulated charges at the surface. AR-PC 5090 is spin coated with a final spin-velocity of 6000 rpm resulting in a thin 40 nm thick conductive top layer which can easily be washed off with distilled water for 40 seconds after electron beam lithography.

2.3.3 Versatility of PMMA

Through most of this work, unless otherwise stated, Poly(methyl methacrylate) (short PMMA, Microchem 950 A4) is spinned (section 2.3.2) onto any of the above mentioned substrates, where it can fulfill different functions.

Figure 2.3: Left: Finished diamond flake without a PMMA capping layer. Right: Diamond flake delaminated during electronic measurement.

It can be used as a protective mask during the patterning of graphene, as a lift-off mask for patterning of macroscopic leads and contacting pads to a heterostructure or as a capping layer, which protects the final diamond-on-graphene heterostructure. It was found during the course of this study that a final capping layer of PMMA on the heterostructure

helps to overcome 3 different issues. First, it enhances the contact between diamond and graphene, due to its adhesion and surface tension exhibited on diamond. Second, measurements were preformed where diamond happened to deattach from the substrate during the measurement and was completely removed, see figure 2.3. Third, during high temperature measurements a capping layer of PMMA serves as an encapsulating layer for the diamond top surface and graphene, protecting it from oxidization and degradation of graphene at higher temperatures.

2.3.4 Polymer Assisted Transfer of CVD Graphene

Device fabrication requires the transfer of CVD graphene onto any desired substrate. This is accomplished in the following way. A thin layer of Poly(methyl methacrylate) (PMMA) resin is either spin-coated, see section 2.3.2, with a thickness of 250 nm or drop-casted onto one side of the graphene-on-copper foil. Then, an inductive coupled plasma (ICP) etch or reactive ion etch (RIE) in oxygen followed, to remove graphene on the PMMA-free side. It is not hard to remove a single atomic layer of carbon and hence a weak etch is sufficient, e.g. in an ICP for a duration of 5 s at a "ICP power" of 50 W, a "forward power" of 50 W and an O_2 gas flow of 50 sccm. It is recommended to optically check that the plasma is turned on during the etch process. After the bottom graphene (PMMA free) is removed, the copper/graphene/PMMA foil is placed into a copper etchant solution (Transene APS copper etchant 100) with the copper side facing the copper etchant. Depending on the strength of the copper etchant, the etching time may vary and it is recommended to observe the copper dissolve. Usually, two hours was enough to dissolve the copper and find a floating graphene/PMMA layer on top of the solution.

The PMMA serves with two important functions. Firstly, its hydrophobic properties ensure that the stack (graphene/PMMA) remains floating on top of the solution. Secondly, it prevents graphene from scrumbling and enables the stack to be scooped up with a freshly cleaned bare silicon wafer and transferred in a beaker filled with deionized water. The bare silicon wafer is rinsed with acetone, isopropanol and deionized water before scooping up the stack. Once the stack is transferred, the deionized water removes the copper etchant from the graphene surface. The transfer process of the stack from one beaker to another beaker can be carried out successfully as long as a thin aqueaous layer remains between the stack and the bare silicon wafer. The thin aqueous layer prevents the stack to stick to the silicon wafer. The stack is transferred to two additonal beakers with deionized water to remove any etchant residues. Finally, the stack can be scooped up with a desired substrate, in this study either Si/SiO_2 or ST-cut quartz. The substrate/graphene/PMMA structure is deposited onto a hot plate at 60°C for 30 minutes in air to remove the aqueous layer between the substrate and the stack. Consequently, the temperature is raised to 120°C to improve adhesion of graphene and the substrate and to relax existing stress in the PMMA layer. The PMMA layer is washed off in an acetone bath overnight and rinsed off with IPA. Before transfer of an additional material for heterostructure fabrication, the graphene on the substrate will be cleaned in a furnace for 4-6 hours in and 2 sccm Argon flow at 300°C.

Unless otherwise stated, graphene will be patterned into a desired shape before diamond can be transferred onto graphene. This process consists of spin-coating PMMA on top of graphene, followed by a hot bake. Electron-beam lithography, see section 2.3.8, is utilized to shape the mask into the desired pattern. ICP etching with the above recipe

removes exposed graphene. The PMMA layer is washed off in an acetone bath overnight and rinsed off with IPA. Now diamond sheets can be transferred onto graphene either through a polymer assisted or a polymer-free process.

2.3.5 Polymer Assisted Transfer of Diamond

Elvacite acrylic resin is spin coated onto a scotch tape on a glass slide stack at 4000 rpm for 1 minute at 1000 rpm/s acceleration.The stack is baked at 110°C for 10 minutes on a hot plate in air. The diamond sheets are mechanically downsized with tweezers, picked up with a pipette tip and positioned onto Elvacite acrylic resin/scotch tape/glass slide stack. The stack and the desired substrate are placed in a transfer microscope with x, y and z stage movement and two-axis tilt setup for slope compensation, see figure 2.5. Relative positioning is monitored through an optical setup, while the substrate and the diamond are brought into contact. The stage is heated up above the glass transition of the Elvacite acrylic resin to 65°C. The resin sticks to the substrate and the diamond is transferred. The resin is removed in a water/acetone bath.

2.3.6 Polymer-Free Assisted Transfer of Diamond - Water Droplet Method

Polymer assisted transfer processes reduce the samples quality and its electronic characteristics due to leftover residue. Thus, it is desirable to have a polymer-free transfer process. We utilize deionized water as the transfer medium in our polymer-free transfer process, which is pictured in figure 2.4. A droplet of deionized water (DI H_2O) is deposited on top of CVD graphene on a Si/SiO_2 substrate. Then, diamond flakes are mechanically downsized, picked up with a pipette tip and deposited into the water droplet.

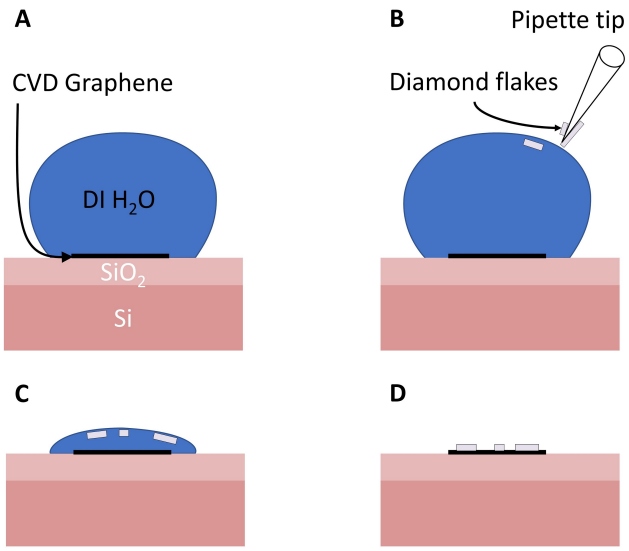

Figure 2.4: Polymer-free assisted transfer method, exemplified for the case of a diamond-on-graphene junction. A) Droplet of deionized water on top of the substrate. B) Mechanically downsized diamond flakes (shown in grey) deposited into the water droplet with a pipette tip. C) and D) The deionized water evaporates and a heterostructure is formed.

As the water evaporates, the diamond flakes are pushed onto the graphene due to the polar forces of the water and a diamond-on-graphene heterostructure is formed. The drawback of this method is the random nature of deposition of diamond flakes. Only by chance will a diamond flake end up on the CVD graphene. Another drawback could be residue present in the water, which can contaminate our materials.

2.3.7 Pick-up and Transfer: The Mechanics of Fabricating a Diamond-on-Graphene Heterostructure

Instead of using the water droplet method with its randomly distributed diamond deposition on graphene it is more desirable to perform transfer of diamond flakes deterministically. Therefore a transfer procedure similiar to the one presented by Pizzocchero et al. [37] was adapted. Pizzocchero et al. introduced a technique to pick up two-dimensional

materials from a substrate and deposit it on another position or another substrate. The pick up and drop down of materials can be executed consecutively to built stacks of hetero- or homostructures of materials. This opened up the possibility for a wide range of potential new material classes by stacking different two-dimensional materials. An adjusted pick-up and transfer approach is used in this study. The main differences lie in the way the pick-up and transfer is performed and their respective temperatures. The following segment describes the specifics of fabricating a diamond-on-graphene heterostructure.

The main components for the pick-up and transfer process are an optical microscope, a sample stage, a heater and a glass slide holder, shown in figure 2.5. The optical microscope is equipped with a 10x objective for monitoring the pick-up and transfer process. The sample stage can be moved in x and y direction, tilted around the x and y direction and rotated in the sample plane. The substrate with the material to be picked up is positioned on the sample stage. A current dissipates through a resistive element which is placed right below the sample stage. There can also be found a hollow cavity where a temperature probe is positioned. The voltage drop at the temperature probe is monitered with a multimeter and converted into a temperature reading. A glass slide with polymers is placed in the glass slide holder and can be moved in x, y and z direction. Such a glass slide with polymers will be used to pick-up flakes from their substrates. A 0.7 x 0.7 cm^2 piece of polydimethylsiloxane (PDMS) is deposited on the glass slide which is followed by spin-coating a thin layer of 20% polypropylene carbonate (PPC) in anisole solution, prepared by weight. Spin-coating, see section 2.3.2, is performed at 4000rpm for 45seconds which results in a film thickness of a few μm. Subsequent baking of the glass slide/PDMS/PPC stamp is crucial for whether

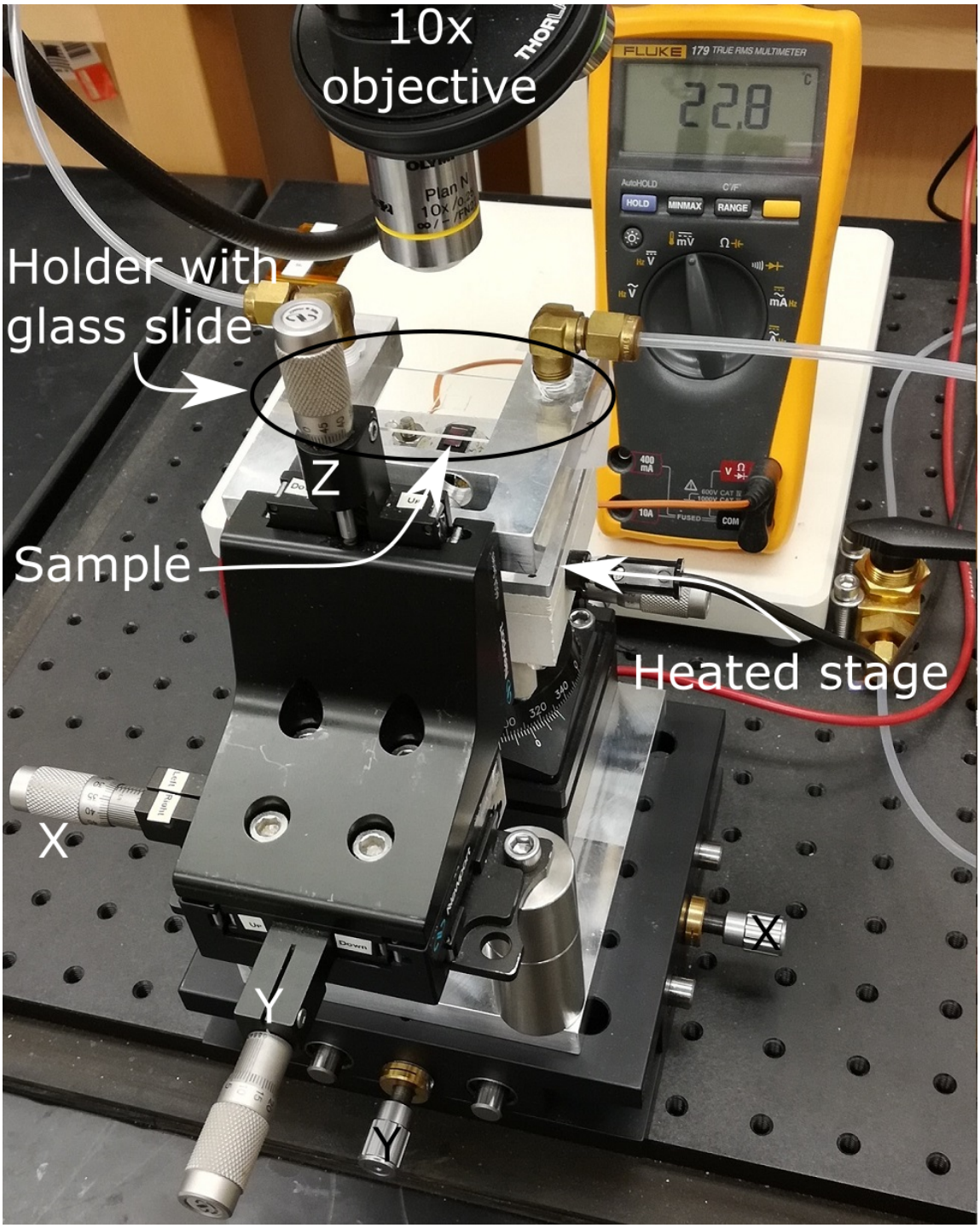

Figure 2.5: Transfer stage for heterostructure assembly. Optical microscope with 10x objective, heated stage and glass slide holder for pick up and transfer process. A temperature probe is connected to a multimeter displaying the temperature of the stage. Micrometer positioners for the X, Y and Z axes of the glass slide holder are labelled in white. The X and Y axes of the heated stage are labelled in black.

the PPC will be able to pick up hBN or not. It was found that prolonged baking time of 2-5 minutes at 180°C on a hot plate in ambient environment results in the PPC not being able to pick up a hBN flake. A backing time of 30-40 seconds was found to provide a good adhesion of the PPC for pick-up. Though, this only worked for roughly every second stamp. If the PPC was unable to pick-up a flake, then another glass slide/PDMS/PPC stamp was prepared.

During the course of this work a problem occurred with the diamond-on-graphene heterostructure fabrication. Quite frequently, in around 50-70 % of samples the diamond flake tended to deattach from the graphene during the lift-off procedure of metallic contact deposition. Therefore, it turned out to be helpful to pin down the diamond flake on the substrate with a hBN flake. Hence, the schematic representation of the pick-up and transfer procedure starts with a hBN flake deposited on a Si/SiO_2 substrate in figure 2.6A. hBN was obtained by exfoliation and annealed in a furnace under oxygen flow for 2 hours at 300°C to remove leftover residue from the surface from the exfoliation process. Prior to exfoliation, the Si/SiO_2 substrate was high-pressure spray-cleaned with acetone, ultrasonicated in an acetone bath, rinsed of with IPA and placed in a plasma asher for 1 minute at 100 W power in oxygen flow to remove organic components from its surface.

Next, figure 2.6 is explained in closer detail. At first, the PDMS/PPC stack is brought into contact with the hBN at room temperature, shown in schematics A. The screw that levels the z-position of the glass slide holder is fully unscrewed. It was found, that the full weight of the glass slide holder enhances the pick-up procedure. In schematics B, the interface is heated up to 50°C and cooled down to 24°C again. The observer will

notice that the hBN/PPC interface changes its color to a more uniform structure as the temperature passes PPC's glass transition temperature between 30-40°C. Passing PPCs glass transition temperature changes PPCs material properties from solid to a viscous like fluid structure, which allows the PPCs to improve the contact to the substrate and the hBN. Upon cooling below its glass transition temperature, PPC becomes solid again and sticks to hBN, due to the enhanced contact from the viscous phase. Now the glass slide holder is retracted and hBN is picked up by the PPC, shown in schematics C. It is noted, that the heating and cooling cycle is not always necessary to pick up a hBN flake.

Next, diamond flakes are deposited on a Si/SiO2 substrate by the water droplet method, see section 2.3.6. A suitable sized diamond flake is chosen with no cracks and little to no graphitic contaminations on its surface. The procedure for pick-up of the diamond flake is repeated analogously as described previously in schematics A-C. Nonetheless, this procedure is shown again in schematics D-F to display two important insights about the mechanics of hBN and the adhesion of the diamond/hBN interface. First, in schematic E one can see that the diamond flake is not completely covered by hBN during the pick-up. It turns out, even though the flat side of the diamond flake with a surface roughness of 2-4 nm (compared to 60 nm on the top side) was facing the hBN, it was not possible to pick up the diamond flake. This can be pinpointed to a low adhesion of the diamond/hBN interface, as well as the requirement of atomically flat surfaces for a successful pick-up. Exposing part of the diamond flake to PPC made it possible to pick-up the diamond flake, see middle image figure 2.7. The diamond flake in the right image of figure 2.7 was around 600 nm and the hBN only 200 nm thick.

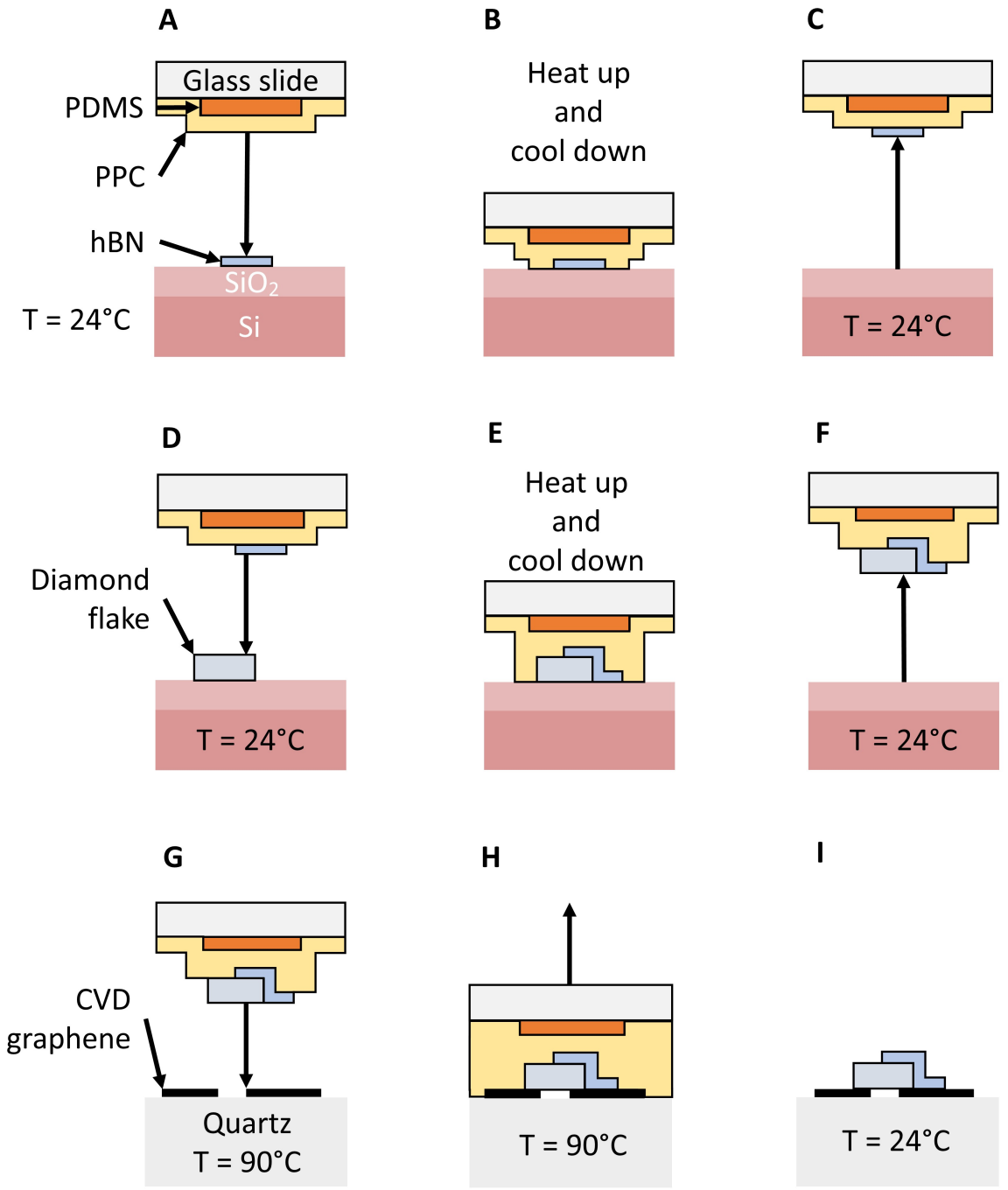

Figure 2.6: Schematic representation of the pick up and transfer process, in greater detail described in the main text body.

One can see, that hBN was stretched over the edges of the diamond flake, since interference patterns due to elastic stretching of the hBN flake are only visible at the edges

of the diamond flake. Next, the diamond/hBN stack was deposited onto a quartz/graphene substrate. This procedure is illustrated in schematics G-I in figure 2.6. Quartz/graphene is heated up to 90°C under ambient environment. The glass slide/PDMS/PPC/hBN/diamond stack is lowered onto the graphene substrate such that a bridge is formed between two graphene sheets, see schematics H. As the glass slide/PDMS is retracted the PPC/hBN/ diamond sticks to the substrate at 90°C. The newly formed diamond-on-graphene heterostructure is left on a hot plate at 110°C for 30 minutes under ambient environment to enhance the contact between the graphene-diamond, graphene-hBN and quartz-hBN interface. Once the sample is removed from the hot plate it is allowed to cool down to room temperature before the PPC is washed off in an acetone bath for a few minutes. Placing the hot substrate in the acetone bath can result in removal of the diamond and/or hBN.

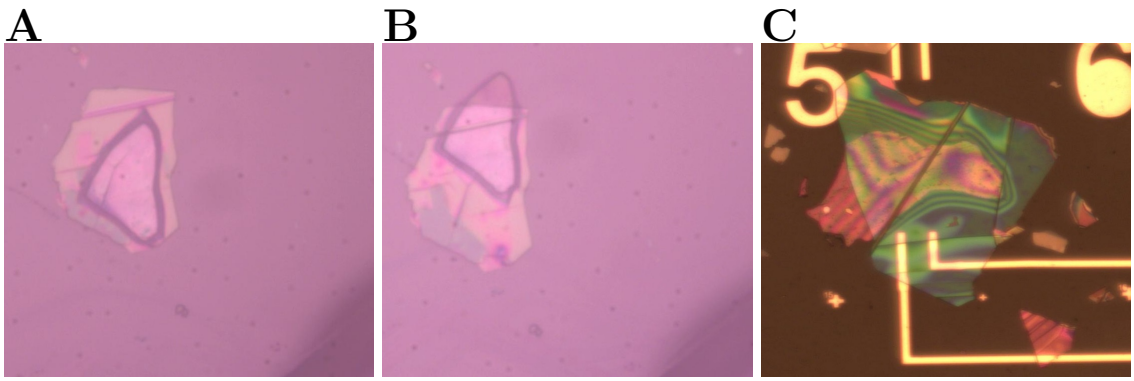

Figure 2.7: Pick-up and transfer of diamond with hBN. A and B: Si/SiO_2/Diamond/hBN/PPC stack. A: hBN completely covers a diamond flake and the pick-up fails. B: hBN partially covers a diamond flake and the pick-up succeeds. C: Si/SiO_2/Graphene/Diamond/hBN stack with Ti/Au contacts. 200 nm thick hBN lays on top of 50 nm thick Ti/Au contacts and 600 nm thick diamond flake. Interference patterns of the hBN flake are only visible at the edges of the diamond flake.

2.3.8 Electron-Beam Lithography

Electron-beam lithography is used to define patterns on a PMMA resist, which can be either used as an etching mask or a lift-off layer for contact deposition. The electron-beam system was either a Leo SUPRA 55 or a Leo XB1540, both with capabilities for microscopic pattern generation through the nano pattern generation system (NPGS) software [38] version 9. Desired microscopic patterns were designed with DesignCAD2000. Proper preparation of the electron-beam distance, dosage testing, and beam adjustment were important for a successful pattern generation. After electron-beam exposure of the PMMA film the desired patterns were developed in MIBK:IPA 1:4 solution for 65 seconds at room temperature and rinsed off with IPA. The sample is ready for further processing, either etching or contact deposition.

2.3.9 Dry Etching

Inductive coupled plasma (ICP) etching or reactive ion etching (RIE) can be used to etch graphene into desired shapes, with oxygen as the etching agent and 500 nm thick PMMA as the etching mask. The PMMA mask can be prepared through electron-beam lithography as described in the section 2.3.8. For the ICP etching an Oxford Plasmalab 100/180 model was used, with a base pressure of 20 mTorr, 30 W forward power, 300 W ICP power and 50 sccm oxygen flow for 10 seconds. For the RIE process an STS Multiplex RIE system was used, with a base pressure of 20 mTorr, 50 W etching power in 50 sccm oxygen flow for 10 seconds. The general procedure for either machine consists of loading the sample into a primary loadlock-chamber, consecutive pumping of the loadlock and flushing

of the main chamber with nitrogen. After the flushing procedure, the sample is moved into the main chamber for the etching process. The main chamber gets filled with the desired gas (here oxygen) and the etching recipe is run.

2.3.10 Electron-Beam Evaporation

Metallic contacts are evaporated through electron-beam evaporation in a Temescal BJD 1800 system. The sample with a pre-patterned PMMA mask is loaded into the evaporator and pumped down to a pressure below 10^{-6} Torr. An high energy electron beam sweeps over a pocket filled with a desired metal and heats it up evenly. Increasing the power of the electron beam over a certain threshold value, leads to emission of atoms from the metal. The metal deposits on our sample at a controlled rate, reaching averaged values as low as 0.1 nm/s. As a general rule of thumb, the deposited metal should not be larger than 1/3 of the pre-patterned PMMA mask thickness.

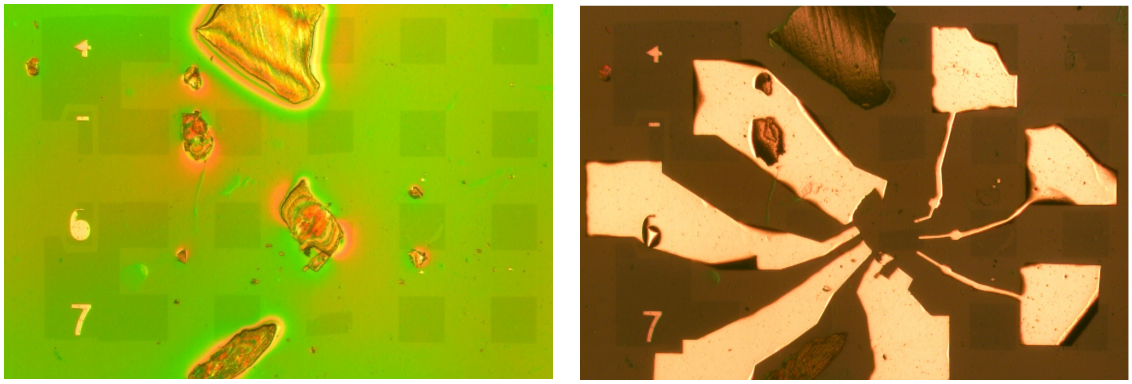

Figure 2.8: Risk of removing diamond flake. Left: Diamond flake before electron beam lithography, electron beam evaporation, and lift-off. Right: After prolonged lift-off time the possibility of the flake to deliminate increases.

After metal deposition, a lift-off procedure is performed by depositing the sample in acetone overnight. Prolonged lift-off procedures carry the risk of removing the diamond

flake, see figure 2.8. Therefore, a top hBN flake was used to pinpoint the diamond flake for long lift off times, in order to enhance the contact of the diamond-on-graphene interface.

2.3.11 Device Geometries

This dissertation showed that diamond films can be used for device application as a barristor or memristor. The structure of the devices are described shortly. The left plot of figure 2.9 shows an optical image of a diamond-on-graphene heterojunction, which was used to show that a barristor behavior is possible. The diamond nanosheet is marked by a white line, the CVD graphene islands by a black line, and evaporated Ti/Au contacts are shown in a goldish tone. Blue lines also indicate the region where graphene islands have been cut by etching away a narrow area to avoid crosscurrents. On the right side, one can see a schematic side-view of the device structure and setup for electronic measurement setup. A silicon backgate is used to tune the Fermi level of graphene, which allows usage as a barristor device structure.

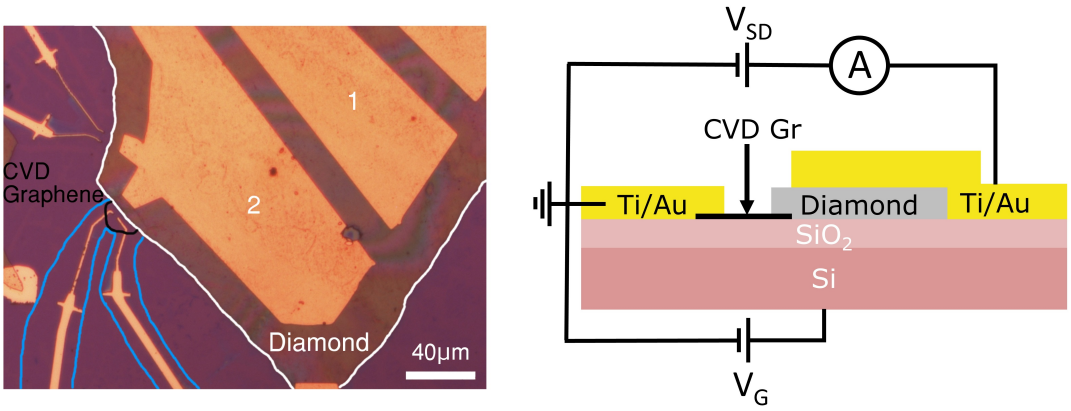

Figure 2.9: Left: Optical image of a diamond-on-graphene heterojunction on Si/SiO_2. Taken from [39]. Right: Schematic diagram of a side-view of the device structure.

Figure 2.10 shows an optical image of a hBN/diamond/graphene heterostructure. Hexgonal boron-nitride is used to prevent the diamond flake from deliminating during lift-off or measurement procedures. During experiments, a high voltage is applied on undoped diamond films and hence the Si/SiO_2 substrate is replaced by quartz, in order to avoid leakage currents to the backgate. Such a setup is used for memristor studies of our undoped diamond films.

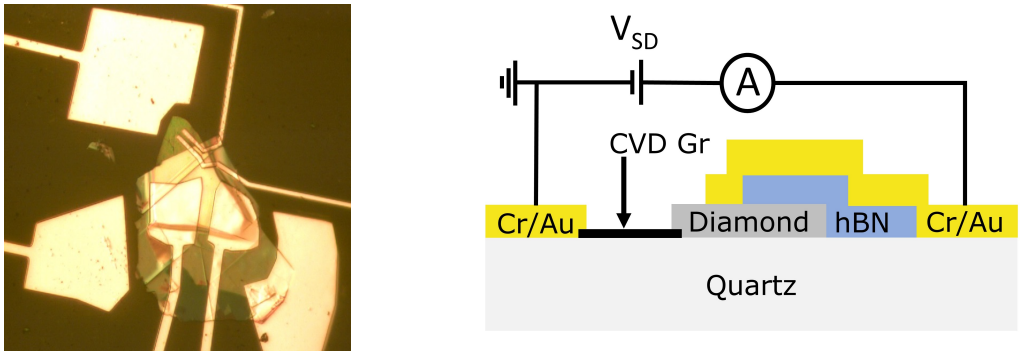

Figure 2.10: Memristor device. Left: Optical image of a hBN/diamond/graphene heterostructure. Right: Schematic diagram of a side-view.

Chapter 3

Material Characterization and Measurement Techniques

3.1 Raman Spectroscopy

Light incident upon a medium (solid, liquid, gas) can be scattered elastically or inelastically. Elastic scattering of light or electromagnetic waves is referred to as Rayleigh scattering, which has the same incoming and outgoing wavelength. In contrast, inelastic scattering results in energy exchange of the incoming light with a medium and thus the outgoing energy and wavelength differs from the incoming one. This effect was first observed by Chandrasekhara Venkata Raman in 1928 [40], who was shortly after awarded with the Nobel prize in 1930 [41]. Successively, inelastic scattering of light was termed Raman scattering.

In general, Raman spectroscopy allows to access the vibrational modes of atomic bonds

through the intimate relation of light-electron interactions coupled to vibrations of the lattice. Over time, it emerged as a very successfully tool for characterizing the structural properties of matter. A review can be found in [42].

This work utilized Raman spectroscopy to obtain information about the material quality of graphene and polycrystalline diamond. For this purpose, a Horiba LabRAM HR system with a 532 nm was used. Optical filters can be chosen to reduce the power incident on the sample to prevent destruction of sensitive samples. Even though graphene has an exceptionally high thermal conductivity, applying a high power onto graphene resulted in burning the material away from the substrate. Applying a high enough power on a homebuild Raman tabletop laser setup, succeeded to even cut heavily doped diamond thin films. Lowly doped diamond films remained intact, due to their high transparency.

3.1.1 Raman Spectroscopy of Graphene

Raman spectroscopy allows to determine the number of layers [43], their orientation, the type and quality of edges, doping, strain, disorder and a plethora of other properties and effects around graphene. Ferrari and Basko summarize the information that can be obtained on graphene from Raman spectroscopy in their review article [44]. Ferrari et al [43] were the first to provide Raman spectra of graphene in 2006, shortly after the intial discovery of graphene by Novoselov and Geim. Figure 3.1 shows the Raman spectra of graphene, multilayers of graphene and graphite. Two signals are characteristic of carbonic sp^2 bonds, namely the G-band around 1580 cm^{-1} and the 2D band around 2700 cm^{-1}, shown in figure 3.1a. The precise peak position evolves with the number of layers and has different values for different excitation wavelengths of incoming light, e.g. green light of 514 nm in figure

3.1b and red light of 633 nm in figure 3.1c. Strain-free and atomically clean graphene has a G-peak at 1584 cm^{-1} and the 2D-peak around 2675 cm^{-1}. Now, graphene's fingerprint in a Raman spectrum shows in at least two ways. Once, the form of 2D peak is highly symmetrical compared to two or more layers of graphene. Secondly, one can compare the intensity of the 2D peak I_{2D} to the intensity of the G peak I_G. The ratio of $I_{2D}/I_G \sim 2$ for monolayer graphene, $I_{2D}/I_G \sim 1$ for bilayer and $I_{2D}/I_G < 1$ for more then two layers of graphene. Thus, graphene can be identified unambiguously by one or the other criteria.

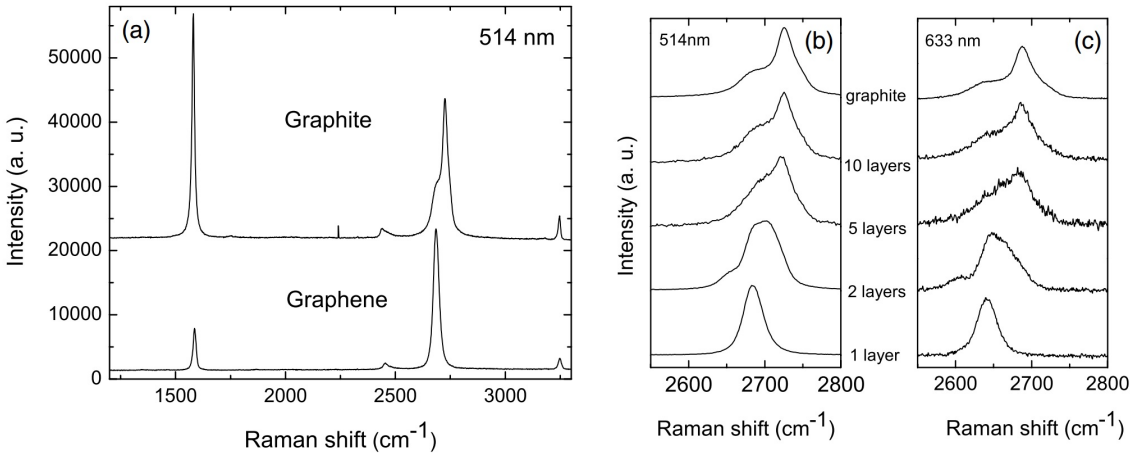

Figure 3.1: Stokes Raman spectra for graphene and multiple layers of graphene. Scaled to show similar height of the 2D peak around 2700 cm^{-1} [43].

3.1.2 Raman Spectroscopy of Diamond

Individual diamond grains in single- and polycrystalline diamond

Diamond grains exhibit a characteristic and symmetric Raman peak at 1332.5 cm^{-1} wavenumbers [45]. The Raman line width, full width at half maximum, is a measure of structural disorder and depends on the diamond growth method. Figure 3.2 shows the evolution of the linewidth for different growth conditions. GE Diamond was prepared synthetically under high pressure, natural diamond is a gem quality stone, carbonado is a

black polycrystalline diamond with interlocked crystallites and the rest of the samples are CVD diamond films grown under different conditions [45].

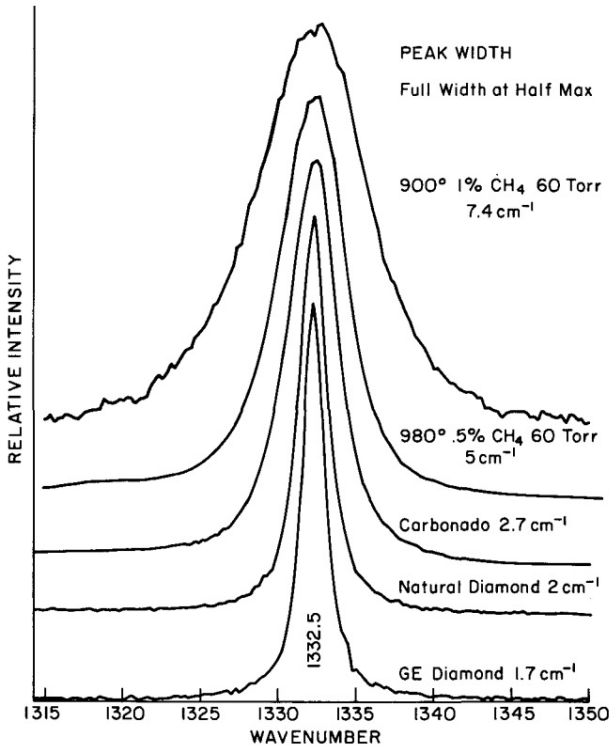

Figure 3.2: Stokes Raman spectra of individual diamond grains of single-crystal diamond and diamond films with a 514.5 nm excitation laser [45].

A linewidth smaller than 2 cm^{-1} indicates a very small amount of structural disorder in natural and high pressure grown samples. On the other hand, CVD samples with the growth of methane as a precursor show a considerable amount of broadening and structural disorder with linewidths between 5-7 cm^{-1} within an individual diamond grain. The grain size of the diamond films in figure 3.2 is between 10-20 μm, with the focus of the Raman spectrometer $\approx$ 1-2 μm. Thus, the structural disorder can be understood in terms of disorder generated inside the grain during CVD growth and not the grain boundaries. A shift of the peaks position towards lower or higher wavenumbers has been

interpreted previously as internal tension or compression of the diamond film with respect to the substrate [45]. A calibration curve was determined in [46] from measurements in an anvil cell. Furthermore, the position and the shape of the 1333 cm^{-1} line depend on the polarization of the incoming light [47]. Thus, care is required when making conclusions of the quality of the crystal and its internal stress state.

Undoped polycrystalline diamond films

Revealing the detailed nature and composition of a polycrystalline diamond films becomes considerably harder. Polycrystalline diamond consists of individual single crystal grains (section 1.3.1) interconnected through grain boundaries (section 1.3.2). Different phases of sp^2 and sp^3 carbon can be observed either within a grain or at the grain boundaries. Single crystal sp^3 diamond can be accompanied by graphitic carbon, disordered sp^2 bonds like amorphous carbon or diamond-like carbon, each with their own characteristic signature in a Raman measurement. They can be found within the 1000-2000 cm^{-1} band of the Raman spectrum excited by a laser source of visible light. Signals between 2500-3000 cm^{-1} give insights about natural, polycrystalline or highly oriented graphite as well as glassy carbon structures in the samples [45]. Raman spectra of the top surface of the polycrystalline diamond foils on a Si/SiO_2 substrate with different doping and surface termination are shown in figure 3.3. Only the undoped diamond foil is on a quartz substrate. As grown samples refer to a hydrogen terminated surface, which prevails after removing the foil from the CVD growth chamber. Oxygen plasma treatment changes the surface termination to an oxygen termination. The Raman spectra showed different peaks and bands at 521, 1175, 1332, 1450 and 1500-1525 cm^{-1}. The 521 cm^{-1} silicon Raman line is used to calibrate the

diamond Raman spectra with respect to each other. A clear sp^3 diamond peak is visible at 1332.5 cm^{-1} with a width of 10 cm^{-1} and 12 cm^{-1} [45], for 266 ppm boron doped hydrogen terminated and 10k ppm oxygen terminated diamond, respectively. The relatively large linewidths might result from inclusion of grain boundaries in the laser spot (diameter 1-2 μm) during measurement. The grain size ranges anywhere from 10-20 nm (bottom side of the film) to 50-500 nm (top side of the film). Thus, deviations from a perfect single crystal signal are expected and result in an enhanced linewidth of the sp^3 diamond peak. Raman peaks at 1175 and 1450 cm^{-1} usually appear hand in hand and have previously been attributed to trans-polyacetylene, a polmeric one-dimensional carbon chain at the grain boundaries [48, 49]. Amophous carbon, more specifically diamond-like carbon in the form of hydrogenated amorphous carbon (a:C-H, see section **??**), is the origin of the 1525 cm^{-1} peak [50] for an excitation wavelength of 532 nm. Raman signals of amorphous carbon appear in a range of around 1460 cm^{-1} to 1560 cm^{-1}.

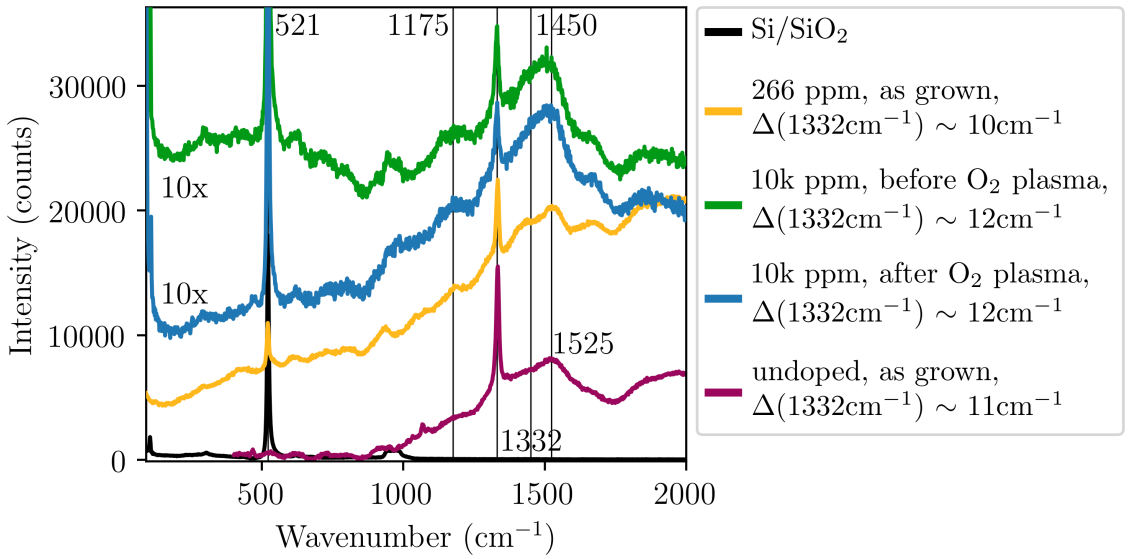

Figure 3.3: Raman spectra of different polycrystalline diamond foils. Δ indicates the full width half maximum of the diamond peak.

The ratio of the amorphous carbon peak to the 1332 cm^{-1} sp^3 line is a measure of the diamond film quality. Measurements of even smaller amounts of sp^2 carbon bonds are possible, because the scattering efficiency of sp^2 carbon is around 56 times larger than for sp^3 carbon, for an laser wavelength of 514.5 nm [51]. For a short review see [52].

Boron doping of polycrystalline diamond films

Regular Raman spectroscopy for boron doped diamond in the visible light, does not yield a signal of the B-C vibrational modes. Nonetheless, a qualitative comparison of Raman spectra can be made. The gas mixture of the dopant during the CVD process is not a linear function of the actual doping in the grown material and it depends on different factors. The most important is the growth direction. For example, one order of magnitude more boron is incorporated in grown {111} facets of single crystals then for {100} single crystal facets of 4-10 μm size on a Si(100) substrate, as discussed by Ushizawa [53] within secondary ion mass spectroscopy data. Furthermore, the boron doping level has a strong effect on the growth direction of the crystal. While for 200ppm boron to carbon (B/C) the {111} and {100} facets appeared with almost equal numbers, for 5500ppm B/C the number of {111} facets increased steadily to a degree where {111} facets were found to dominate in numbers. In the same paper, Raman spectra of 514.5 nm laser excitation have been provided for facets of single crystal diamond and doping levels from 0 to 10k ppm of B/C. Figure 3.4 shows their measurements for very low doping from 0 to 40 ppm B/C.

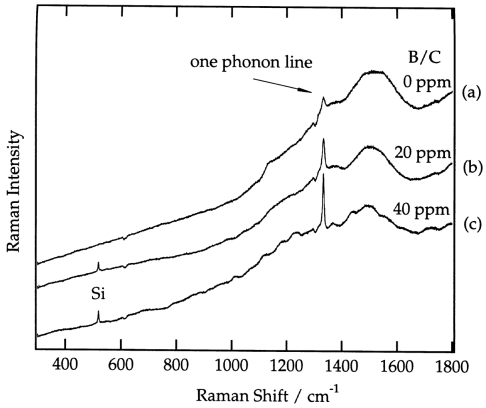

Figure 3.4: Raman spectra of lowly doped diamond grains. From [53].

Doping above 40 ppm B/C is shown in figure 3.5, for {100} and {111} facets on the left and right plot, respectively. Ushizawas measurements provide a qualitative guideline for determining the doping level of boron doped diamond for relatively high concentrations. Their results can be extrapolated for polycrystalline diamond films to get only a very rough estimate of the doping level since stress, orientation a crystal facets can strongly vary within such a film. Infrared spectroscopy or secondary ion mass spectroscopy measurements provide a more reliable route to determine the boron concentration after film growth.

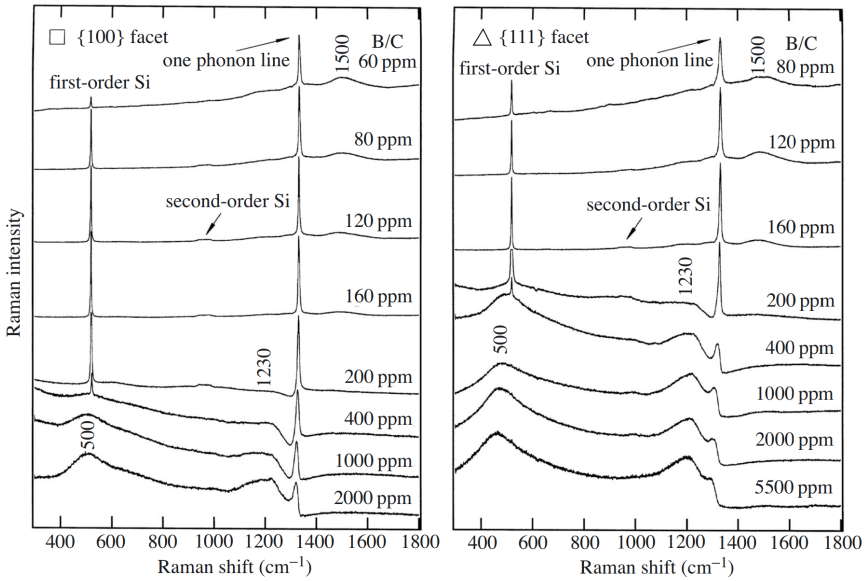

Figure 3.5: Raman spectra of doped diamond grains over a wide doping range [53].

3.2 Electronic measurements

3.2.1 High Temperatures

High temperature measurements were performed in a Lindberg/BlueM TF55035A furnace within a quartz tube under nitrogen flow, as shown schematically in the left picture of figure 3.6. The device under investigation (DUT) is placed in the middle of the open-ended quartz tube, which is wrapped with aluminium foil connected to ground. Aluminium shields the DUT from an electronic feedback loop from within the furnace, controlling the temperature and coupling into the current voltage measurements.

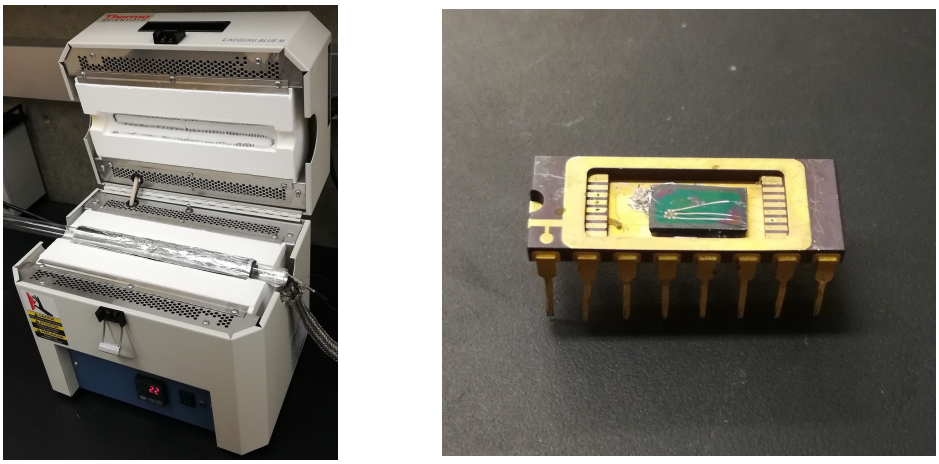

Figure 3.6: Left: High temperature measurement setup. Right: Sample positioned in sample holder and connected with wire bonds.

The DUT is mounted on a side braze sample holder (Spectrum Semiconductor Materials SSM P/N CSB01652), and is connected to low resistive 27% nickel clad copper wires (Kulgrid 28 Ceramawire) with an outer insulating ceramic high temperature resistant coating. Connector pins are added to one end of the high temperature wire, in order to manually connect the wire and the sample holder. The connector pin and the high temperature wire are are epoxied with a two component high temperature silver conductive

T(°C)	22	100	150	200	250	300	350	400	450	500
R (MΩ) @ 1V	6000	5000	4500	4000	1000	333	100	19	8	3

Table 3.1: Temperature versus resistance between two adjacent pins of a sample holder caluclated from leakage currents between 22°C and 500°C, which increase around 300°C.

epoxy (Ted Pella H20E Epo-Tek), in order to ensure good electrical conduction at high temperatures. The measurement setup with the sample holder was tested for possible leakage currents, occurring at elevated temperatures in a open circuit configuration between two adjacent pins of the sample holder, see table 3.1. The measurement procedure versus time for heating up and cooling down is illustrated in figure 3.7 in a temperature range of 22°C up to 300°C. During the heating procedure the sample is hold at constant temperature for a certain amount of time to allow for measurements of megasweeps, e.g. holding the backgate voltage constant while sweeping the source drain voltage. Likewise, while the temperature is ramped up to the next temperature plateau, the current-voltage characteristics are recorded at constant backgate voltage. The heating is set to a constant rate. During cool down a similar measurement procedure can be performed, or alternatively, the furnace can be opened which allows the sample to reach lower temperatures faster, see right panel in figure 3.7. A single function cannot fit the cooling temperature well. Thus, piecewise fitting of the data points allows to properly extract the temperature.

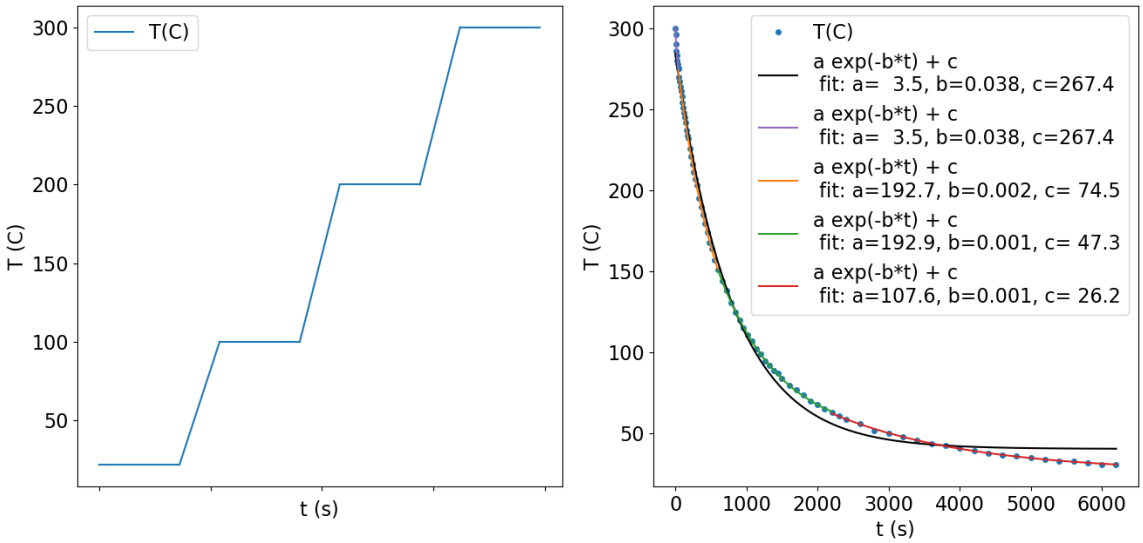

Figure 3.7: Left: Heating procedure with periods of constant temperature and constant ramp up. Right: Decay of the cool down after the furnace is opened. Piecewise fitting is required to properly describe the data, since a single fit does not provide a good result.

Chapter 4

Hopping Conduction

4.1 Impurity Conduction

Doped semiconductors can exhibit thermally activated conduction through impurities which is referred to as impurity conduction. It was first observed by Labhardt and Busch on silicon carbide in 1945 [54]. During the process of impurity conduction in semiconductors a charge carrier will tunnel or hop from a filled impurity site to an empty impurity site, due to a small but finite overlap of a localized wavefunction with the empty site. During that process the charge carrier is not entering or activated into the conduction band [55]. The energy levels of the impurities lie below/above the conduction/valence band for n-type/p-type conduction, respectively. At elevated temperatures electrons/holes of high mobility in the conduction/valence band have the largest contribution to the conductivity while at low enough temperatures impurity conduction dominates, e.g. when the thermal energy is not enough to excite the electron/hole into the conduction/valence band. Then impurity conduction will show thermally activated behavior to its closest neighbours, re-

ferred to as nearest neighbour hopping (NNH), given that the neighbouring site is free. In general the conductivity of lightly doped semiconductors takes the form

$$\sigma(T,N) = \sigma_1 \exp(-\varepsilon_1/k_BT) + \sigma_2 \exp(-\varepsilon_2/k_BT) + \sigma_3 \exp(-\varepsilon_3/k_BT) \tag{4.1}$$

where $\varepsilon_1(N,K), \varepsilon_2(N,K), \varepsilon_3(N,K)$ are all functions of the number of impurities N and the compensation K, and represent the activation energies to the conduction band, to the upper Hubbard band and hopping between impurities, respectively. The Hubbard band is a result of considering interaction between particles in a lattice. The activation energies follow the relation $\varepsilon_1 > \varepsilon_2 > \varepsilon_3$ according to their positions in a band diagram. Fritzsche and coworkers identified the three different activation regimes for the first time in p- and n-doped germanium in successive experiments in 1955 [56] and 1958 [57].

Compensation K plays a critical role in which of the activation energies will dominate at fixed temperatures. Impurity conduction will play a role for lightly doped and compensated samples and nearest neighbours hopping (NNH) between impurities will occur. Impurity band conduction is very sensitive to the concentration of the impurities, e.g. for germanium a change of 30 for the impurity concentration results in a change of 10^7 for the conductivity. Heavy doping of the semiconductor can result in metallic behavior, when the impurity concentration is bigger than a critical density such that $n > n_C$.

4.2 Anderson Localization and the Mobility Edge

In 1977, Anderson, Mott and van Vleck received the Nobel Prize in Physics "for their fundamental theoretical investigations of the electronic structure of magnetic and disordered systems" [58]. In particular, Anderson investigated the question of diffusion

of electrons in random lattices in 1957 [59] for electronic transport problems that involve quantum mechanical movement of entities, such as electrons or holes or spins, from one state $|i\rangle$ to another state $|j\rangle$. Furthermore, randomness was a crucial element involved in this process, such as a random distribution of the lattice sites, a random energy distribution $P(E)dE$ of the energy states at different sites or a random distribution of the matrix transfer element V_{ij} from initial to final state. Anderson specified that the lattice site distribution or the matrix transfer element can possibly be regular but that the energy distribution of the states requires randomness. He found that localization of the entity that occupies a state is possible and that transfer from one to the other site can occur, provided overlap of the wavefunctions exists. A second conclusion was that no transport at all is possible. A true stationary state of the entity at hand, in a sense that the probability amplitude of a particle at a specific site does not diffuse away over time. Nowadays, the localization of any entity in such a transport problem is referred to as **Anderson localization** and its required randomness is called a **disordered system**. In general, localization is a wave phenomena and can occur for electromagnetic waves [60], sound waves [61], elastic waves [62], Bose Einstein condensates [63], et cetera.

The counterpart to a localized entity in a disordered medium is a delocalized entity in a ordered medium. Around 1928, Felix Bloch [64] considered the movement of the electron in a perfectly periodic potential $V(\vec{r}+\vec{R}) = V(\vec{r})$ for all $\vec{R}$ in a Bravais lattice by solving the Schrödinger equation

$$H\,|\psi\rangle = \left(-\frac{h^2}{2m}\nabla^2 + V(\vec{r}\right)|\psi\rangle = \varepsilon\,|\psi\rangle \tag{4.2}$$

for eigenstates $|\psi\rangle$ in the form of a planar wave $\exp(i\vec{k}\vec{r})$ times a periodic function $u(\vec{r})$ with

the exact same periodicity as the Bravais lattice

$$|\psi\rangle = \exp(i\vec{k}\vec{r})u(\vec{r}). \tag{4.3}$$

Such an eigenstate of the electron for the above Hamiltonian corresponds to a delocalized electron free to move around the lattice and is called a **Bloch wave**. Including the thermal motion of the periodic lattice at non-zero T gives raise to a finite free wavelength restricting the movement of electrons. Hence, with increasing temperature the resistivty of a metal increases.

In contrast, a localized wave function in the sense of an Anderson localization has an exponentially decaying envelope

$$|\psi\rangle = \exp(-\alpha(r - r_0))\,|\psi_0\rangle \tag{4.4}$$

where α is the exponential decay length, $1/\alpha$ the localization length, and $|\psi_0\rangle$ the wave-function below the envelope depending on the specific system under consideration. In the limit of $1/\alpha \to \infty$ the case of an extended state is recovered.

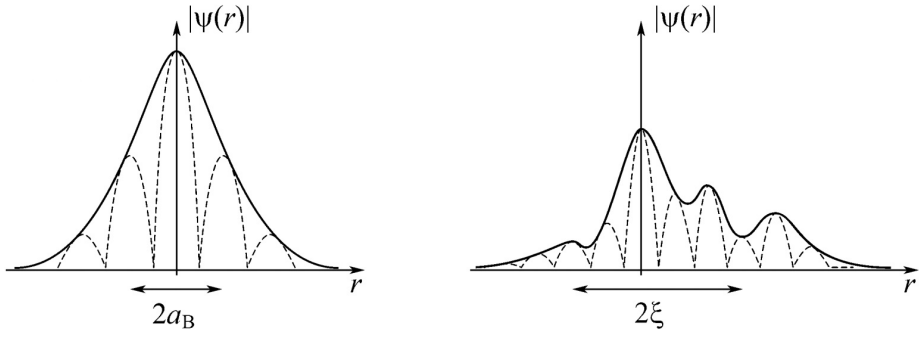

Figure 4.1: Left: Strongly localized state at a single impurity. Right: Localized state in close proximity to the metal-insulator transition. Reprinted from [65]

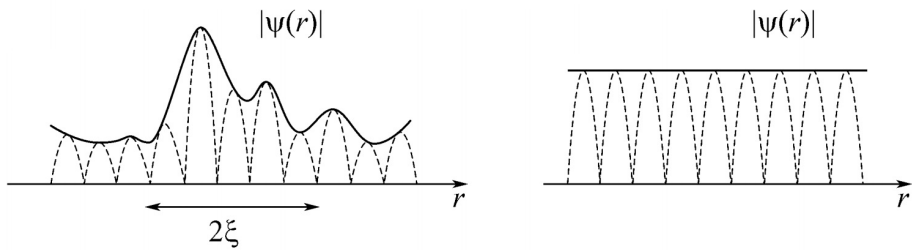

Figure 4.2: Left: Delocalized charge carrier after the metal-insulator transition. Right: Delocalized state extending over a wide range. Reprinted from [65]

Now one may inquire about the nature of a system, when it changes from a delocalized to a localized one. Anderson showed that such a transition is possible in general and Mott persisted strongly enough to introduce the concept of a sharply defined **mobility edge**. The terminology of a mobility edge was chosen such that when the Fermi energy E_F lies above the mobility edge charge, carriers can move with characteristics similar to delocalized states, also called extended states. When the Fermi energy lies below the mobility edge, then transport of charge carriers is dominated by effects of localized nature, such as variable range hopping. Schematically, this is shown in figure 4.3

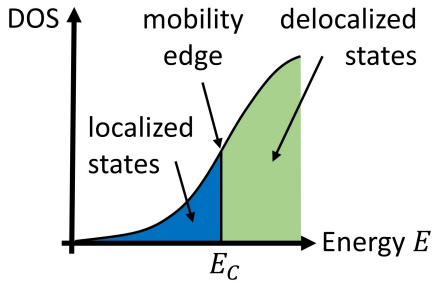

Figure 4.3: Density of states versus energy E. Below/above the mobility edge E_C conduction is through localized/delocalized states.

For the case of a polycrystalline wide bandgap semiconductor like diamond, it is possible to transition between localized states ($E_F < E_C$) and delocalized states ($E_F > E_C$) by increasing the amount of disorder through doping. Then, the insulator undergoes a

transition to a metal, widely referred to as an **Anderson transition**. Delocalized states in heavily doped insulators and delocalized states in ordered metals in the form of Bloch waves originate from two different physical systems. Delocalization in ordered metals is the result of perfect translational symmetry of the lattice, while Anderson localization is the result of randomness of the energy distribution of occupied states. Delocalization in the sense of a mobility edge occurs upon increasing the amount of doping in a disordered medium. The random distribution of energy states under light doping is discrete, upon increasing the doping, the discrete distribution transforms into a band of continuous states, the impurity band (section 4.1). Interesting phenomena have been investigated at the Anderson transition, like multifractality of critical wave functions or criticality in the power law, which are just named here and summarized elsewhere. For a review see [66].

4.3 Variable Range-Hopping

4.3.1 Temperature Dependence of Variable Range Hopping

Variable-range hopping (VRH) is an electrical conduction mechanism describing charge transfer through localized states arranged in a non-periodic manner [67]. It was first observed in 1967 on studies of amorphous germanium by Clark [68], Walley&Jonscher [69], and by Walley [70] on germanium/silicon as a characteristic non-linear plot of $\log(R)$ vs $1/T$. A constant activation energy E_A could not be inferred from their plots as the log resistance changed non-linearly with the inverse temperature. Such a behaviour is characteristic of variable range hopping conduction. Mott was the first to derive a temperature dependent

conductivity σ at low electrical bias (linear regime) for this process [67, 71]

$$\ln(\sigma) = A - B/T^{1/4} \tag{4.5}$$

where A and B were initially unspecified. It turns out that A exhibits a temperature dependece of the form $\ln\sigma_0(T)$, which is usually masked by the inverse $T^{1/4}$ factor and of weaker dependence on the overall conductivity. This was the starting point of a more rigorous endeavor into VRH transport of localized states with a wide literature body nowadays. An attempt is made in this chapter to give an overview of the most important works and phenomena of this and related mechanisms. Mott's VRH equation (4.5) applies to a specific case of hopping at constant density of states around the Fermi level in three dimensions. Hopping at constant density of states around the Fermi level can also occur in quasi one dimensional nanowires or disordered two dimensional sheets of atoms and hence a more general form of the temperature dependence of VRH [72] is given by

$$\sigma(T) = \sigma_0 \exp - \left(\frac{T_0}{T}\right)^{\frac{1}{1+n}} \tag{4.6}$$

where n =1, 2, 3 represents the number of dimensions.

Pollak [73] considered percolation theoretical treatment of VRH in three dimensions for the case of a non-constant density of states $N(E)$ of the form $N(E) = A \mid E - E_F \mid^m$ and deduced

$$\sigma(T, m) = \sigma_0(T, m) \exp - \left(\frac{T_0}{T}\right)^{\frac{m+1}{m+4}}. \tag{4.7}$$

Factors $\sigma_0(T, m)$ and T_0 were provided for the case of Mott VRH hopping ($m = 0$) and thermally activated conduction through an impurity band ($m \to \infty$) in which case the density of states shows a strong and sudden increase somewhere away from the Fermi level.

In detail,

$$\sigma(T, m = 0) = (78Ca)^{-1}(k_B T a^3 v)^{-1/4} \exp\left[-1.82(v k_B T a^3)^{-\frac{1}{4}}\right]. \tag{4.8}$$

where T_0 in the exponent is a function of v the denisty of localized states, a the inverse decay length of an assumed hydrogen like localized state and k_B the Boltzmann constant. The exponential prefactor σ_0 depends inversely on the fourth square root of the temperature and includes a constant C from the derivation of the percolation problem. In the limit $m \to \infty$ equation (4.7) describes the process of thermally activated impurity band conduction

$$\lim_{m\to\infty} \sigma(T, m) = (160 C r_s N_s a^3 k_B T / \langle\Delta\rangle_m)^{-1} \exp(2.4 r_s/a) \exp(e^2/\kappa r_s k_B T) \tag{4.9}$$

where $\langle\Delta\rangle_m$, r_S, N_s, κ can be found in [73]. For cases other then $m = 0$ or $m \to \infty$, the factors T_0 and σ_0 need to be calculated according to the procedure applied in Pollak's approach [73]. The crossover between VRH and impurity band conduction is discussed in section 4.3.3.

Motivated by Pollak's calculations, Hamilton [72] confirmed the exponential temperature dependence of VRH in three dimensions and provided a temperature dependence in two dimensions. His derivation was based off Mott's original approach instead of a percolation treatment of the problem. Apsley and Hughes [74] introduced a simple method following Mott's original approach, though without the simplifying relation between hopping energy and hopping distance. They extended their work in [75] to a more general approach including a non-constant energy-dependent density of states, a Fermi-Dirac distribution of states above and below the Fermi energy and the effect of an applied electric field. In comparison to Pollak's work, Apsley and Hughes calculated a mobility which is integrated to obtain a conductivity while Pollak calculated a critical conductance from a

network of resistances. Surprisingly, as will be seen at the end of this section, both approaches yield very similar results in the case of temperature driven VRH for a constant density of states. Apsley and Hughes held their approach and expressions general to the point where progress in their calculation could only be achieved by simplifying assumptions to obtain analytical closed form solutions. This was only possible for the easiest case of a constant density of states while any other forms of density of states requires numerical integration of their expressions. Their calculation resulted in a solution for the temperature T and electric field F dependence of the conductivity $\sigma(T, F)$ for the case of three dimensions. A unitless parameter $\beta = eFa/2k_BT$ was introduced to distinguish between three scenarios from where the charge carrier obtains its energy for VRH to occur: For small β the energy mainly comes from the scalar temperature reservoir, while for large β the energy mainly comes from the electric field potential. In the intermediate region, for $\beta \sim 0.5$, the energy contributions from the electric and the thermal energy mix on similar energy scales. For small β, the Ohmic regime reads

$$\sigma(\beta, T) \sim \frac{Ne^2 v_{ph}}{2\alpha^2} \left(\frac{24\alpha^3}{N\pi k_B T} \right)^{1/4} exp\left[- \left(\frac{24\alpha^3}{N\pi k_B} \right)^{1/4} \frac{1}{T^{1/4}} \left(1 - \frac{\beta^2}{4} \right) \right] \tag{4.10}$$

with N the density of states, α the decay length of an assumed hydrogen like localized state, e the electron charge and v_{ph} the hopping frequency. Hence in the limit of $\beta \to 0$ equation's 4.8 functional dependence is recovered and only the numerical factor in T_0 differs slightly $(24/\pi)^{1/4} = 1.66 \neq 1.82$, by less then 10%. The case of large β will be covered next.

4.3.2 Electric Field Dependence on Variable Range Hopping

When the charge carrier obtains most of its energy for a variable range hop from the electric field, then the unitless parameter $\beta = eFa/2k_BT >> 1$. Then, the conductivity can be written as

$$\sigma(F,T) \sim \frac{Ne^2 v_{ph}}{4\alpha^2}\left(\frac{64\alpha^4}{N\pi eF}\right)^{1/4} \exp\left[-\left(\frac{64\alpha^4}{N\pi e}\right)^{1/4}\frac{1}{F^{1/4}}\right] \tag{4.11}$$

with the parameters as described in section 4.3.1. Again, the exponential term $\exp(-1/F^{1/4})$ has a stronger influence on the overall conductivity and will mask the $1/F^{1/4}$ component in the prefactor and hence the famous $\sigma(F) \sim \exp(-1/F^{1/4})$ is obtained. Pollak has obtained the same functional dependence in the voltage regime through a percolation treatment [76].

4.3.3 Crossover between Impurity Band and VRH conduction

Usually, experimental results for conductivity at low electrical bias (linear regime) show a crossover between Mott's VRH at low temperatures and thermally activated impurity band conduction at higher temperatures. Pollak [73] obtained the crossover temperature T_c as

$$T_c = 0.28(E_0/k_B)a\left(\frac{4}{3}\pi N E_0\right)^{\frac{1}{3}} \tag{4.12}$$

where E_0 is the activation energy in the impurity band regime, a the localization radius, and N the constant density of states. E_0 can be extracted from a plot of $\ln(\sigma)$ versus $1/T$, as pictured schematically in figure 4.4, where the slope of the straight line in the $1/T$ region equates to E_0/k_B. Care needs to be taken to make sure the activation energy is extracted from a section that is a straight line over a sufficiently large temperature window. Otherwise, one might interpret the data to be thermally activated, while in fact the data

exhibits a different functional form than $1/T$. A good method to make sure the Arrhenius plot actually follows $1/T$ is discussed around figure 4.6.

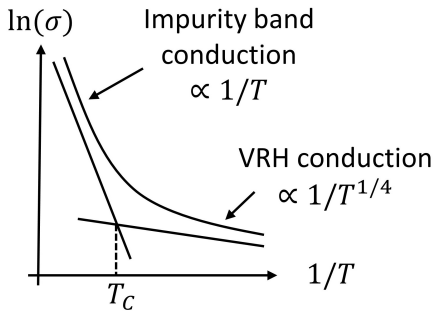

Figure 4.4: Schematics of a crossover between impurity band conduction and VRH at the crossover temperature T_c.

4.4 Conductivity Measurements of Low and High Doping

We fabricated and measured boron-doped diamond polycrystalline films of low (266 ppm) and high (10 kppm) doping. In figure 4.5, the logarithm of the low bias conductance G versus $1/T$ is displayed. A schematical side-view and exemplary optical image can be found in figure 2.9. The plot shows a graphene sample, two diamond samples, and two diamond-on-graphene heterojunction devices. The low bias resistance of the diamond-on-graphene heterojunction (10k ppm) varied from 22.05 kΩ at room temperature to 4 MΩ from 20K to 4.2K, where it saturated. It was ≈ 3 orders of magnitude larger than the bare diamond top surface, which measured 90 Ω and 1300 Ω at room temperature and 4.2K, respectively, after subtracting the wiring of the electronic setup. Lowly doped samples follow a similar pattern, where the top surface shows an enhanced conductance. Though, the overall conductance of lowly doped samples is considerably lower and exhibits a larger change of its overall conductance by ≈ 12 orders of magnitudes going from room temperature down to low temperatures. The surface conductivity of diamond is known to

exhibit an enhanced conductivity of the surface due to a hydrogen termination of the diamond top atoms, which is the regular termination of dangling diamond bonds after PECVD growth. More precisely, a top layer of adsorbates in combination with a hydrogen terminated diamond surface creates a conductive hole layer [77], which in return enhances the conductivity. Without adsorbates from the air, no enhancement of the surface conductivity is observed.

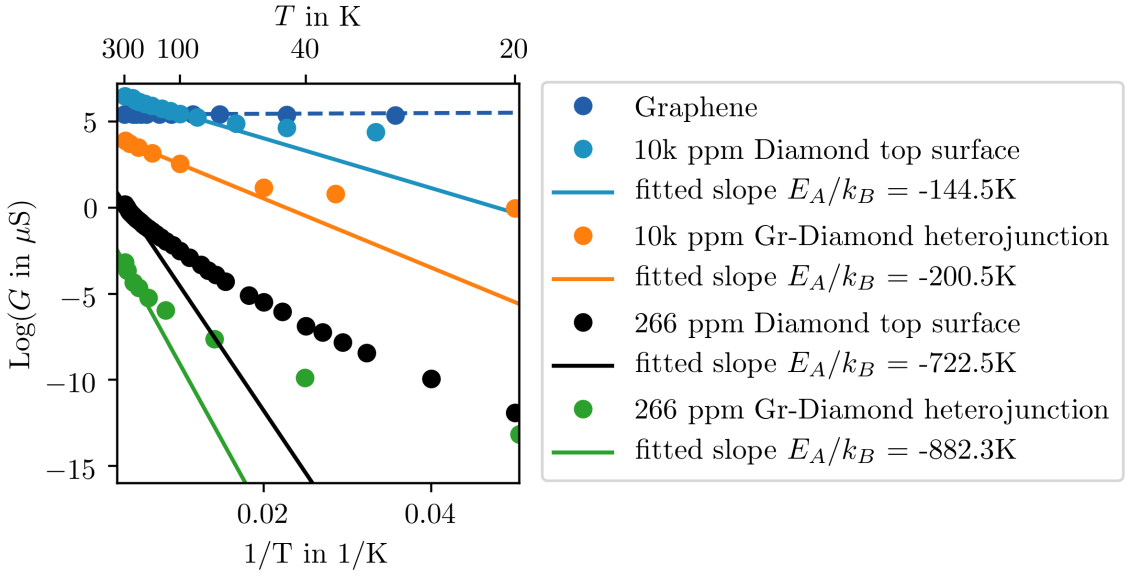

Figure 4.5: Arrhenius plot of lowly and highly doped diamond samples, probing either the top surface or the bulk electronic properties. A top axis is included for better readability.

Furthermore, the figure shows fitted slopes for 300K to 200K, from which one can extract activation energies E_A. Graphene's activation energy is zero as expected from a semi-metal. E_A for 10kppm doped surface/bulk sample yields 12.5meV and 17.3meV, and for the lowly doped sample 62.3meV and 76.0meV, respectively. From consideration of the slopes, it is evident, that the low temperature activation energies differ from the high temperature ones, implying that our data does not follow a simple Arrhenius relation of the form $1/T$ at low temperatures. A common conclusion drawn in literature is to claim a non-

linear Arrhenius plot as a fingerprint for VRH transport. Specifically, electronic transport of doped diamond is commonly explained in terms of VRH down to cryogenic temperatures [78]. Usually a plot of $\ln(\sigma)$ vs $1/T^{1/4}$ with a straight slope is interpreted as VRH in 3D without Coulomb interactions, according to relation (4.5). Such an interpretation can turn out to be merely fortuitous. It is more appropriate to perform a data analysis that determines the exponent of the temperature more precisely.

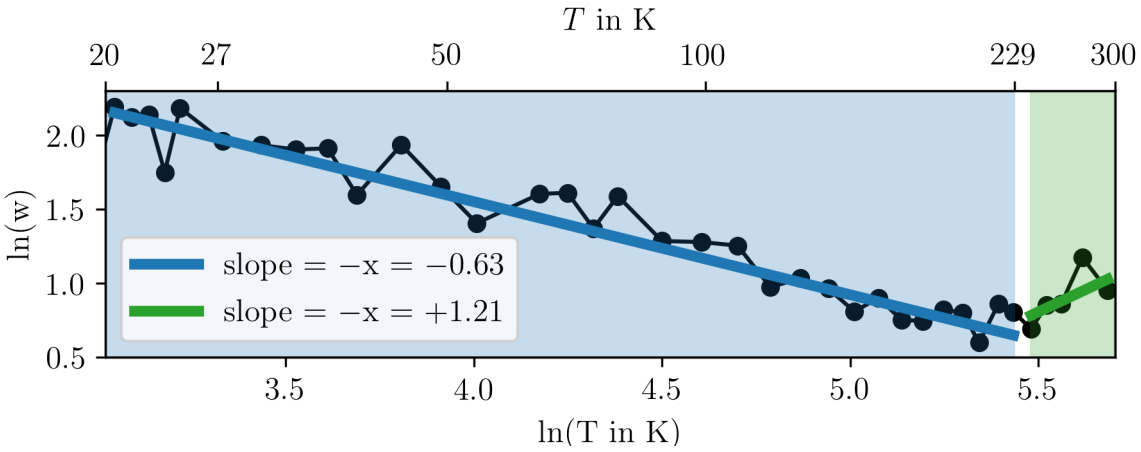

Figure 4.6: Analysis of exponent.

Zabrodskii [79] performed such an analysis by defining a dimensionless activation energy $w(T) = \partial \ln G(T)/\partial \ln T = m + x(T_0/T)^x$, where x is the exponent in $G(T) = G_0 \exp[-(T_0/T)^x]$ and m is a factor that includes the temperature dependence of the prefactor G_0. If G_0 is only weakly dependent on T, as is commonly assumed throughout the analysis of VRH, then a plot of $\ln(w)$ versus $\ln(T)$ will yield x as the negative slope. Figure 4.6 shows the analysis of the exponent x for the lowly doped diamond surface, since only this curve had enough data points for numerical derivatives to yield reliable results. Two regions are visible. From 20K to 230K the factor of x takes the value 0.63, which is above the value of 0.5 for VRH in 3D with Coulomb interactions. Furthermore, above

230K the temperature dependence in the exponent flips such that $G(T) \propto \exp[-(\mathrm{T}/\mathrm{T}_0)^{1.23}]$. Surprisingly, simple impurity conduction where $G(T) \propto \exp[-(\mathrm{T}_0/\mathrm{T})^1]$ is not observed.

Chapter 5

Dissipative Quantum Tunneling

Deep doping of wide bandgap semiconductors provides a unique platform to explore quantum mechanical effects within condensed matter physics. One such platform is boron-doped polycrystalline diamond. As we have seen previously (sections **??**), diamond can be doped with different atoms. Most reliably with boron. It can be introduced deep into the bandgap, 370 meV above the valence band where it acts as an acceptor. Holes become the majority charge carrier in such a system. Below a boron doping concentration of $\approx 2 \cdot 10^{20}$ cm^{-3} diamond remains on the insulator side of the insulator-metal transition and holes are not free to move like in a metal. They are strongly localized within a quantum well, in the sense of an Anderson localization. Quantum mechanical effects, like the tunneling effect coupled to the environment, play an important role in determining charge transport in such systems. This chapter discusses those effects and is set up in a non-traditional way such that mathematical relations to understand measurements are presented first and held to a minimum. This is followed by our experimental measurements. Thereafter, a more

detailed summary of dissipative quantum tunneling theory and its underlying assumptions is presented. Agreements and discrepancies of theory and experiments are pointed out, followed by a discussion of possible mechanisms that could lead to such deviations.

5.1 Closed and Open Quantum Systems

A quantum mechanical system can be considered as either open or closed. The most prominent example of a closed quantum system is a two-level system like a spin-1/2 particle, e.g. an electron or a hole. Such a two-state quantum system can be described by the superposition of its two energy eigenstates. Unless the system is initially prepared in an energy eigenstate or it is degenerate, it will exhibit Rabi oscillations. The system is considered to be a closed quantum system, because the environment is not taken into consideration. In general, any physical system will be embedded in an environment, like a solid, a liquid, a gas, a plasma or vacuum/space itself. Depending on the physical system and the type of environment at hand, the coupling between each other can be strong, weak or non-interacting. The coupling will depend on the specific parameters used such as energy, time, doping, elastic constants etc., where the coupling can be either on or off, or can have an in between value. If the coupling is turned on, energy can be exchanged between system and environment, e.g. when energy dissipates away from the system into the environment, or vice versa is introduced into the system by the environment, see figure 5.1.

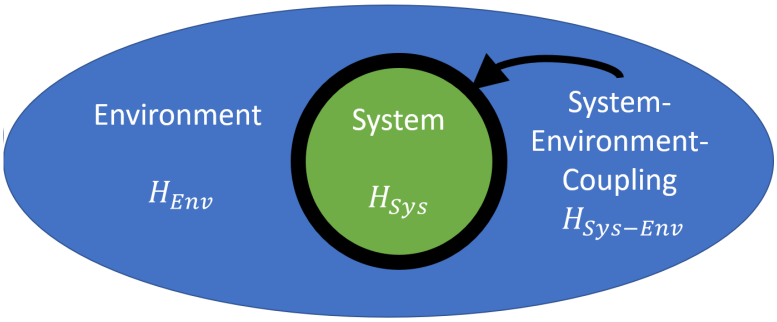

Figure 5.1: Closed and open quantum system. A closed quantum system is solely described by its Hamiltonian H_{Sys}. An open quantum system incorporates the environment and a coupling term such that the total Hamiltonian $H_T = H_{Sys} + H_{Env} + H_{Sys-Env}$.

5.2 The Double Quantum Well Model

Dissipative quantum tunneling is the process of quantum mechanical tunneling of a particle through a potential barrier, where energy dissipates away into the environment or can be introduced by the environment into the system. An extensive discussion of dissipation on quantum tunneling was presented by Caldeira and Leggett in 1983 in their innovative paper on "Quantum Tunneling in Dissipative Systems" [80] for macroscopic tunneling of, for example, trapped flux in a SQUID. In particular, they developed techniques and presented results for quantum tunneling of a system in a localized metastable state into a continuum of states. One of their main results is, that dissipation suppresses quantum tunneling [80]. Successive papers by Grabert&Weiss [81] and Dorsey&Fisher [82] performed calculations applicable to microscopic dissipative tunneling from a localized state into another localized state at finite temperatures. Figure 5.2 illustrates a biased double quantum well with localized states. The underlying assumptions for both quantum wells are $V_0 >> E_0 >> | eV |$ and $E_0 >> k_B T$. The ground state energy E_0 of the localized particle is considerably

larger than the energy provided by the electric field. It is also considerably lower than the potential barrier height, such that thermally activated conduction over the barrier top can safely be neglected.

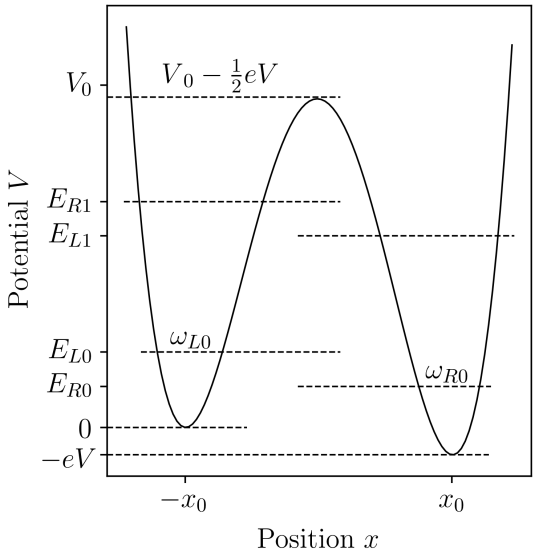

Figure 5.2: A biased double quantum well with localized states. The potential well takes the form $V(x) = c_0 V_0 (x^2 - x_0^2)^2 - c_1 eV(x - x_0)$ with the applied external voltage V and $c_0 = 1/x_0^4$. Small oscillation frequencies in the left and right double well are indicated as ω_{L0} and ω_{R0} with respective ground state energy eigenvalues. The height V_0 of the potential well is reduced due to an applied external voltage $V > 0$.

Excitation of the ground state into its first excited state can be neglected as well. The frequency of small oscillations $\omega_{L0/R0} = (V''_{L0/R0}/M)^{1/2}$ is related to the mass M of the particle and the curvature $V''_{L0/R0}$ of the left and right well, respectively. In a realistic experimental setup ω_{L0} and ω_{R0} can be close to each other or potentially deviate from each other, but for the purpose of this model they are assumed to be the same, $\omega_0 = \omega_{L0} = \omega_{R0}$. The distance between the two minima is $2x_0$ and will be extracted experimentally in section 5.4.

Let's assume that the charge carrier is positioned in the left well at $t = 0$ s with

$V > 0$. Now, one may ask, what is the probability of finding the charge carrier in the right or left well after time t? Experimentally, this can be determined by preparing an array of quantum wells with the same initial conditions, performing an observation at $t \neq 0$ s and counting how many times the charge carrier was in the left or right well. Physically possible, experimentally unfeasible in a condensed matter experiment with doped solids. In theory, Grabert&Weiss [81] and Dorsey&Fisher [82] calculated the probability $P_L(t)$ to find the charge carrier in the left well, explicitly including dissipation of energy into the environment. $P_L(t)$ reads

$$P_L(t) = \frac{1}{2} - \frac{1}{2}\tanh\left(\frac{eV}{2k_bT}\right) + \frac{1}{2}\left[1 + \tanh\left(\frac{eV}{2k_bT}\right)\right] \mathrm{e}^{-\Gamma t} \tag{5.1}$$

where $\Gamma = \Gamma_+ + \Gamma_-$ is the total relaxation rate for forward and backward tunneling rates, Γ_+ and Γ_-, respectively. Expressions for the tunneling rates are provided in the next section 5.3. Let's consider the starting condition $t = 0$ s for which we obtain $P_L(t = 0s) = 1$. The charge carrier is found in the left well, as expected. For $t \to \infty$ the exponential term in (5.1) vanishes, and one needs to consider the two limiting cases of the ratio of electric field energy over thermal energy. For $t \to \infty$ and $eV >> k_BT$ the probability $P_L \to 0$ and the particle spontaneously decays/tunnels into the right well. The particle is localized in the right well. On the other hand, if $t \to \infty$ and $eV << k_BT$, then $P_L \to 0.5$. The particle can be found in either well with equal probability, since probability conservation for a two-well system gives $P_L(t) = 1 - P_R(t)$. If it is not in the left well it must be in the right well. Now, from a classical point of view, this does not necessarily mean that the particle delocalizes in space. It does also not mean that the particle is in both wells at the same time. It merely means that after time t has progressed, we don't have knowledge

of the particles position. We don't know where to find the particle, since we havn't been observing the system. We don't know until we look for it. From a quantum mechanical point of view, the particles wavefunction can be found in the left and right well and upon measurement and collapse of the wavefunction, the particle localizes either in the right or left well. Somehow this point of view is in contradiction with Anderson's idea of absence of diffusion in disordered media. The underlying concept there is that the wavefunction does not diffuse away and does not spread over the lattice but is localized within a certain volume. Most probably the equilibrium extension of the wavefunction of the localized charge carrier is spread over a few quantum wells. Then, initially placing the charge carrier in just a single quantum well will naturally lead for the wavefunction to delocalize over time in a certain volume on a microscopic scale until it reaches its spacial equilibrium extension of an Anderson localized particle. Going back to the discussion of the double quantum well, zero probability is assigned to find the particle within the potential barrier, even though it takes a finite time for particles to tunnel through a barrier. The minimum time t_{min} for tunneling can be estimated as $2x_0/c$, where c is the speed of light. Furthermore, it has been shown recently that tunneling times are finite for electrons tunneling out of argon and crypton atomic potentials [83]. The tunneling time was around 100 attoseconds. In contrast to these results, it was found that for the case of atomic hydrogen the tunneling time was below the experimentally possible resolution of ~ 2 attoseconds [84]. In principal, the observer should be able find the particle in neither the left nor the right well given that the observation is performed faster than the tunneling time. All in all, the tunneling time is assumed to be very small compared to the average time it takes the particle to decay and

zero probability is assigned to find the charge carrier below the barrier top. It is noted, that in the case of no dissipation, when the double quantum well is decoupled from the environment, formula (5.1) takes a very different form and exhibits oscillatory behavior in time, similar to Rabi oscillation in a two level-system [81]. This can be viewed as a closed quantum system (section 5.1) with unitary time evolution.

5.3 Transition Rates and Universal Scaling Behavior

Tunneling transition rates for the biased double quantum well, have been calculated in [81, 82] and a more detailed derivation and discussion of the underlying assumptions can be found in [85], which will be discussed in section 5.10, after experimental results have been layed out in sections 5.4, 5.5 and 5.6. In this section, we focus on the bare minimum to arrive at universal scaling behavior. The **forward transition rate** Γ_+ is given as

$$\Gamma_+ = \frac{\Delta^2}{4\omega_0}\frac{1}{\Gamma(2\alpha)}\left(\frac{2\pi k_B T}{\hbar\omega_0}\right)^{2\alpha-1}\exp\left(\frac{eV}{2k_BT}\right)\left|\Gamma\left(\alpha + i\frac{eV}{2\pi k_BT}\right)\right|^2 \tag{5.2}$$

where Γ is the complex gamma function, ω_0 is the frequency of small oscillations in the biased double quantum well, Δ is the dressed tunneling matrix element, and α is the dimensionless dissipation constant. Incoherent tunneling transport and onset of dissipaton are expected for $\alpha > 1$, coherent transport can be observed for $0 < \alpha < 1/2$, and $\alpha < 0$ corresponds to an unphysical configuration.

The forward transition rate Γ_+ is related to the backward transition rate Γ_- by principle of detailed balance and hence

$$\Gamma_- = \Gamma_+ \exp\left(-\frac{eV}{k_BT}\right). \tag{5.3}$$

Then, the current I, which is carried by the biased double quantum well, is described by the difference of forward and backward tunneling rates

$$I = e(\Gamma_+ - \Gamma_-)\,. \tag{5.4}$$

Putting together formulas (5.2), (5.3), and (5.4) yields

$$I = e\frac{\Delta^2}{4\omega_0}\frac{1}{\Gamma(2\alpha)}\left(\frac{2\pi k_B T}{\hbar\omega_0}\right)^{2\alpha-1}\sinh\left(\frac{eV}{2k_BT}\right)\left|\Gamma\left(\alpha + i\frac{eV}{2\pi k_BT}\right)\right|^2 \tag{5.5}$$

which constitutes the current-voltage characteristics of a single biased double quantum well. In an experimental setup, a chain of N double quantum wells will usually be considered interconnected in series. Then, an additional parameter γ is introduced into equation (5.5), where $\gamma = 1/N$ is the average inverse number of biased double quantum wells or the inverse number of tunneling events and hence

$$I = I_0 T^{2\alpha-1}\sinh\left(\frac{\gamma eV}{2k_BT}\right)\left|\Gamma\left(\alpha + i\frac{\gamma eV}{2\pi k_BT}\right)\right|^2 \tag{5.6}$$

where $I_0 = [e\Delta^2/4\omega_0\Gamma(2\alpha)](2\pi k_B/\hbar\omega_0)^{2\alpha-1}$. Expression (5.6) possesses an **universal scaling behavior**, since plotting $I/T^{2\alpha-1}$ versus eV/k_BT should collapse a set of measured current-voltage characteristics over a wide range of voltages and temperatures onto a single curve. With this definition of γ, the voltage drop across one tunneling event reads γeV. In an experimental setup one will not encounter only a single chain of N double quantum wells in series. A more realistic approximation of an experimental situation will be to consider M non-interacting parallel chains of N double quantum wells. Essentially this corresponds to M wires in parallel, separated by an insulating material. Then, the voltage drop across each single wire will be the same as the voltage V applied to the system. Effectively, only I_0 in equation (5.6) will be scaled by M and ultimately absorbed into the prefactor itself. So

then, γ represents the averaged inverse number of tunneling events of M parallel wires. For our diamond samples the bottom surface is as smooth as the atomically polished surface of the growth substrate. On the other hand, the top surface can be very rough exhibiting a surface roughness of up to 90 nm [39]. Quite considerable when the thickness of the flake is just $\sim$ 600 nm thick. With a such a big surface roughness the path of least resistance between bottom and top surface will be at the valleys of the rough surface landscape on the top side. The length of the parallel wires is minimized, effectively reducing the deviations of γ of each single parallel wire.

A wide range of publications has used a slightly modified version of equation (5.6), where $2\alpha - 1$ is replaced with $\alpha + 1$. This originates from the observation of a universal scaling behavior in Luttinger liquids in one-dimensional carbon nanotubes [86], which was later used for quasi-one-dimensional bundles of nanofibers [87, 88] as well as two-dimensional films of polymers, claiming to observe Luttinger liquid behavior [89, 90], nuclear mediated polaron hopping [91], or variable range hopping [92] to name a few. In any case, the equation of the universal scaling behavior is identical for all the above situations leading to a problematic ambiguity when trying to distinguish between underlying physical models. We will stick to the form of $T^{2\alpha-1}$, since it is not clear how the factor of $\alpha + 1$ is obtained. However, both expressions for the universal scaling behavior are equivalent, with the only difference that α will vary by a transformation factor.

5.4 Universal Scaling of Lowly Doped Samples below 100K

We have performed measurements of lowly (266ppm) and highly (10k ppm) boron-doped diamond-on-graphene heterostructures and single flakes over a wide range of voltages and temperatures. In this section, we will present our results for the lowly doped samples, which exhibit highly non-linear characteristics at low temperatures. Current-voltage measurements of a single diamond flake from 4K to 100K are presented in the left plot of figure 5.3. The right plot shows the collapse of our measurements onto a single curve of scaled current $I/T^{2\alpha-1}$ versus eV/k_BT, demonstrating universal scaling behavior of expression (5.6). Three different regimes of the universal scaling behavior can be identified: Ohmic regime (O), transition region (T), and power law regime (P). They are separated by dashed line. Regimes defined by dashed lines in the bottom (top) part correspond to our experimental data (best fit), respectively. The best fit of formula (5.6) is shown in black. Three parameters I_0, α, γ were used for fitting and the obtained values are $I_0 = 5 \cdot 10^{-11}$ nA/K$^{6.2}$, $\alpha = 3.6$, and $\gamma = 0.0012$. One identifies, that the transition region is extended in our measurements, compared to what is expected from the theoretical model of the best fit. The onset of the transition regime can be determined from a change in slope compared to the Ohmic regime. In the Ohmic regime, the slope of a log-log plot $I/T^{2\alpha-1}$ vs eV/k_BT should be identical to one, while it is bigger than one in the transition regime.

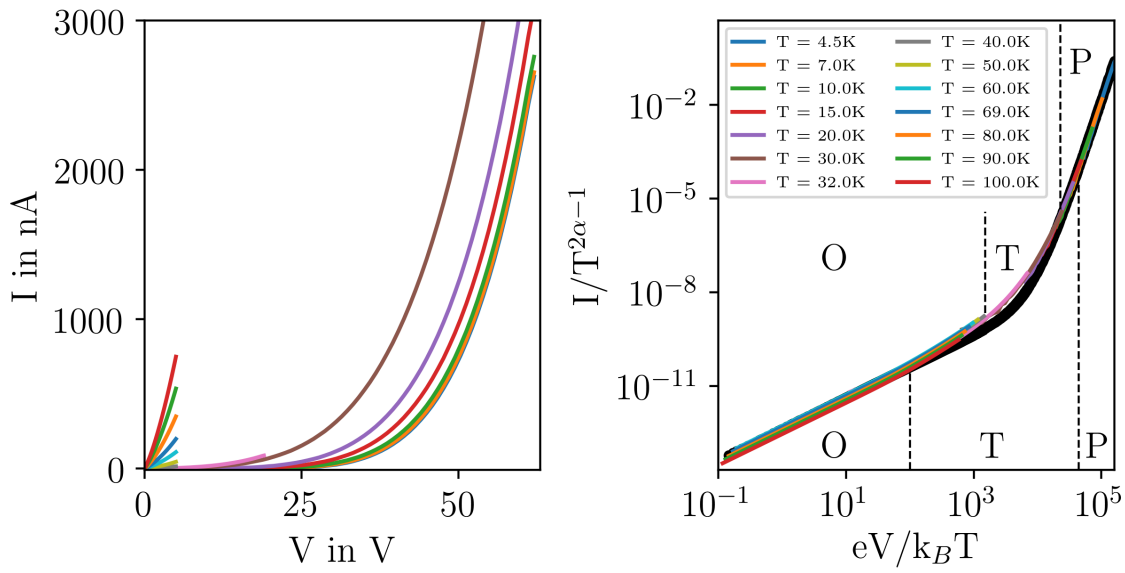

Figure 5.3: Universal scaling behavior of lowly boron-doped diamond. Left: Current-voltage measurements of a lowly boron-doped (266ppm) diamond polycrystalline flake from 4K to 100K. Temperature color coding can be found in the right plot. Right: Collapse of current-voltage characteristics onto a single curve demonstrating universal scaling behavior for $\alpha = 3.6$ between 4K and 100K. Ohmic (O), transition (T), and power law regime (P) of the universal scaling behavior are separated through dashed lines, for experimental data (bottom dashes) and best fit (top dashes).

As discussed in section 5.3, γ yields the average inverse number of tunneling events for a single chain of $1/\gamma$ quantum wells, and hence allows us to easily obtain the average tunneling distance $l_T = d\gamma$ with the separation of the metallic electrodes d. This is quite significant, since now we have enough knowledge about the double quantum well to make at least an order of magnitude estimation for the frequency of small oscillation ω_0 at the potential wells and ω_B at the barrier top! For this specific sample we obtain $l_T = 12.3$ nm$= 2x_0$. The minimum tunneling time to transverse the classicaly forbidden barrier is estimated to be $t = (12.3\,\mathrm{nm}\cdot\sqrt{\epsilon_r})/c = 9.8\cdot10^{-17}s$, where c is the speed of light and $\epsilon_r = 5.7$ the dielectric constant of diamond. A model for the effective activation energy of doped semiconductors as a function of the doping level was suggested by Pearson and Bardeen

[93]

$$E_B^{eff} = E_B - \beta n_A^{1/3} = 0.37\,\mathrm{eV} - 6.7 \cdot 10^{-8}\,\mathrm{eV \cdot cm} \times (8.77 \cdot 10^{17}\,\mathrm{cm}^{-3})^{1/3} = 315.5\,\mathrm{meV} \quad (5.7)$$

where $\beta = 6.7 \cdot 10^{-8}$ eV·cm is a materials dependent constant [94], E_B^{eff} is the effective barrier height to ionize the boron dopant, and n_A is the concentration of the dopant. We set the the potential height V_0 in figure 5.2 equal to E_B^{eff} and find for

$$\omega_0 = \left(\frac{V(x)''|_{x=-x_0}}{M} \right)^{1/2} = \left(\frac{8V_0}{Mx_0^2} \right)^{1/2} = 1.3 \cdot 10^{14} \frac{1}{\mathrm{s}} \quad (5.8)$$

$$\omega_B = \left(\frac{-V(x)''|_{x=0}}{M} \right)^{1/2} = \left(\frac{4V_0}{Mx_0^2} \right)^{1/2} = 9.0 \cdot 10^{13} \frac{1}{\mathrm{s}} \quad (5.9)$$

where $M = 0.7m_e$ is the hole mass in terms of the electron mass m_e, and $x_0 = 6.15$ nm. The results for ω_0 and ω_B are on the time scale of non-equilibrium lattice relaxations ($10^{-12}\frac{1}{s} - 10^{-14}\frac{1}{s}$) and thus correlation with the environment in terms of memory friction might come into play [95]. In order to compare the ground state E_0 and the first excited state E_1 with the thermal energy and the electric field energy, we assume that the energy levels in the quantum well can be approximated to zeroth order by a simple quantum mechanic harmonic oscillator. Strictly speaking this is not correct, since in a quartic potential the energy levels will have intricate correction factors, which must be computed numerically, but it suffices for the purpose of a comparison. We obtain $E_0 \approx \hbar\omega_0/2 = 41.8$ meV, $E_1 \approx 3\hbar\omega_0/2 = 125.5$ meV, $E_2 \approx 5\hbar\omega_0/2 = 209.2$ meV, and $E_3 \approx 7\hbar\omega_0/2 = 292.9$ meV. A total of four energy eigenstates fit into each of the potential wells. The thermal energy $k_BT = 25.7$ meV at room temperature and the potential drop across a double well at the highest voltage applied of 60 V at 4 K gives $\gamma eV \approx 72.0$ meV. The ground state energy E_0 stays much bigger than k_BT at least up to room temperature ($E_0 >> k_BT$), and the

effective barrier height $E_B^{eff} = V_0 >> E_0$. Even though the applied potential γeV reaches the ground state energy level, it does not come to a level crossing of the ground state energy in left potential well and the first excited state in the right well, even when the thermal energy at low temperatures is included. Hence, all assumptions leading to a two-state system in the double quantum well hold. We conclude, that all underlying assumption of dissipative quantum tunneling in a double quantum well are met experimentally and that universal scaling is observed in lightly boron-doped diamond up to 100K.

5.5 Ohmic Regime of Dissipative Quantum Tunneling

Qualitatively, the Ohmic regime corresponds to $eV << k_BT$. Approximating what can be approximated reduces the universal scaling law (5.6) into a linear response regime

$$I \approx I_0 T^{2\alpha-1} \left(\frac{\gamma eV}{2k_BT} \right) \Gamma^2(\alpha) \tag{5.10}$$

where $\sinh(\gamma eV/2k_BT) \approx \gamma eV/2k_BT$ and $|\Gamma(\alpha + i\gamma eV/2\pi k_BT)|^2 \approx \Gamma^2(\alpha)$. Then, $I \approx V$ and the low bias conductance G becomes

$$G = \frac{I}{V} \approx I_0' T^{2\alpha-2} \tag{5.11}$$

where $I_0' = [\gamma e^2 \Delta^2 \Gamma^2(\alpha)/8k_B\omega_0\Gamma(2\alpha)](2\pi k_B/\hbar\omega_0)^{2\alpha-1}$. Now, the slope of a log-log plot of G versus T should yield $2\alpha - 2$. Figure 5.4 gives $\alpha = 3.55$ in close agreement with the expected value of $\alpha = 3.6$ from the universal scaling behavior in figure 5.3.

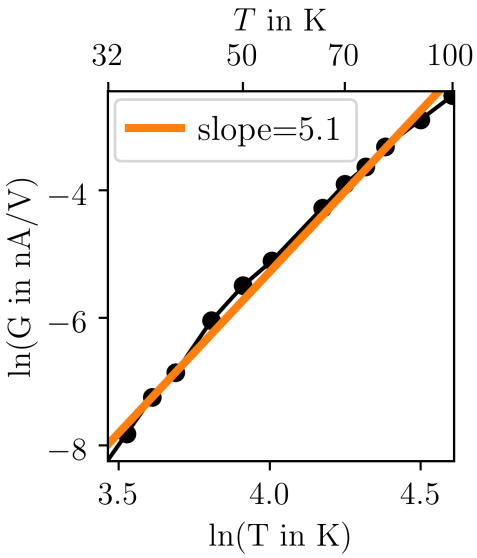

Figure 5.4: Log-log plot of low bias conductance vs temperature. $\alpha = (\text{slope} + 2)/2 = 3.55$ in agreement with the α from the universal scaling behavior. Top axis is included for better readability.

Data points for temperatures smaller than what is shown in the plot were below the noise level of the measurement setup.

5.6 Power Law Regime of Dissipative Quantum Tunneling

The power law regime ($eV >> k_B T$) turns out to be somewhat trickier than the Ohmic regime. The scientific literature extracts the dissipation strength α for strong damping ($\alpha > 1$) from the power law expression $I \approx V^{\alpha+1}$ [87, 88, 89, 90, 91, 92]. I will show that a $I \approx V^{\alpha+1}$ does not sufficiently describe the universal scaling behavior obtained from equation (5.5).

Let's assume that $I \propto V^{\alpha+1}$ appropriately expresses the universal scaling law. Then, a log-log plot of I vs V should give a straight line and its slope should be equal to $\alpha + 1$. Figure 5.5 (left plot) shows a computer-generated set of current-voltage data from

formula (5.5) on a log-log scale for different values of α. An exemplary fit is included for $\alpha = 9$ which differs from the fitted slope = 17.0.

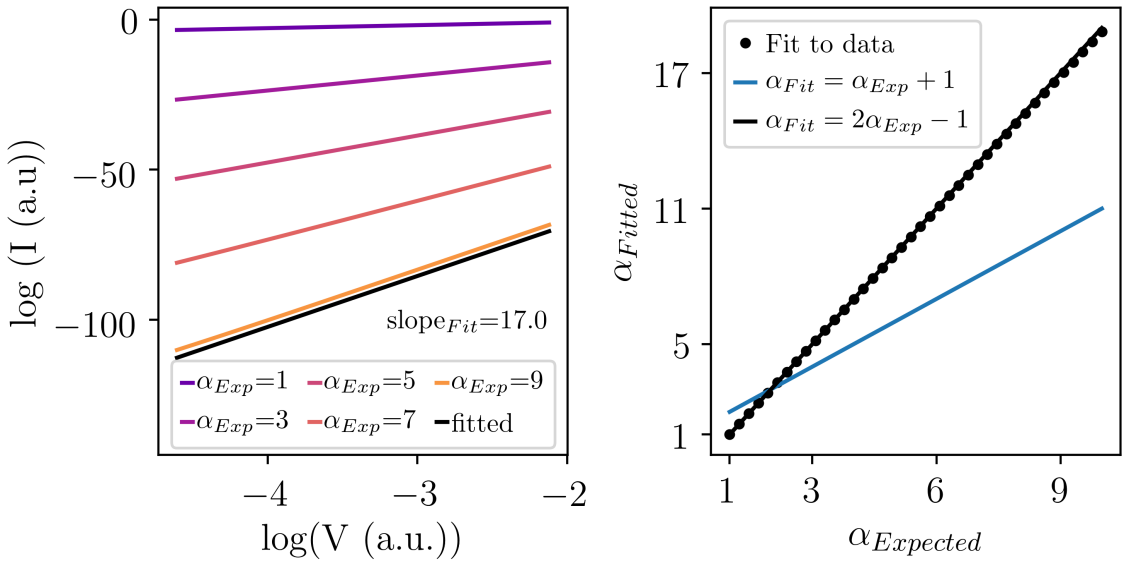

Figure 5.5: Computer generated data of dissipative quantum tunneling. Left: Current-voltage traces for 5 different values of α. For $\alpha = 9$, a fitted slope is included and equals 17.0. Right: Fitted versus expected values of α. $I \propto V^{2\alpha-1}$ describes the fitted slopes the best.

Evidently, the power law regime is not described by $I \propto V^{\alpha+1}$. In the right plot of figure 5.5, a set of fitted slopes is plotted for α ranging from 1 to 10. One observes that $I \propto V^{2\alpha-1}$ describes the fitted slopes the best.

Let's attempt to justify this more rigorously. An expansion of the universal scaling behavior $I = I_0 T^{2\alpha-1} \sinh(\pi x)|\Gamma(\alpha+ix)|^2$ is required in the power law regime, where $x = \gamma eV/2\pi k_B T$ is the ratio of electric field energy per hop over the thermal energy. An algebraic representation of the Gamma function to high accuracy for real and complex arguments is given by [96]

$$\Gamma(z) \approx \sqrt{\frac{2\pi}{z}} \left(\frac{z}{e}\right)^z \left(z \sinh\left(\frac{1}{z}\right) + \frac{1}{810z^6}\right)^{z/2} \tag{5.12}$$

where $z = \alpha + ix$ and e is Euler's constant. One can call this an extended version of Stirling's formula. In the power law regime $1/860z^6$ can be neglected. Complex exponentiation of a complex number can be simplified by the identity

$$(a+ib)^{X+iY}(a-ib)^{X-iY} = (a^2+b^2)^X \, \mathrm{e}^{-2Y\theta} \tag{5.13}$$

where $\theta = \arctan(b/a)$. We will make use of the complex property of the gamma function

$$|\Gamma(z)|^2 = \Gamma(z)\overline{\Gamma(z)} = \Gamma(z)\Gamma(\overline{z}) = A \cdot B \cdot C \tag{5.14}$$

and separate the result for pedagogical reasons into three terms A, B, and C. After inserting (5.12) into (5.14) and applying complex exponentiation we obtain

$$A = \sqrt{\frac{2\pi}{z}}\left(\frac{z}{\mathrm{e}}\right)^z \sqrt{\frac{2\pi}{\overline{z}}}\left(\frac{\overline{z}}{\mathrm{e}}\right)^{\overline{z}} = \frac{2\pi}{\mathrm{e}^{2\alpha}}(\alpha^2+x^2)^{\alpha-1/2}\,\mathrm{e}^{-2x\arctan(x/\alpha)} \tag{5.15}$$

$$B = z^{z/2}\overline{z}^{\overline{z}/2} = (\alpha^2+x^2)^{\alpha/2}\,\mathrm{e}^{-x\arctan(x/\alpha)} \tag{5.16}$$

$$C = \sinh^{z/2}\left(\frac{1}{z}\right)\sinh^{\overline{z}/2}\left(\frac{1}{\overline{z}}\right) = (\alpha^2+x^2)^{-\alpha/2}\,\mathrm{e}^{+x\arctan(x/\alpha)} \tag{5.17}$$

As it turns out, B and C cancel each other, and could have been omitted from the beginning, reducing expression (5.12) to the well-known Stirling formula. Terms B and C become more relevant below the power law regime. Then, the universal scaling law reads

$$I = \frac{2\pi}{\mathrm{e}^{2\alpha}} I_0 T^{2\alpha-1} \sinh(\pi x)\,\mathrm{e}^{-2x\arctan(x/\alpha)}(\alpha^2+x^2)^{\alpha-1/2}. \tag{5.18}$$

For large x (power law regime), $\arctan(x/\alpha) \to \pi/2$ and therefore $\sinh(\pi x)\,\mathrm{e}^{-2x\pi/2} \to 1/2$. It is noted that only a slight deviation of the ratio of the arguments of $\sinh(\pi x)$ and $\mathrm{e}^{-\pi x}$ from $\frac{-\pi x}{\pi x} = -1$ leads to either exponential decay or exponential potentiation of $\sinh(\pi x)\,\mathrm{e}^{-\pi x}$. A very narrow line for the emergence of a power law behavior. In the power

law regime the universal scaling law simplifies to

$$I = \frac{\pi}{e^{2\alpha}} I_0 T^{2\alpha-1} (\alpha^2 + x^2)^{\alpha-1/2} \propto V^{2\alpha-1} \tag{5.19}$$

where $x = \gamma eV/2\pi k_B T$, α represents the dimensionless dissipation constant, and γ the inverse number of tunneling events. To leading order $I \propto V^{2\alpha-1}$, in agreement with our analysis based on the computer generated data set. For $T = 0$ this behaviour has explicitly been stated by [97] (therein, formula 7.20). However, the finite temperature enhancement in [97] (therein, formula 7.19) is proportional to T^2, which is in contrast to our result in equation (5.19) where it varies as $T^{2\alpha-1}$. This discrepancy remains unresolved, since it is not clear to me what approximations the authors used to arrived at their formula (7.19). In summary, the voltage dependence in the power law regime was derived in this section.

5.7 Current-Voltage Data in the Power Law Regime

Next, we compare our experimentally extracted α from the power law regime to the α from the Ohmic regime and the universal scaling behavior plot. Figure 5.6 shows a log-log plot of current-voltage data taken at 4.5 K. A slope of 6.4 corresponds to $\alpha = (6.4 + 1)/2 = 3.7$, in good agreement with 3.55 (Ohmic) and 3.6 (universal scaling). For this specific sample, the current was below the noise level for 17 V of applied bias.

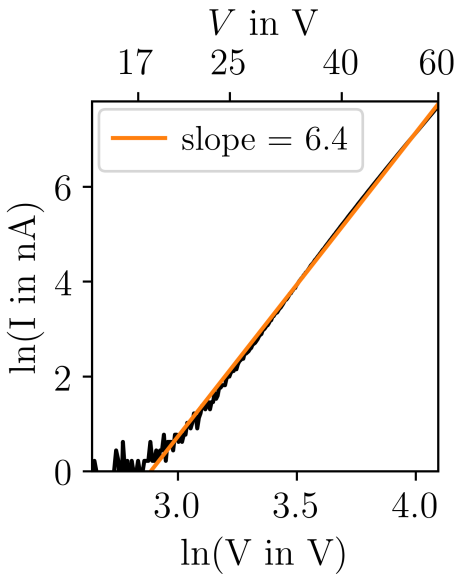

Figure 5.6: Log-log plot of current-voltage characteristics taken at 4.5K. Extracted $\alpha = (\text{slope}+1)/2 = (6.4+1)/2 = 3.7$. Top axis is included for better readability.

5.8 Current-Voltage Characteristics of Lowly Doped Samples above 100 K

So far we have looked at current-voltage characteristics up to 100 K. Above 100 K, we observe deviations from the universal scaling behavior in the Ohmic regime as well as a small part of the transition region. Temperatures from 100 K to 300 K are now included in the universal scaling plot and can be found in the right part of figure 5.7. The curves in the Ohmic regime have a parallel offset towards lower $I/T^{2\alpha-1}$ values above 100 K.

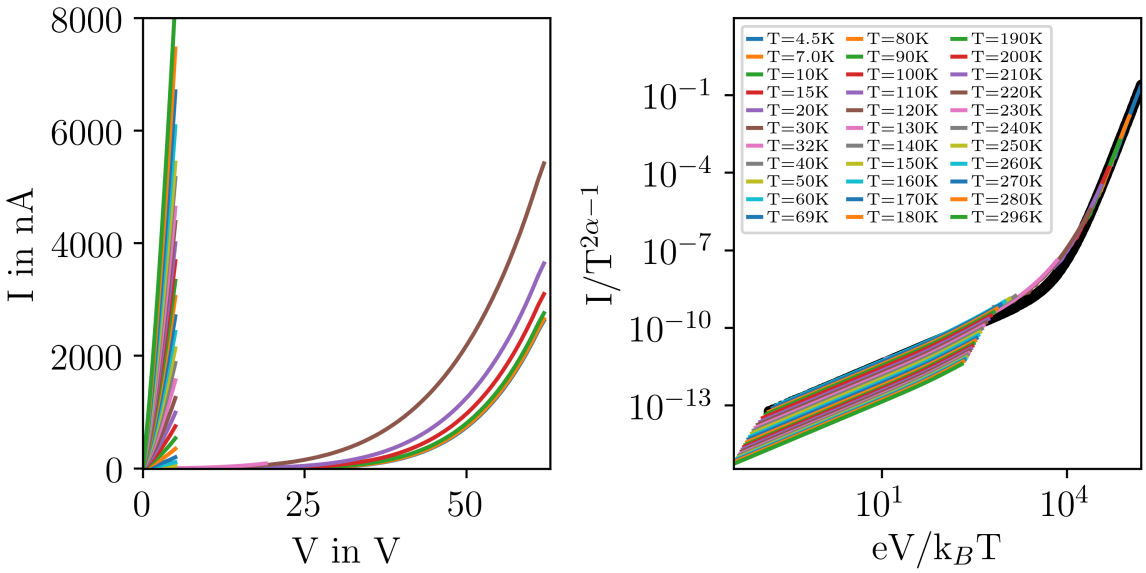

Figure 5.7: Universal scaling behavior of current-voltage characteristics of lowly boron-doped diamond. Left: Current voltage characteristics. Right: Universal scaling behavior with data above 100K shows a constant offset towards lower $I/T^{2\alpha-1}$ values.

In order to investigate this downshift along the y-coordinate we want to get an intuition about what happens when the scaling parameters α, γ and ω_0 are varied. Therefore a set of computer generated universal scaling curves is plotted in figure 5.8, for different conditions of α, γ and ω_0, where T ranges from 4 K to 300 K and V ranges from 1 mV to 60 V. Each of them has a unique effect on the $I/T^{2\alpha-1}$ vs $\gamma eV/k_BT$ plane. Changing γ, while holding α and ω_0 fixed, shifts the curve horizontally along the x-axis, as you can see in the left plot. Increasing the inverse number of tunneling events γ, results in a shift to the left. Changing α (middle and right plot), while holding γ and ω fixed, has a combined effect of shifting the curve vertically along the y-axis and bending the slope in the power law regime towards higher or lower values. It is necessary to distinguish the cases of $2\pi k_B/\hbar\omega_0 > C$ and $2\pi k_B/\hbar\omega_0 < C$, where C is a critical numerical value on the order of 1.5/Kelvin, as you can see in the middle and the right plot, respectively. Upon increasing α in the middle plot, a

shift of the curve in the ohmic regime towards lower $I/T^{2\alpha-1}$ values occurs. Physically, this corresponds to decreasing the tunneling rate Γ, as anticipated when increasing the coupling to the environment α, tunneling becomes less frequent. In the power law regime the change in the slope increases in agreement with formula (5.19). The bigger α, the bigger the slope will be. Now this is true for both cases of $2\pi k_B/\hbar\omega_0 > C$ and $2\pi k_B/\hbar\omega_0 < C$. However, in the Ohmic regime the effect of increasing α reverses when $2\pi k_B/\hbar\omega_0 < 1$, as seen in the right plot. The tunneling rate increases when the the coupling to the environment increases. It is not immediately clear whether this constitutes a physical situation or whether such a case is physically not realizable. Based on the measurements shown in figure 5.7, we cannot conclude if γ or α is changing, since the data in power law regime above 100K is not available. Furthermore, it is hard to reach this limit experimentally, since very high applied voltages tend to break the device. Instead, we will argue now that the deviations from the universal scaling above 100K arise from a transition from a pure quantum mechanical transport regime to a classical transport regime with quantum corrections.

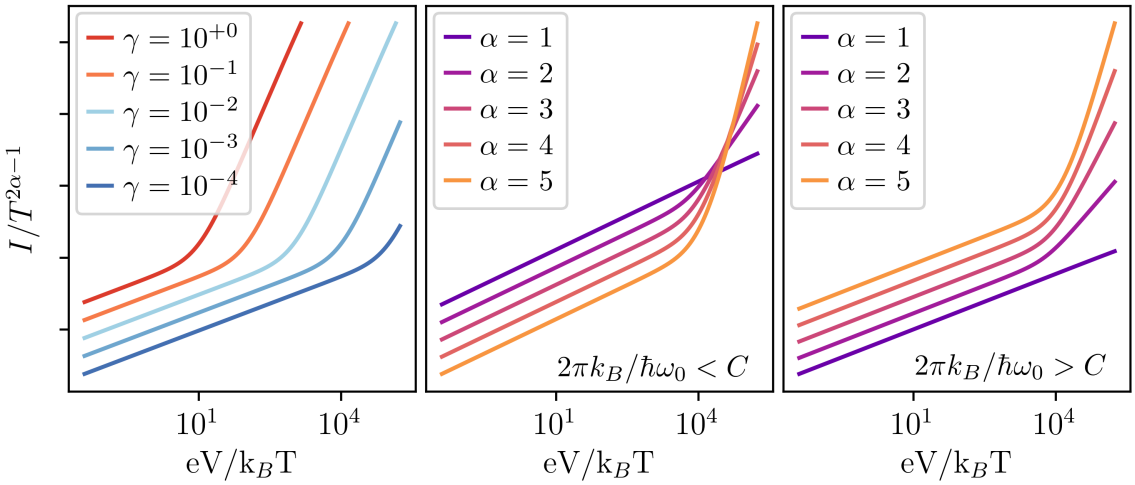

Figure 5.8: Universal scaling behavior for different alpha and gamma.

We will close this section with an estimate of T_0, the transition temperature at

which the system changes from quantum (section 5.9.4) to quasi-classical regime (section 5.9.2). Without dissipation, T_0 can be obtained from the parabolic curvature ω_B at the barrier top $T_0 \approx \frac{\hbar\omega_B}{2\pi k_B}$ and we obtain a value of 109 ± 10 K with ω_B from relation (5.9). As will be discussed in section 5.9.3, the effect of dissipation is to lower the transition temperature T_0. We assume frequency-independent dissipation $\hat{\gamma}(\omega) = \gamma$ in formula (5.27), and the resulting dissipation renormalized frequency-independent crossover temperature $T_0 = 95 \pm 10$ K. The transition temperature is in good agreement with the onset of deviations from universal scaling behavior starting around 100 K. The value of the classical damping factor γ (which is a different γ than the inverse number of tunneling events obtained from fitting procedures) is obtained from the dimensionless dissipation constant $\alpha = 3.6$ by [85]

$$\gamma = \frac{2\pi\hbar\alpha}{M(2x_0)^2} = 3.6 \cdot 10^{13} \frac{1}{\mathrm{s}}. \tag{5.20}$$

where $2x_0 = 12.3$ nm and $M = 0.7m_e$ is the hole mass in terms of the electron mass. Our results suggest that we have observed a smooth crossover from purely quantum mechanical behavior to a semi-classical regime. The experimentally observed stretching of the transition region into the Ohmic regime can potentially be understood in terms of memory friction effects since the time scale for dissipation γ and small frequencies ω_0 are on the same order of magnitude.

5.9 The Classical to Quantum Transition

In this section we investigate the transition from classical hopping transport to tunneling transport in the quantum regime with the inclusion of dissipation in both regimes. An important assumption in this chapter is that a metastable localized state decays into

a continuum of states and not into another localized state. Up to this point, I was not able to find the analysis, presented in this section, for the particular case of a double quantum well, with exception to the transition temperature which holds independent of the nature of the final state. Starting at low temperatures, quantum tunneling prevails up to a crossover temperature T_0, where the system transitions into a classical regime with quantum corrections. Those quantum corrections sustain for quite a large temperature range before thermally activated nearest neighbour hopping sets on, as seen in figure 5.9 [98].

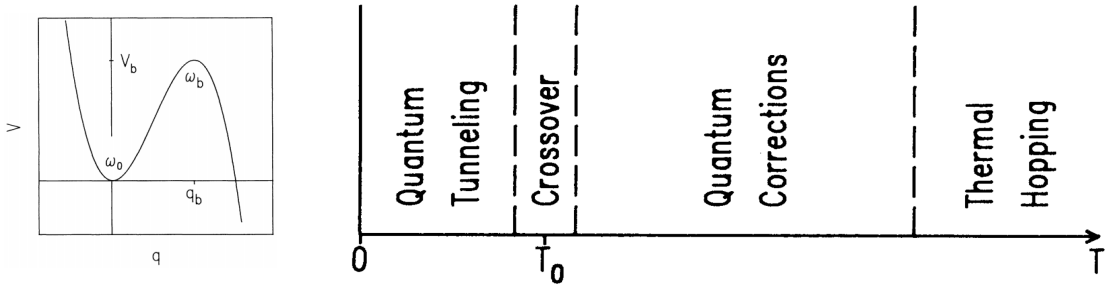

Figure 5.9: Different transport regimes for a charge carrier escaping from a localized state to a continuum of states. Left: Metastable quantum well discussed in this chapter. A localized charge carrier in the left minimum escapes into a continuum of states to the right. Right: Different transport regimes to escape from a metasable potential well versus temperature. Reprinted with permission from [98].

5.9.1 The Classical Regime

It is well-established in disordered materials, that electronic conduction is dominated by thermally activated transport of the form of an Arrhenius factor $\exp(-E_B/k_BT)$ at high temperatures, see chapter 4.1. Arrhenius [99] was the first to suggest the form $\exp(-E_B/k_BT)$ for the temperature dependence of reaction rates in 1889, and ever since it arose in many different phenomena and fields of science. In Kramer's transition rate theory [100], a particle of mass M placed in a metstable potential well with small oscillation

frequencies ω_0, escapes into a continuum of states with

$$\Gamma = \Gamma_{cl}\, \mathrm{e}^{-E_B/k_BT} = \frac{\omega_0}{2\pi}\frac{\omega_R}{\omega_B}\, \mathrm{e}^{-E_B/k_BT} \tag{5.21}$$

where E_B corresponds to the barrier height of the potential well, Γ_{cl} is the classical attempt frequency to overcome the potential barrier, ω_0 is the frequency of small oscillations in the metastable state, ω_B is the frequency defined by the parabolic curvature at the barrier top, and $\omega_R = \omega_B\{[1 + (\gamma/\omega_B)^2]^{1/2} - \gamma/\omega_B\}$ is the renormalized frequency of small oscillations of an inverted barrier top including the environmental damping factor γ [101]. The particle collects enough energy from the environment and its thermodynamic fluctuations to overcome the potential barrier in a classical manner. For small but finite damping γ, the expression Γ_{cl} reduces to the standard outcome of transition state theory $\Gamma_{cl} = \omega_0/2\pi$ [102]. Kramers found that, if the damping does not stay finite and $\gamma \to 0$, then $\Gamma_{cl} \propto \gamma$ and the escape rate vanishes, because the system decouples from the environment. The heat bath cannot maintain a thermal equilibrium with the metastable well [100]. On the other hand, if $\gamma \to \infty$ the attempt frequency $\Gamma_{cl} \propto \omega_0/\gamma$ and goes to zero, hindering any motion of the particle by an opposing frictional force. We conclude that at high temperatures, we deal with a purely classical phenomenon with corresponding analogies to a damped harmonic oscillator.

5.9.2 The Quasi-Classical Regime: Classical+Quantum Corrections

Next, let's consider the region of quantum corrections. As temperature is lowered, the system stays in a classical regime but quantum corrections become important. We term this region quasi-classical regime. Classically, a particle collects enough energy from

environmental thermodynamic fluctuations to hop over the barrier top. In analogy, quantum mechnically, the escape rate of the particle from the potential well can be enhanced by quantum fluctuation of the barrier top. In both cases the effective barrier height is lowered. In order to incorporate quantum corrections into the escape rate a functional path integral approach is chosen. It allows to introduce the environment and the interaction with the environment through a non-local term S_{ex} in the effective action S. In this quantum field theoretical framework the imaginary part of the free energy F, which is a function of the effective action S, gives the transition rate $\Gamma = -(2/\hbar)(T_0/T)\,\mathrm{Im}(F)$ [103], valid for $T > T_0$ with T_0 the transition temperature between quasi-classical and quantum regime. A detailed derivation of the resulting transition rate Γ can be found in [101, 98] for temperatures above T_0, and it reads

$$\begin{aligned}\Gamma &= \Gamma_{cl} f_{QC}\, \mathrm{e}^{-E_B/k_BT} \\ &= \left(\frac{\omega_0\omega_R}{2\pi\omega_B}\right)\left(\prod_{n=1}^{\infty}\frac{\omega_n^2+\omega_0^2+\omega_n\hat{\gamma}(\omega_n)}{\omega_n^2-\omega_B^2+\omega_n\hat{\gamma}(\omega_n)}\right)\mathrm{e}^{-E_B/k_BT} \\ &\overset{\hat{\gamma}(\omega_n)=\gamma}{=} \left(\frac{\omega_0\omega_R}{2\pi\omega_B}\right)\left(\frac{\Gamma_G(1-\lambda_B^+/\nu)\Gamma_G(1-\lambda_B^-/\nu)}{\Gamma_G(1-\lambda_0^+/\nu)\Gamma_G(1-\lambda_0^-/\nu)}\right)\mathrm{e}^{-E_B/k_BT}\end{aligned} \tag{5.22}$$

where $\omega_n = 2\pi n k_B T/\hbar$ are the Matsubara frequencies, f_{QC} the form factor that accounts for quantum corrections, Γ_G is the Gamma function, and $\nu = \omega_1 = 2\pi k_B T/\hbar$. The quantum correction form factor f_{QC} can be simplified in the last line of (5.22) in terms of Gamma functions Γ_G if frequency-independent damping $\hat{\gamma}(\omega_n) = \gamma$ is assumed [98] where

$$\lambda_B^{\pm} = -\frac{\gamma}{2} \pm \left(\frac{\gamma^2}{4}+\omega_B^2\right)^{1/2}, \quad \lambda_0^{\pm} = -\frac{\gamma}{2} \pm \left(\frac{\gamma^2}{4}-\omega_0^2\right)^{1/2} \tag{5.23}$$

The last term in formula (5.22) is valid for the whole temperature range $T > T_0$ and the quantum correction f_{QC} tends to one for $k_BT >> \hbar\omega_0$ which recovers the classical

limit. The latter statement is only true for extremely high temperatures for boron-doped diamond, since $E_{B,max} \approx 0.37$ eV and the activation temperature $T_{A,max} \approx 4300$ K. The quasi-classical regime easily extends beyond room temperature for boron-doped diamond samples. Quantum corrections f_{QC} are contributing considerably more than thermally activated nearest neighbour hopping over the barrier top at room temperature. A variation of approximations for f_{QC} in the quasi-classical regime is summarized in table 5.1 for different damping strengths and temperature ranges closer and far away from T_0. Particular care needs to be taken for the case of weak damping $\gamma << \omega_0, \omega_B$ because non-equilibrium effects influence the transition rate significantly.

<table>
<tr><th></th><th>$T_0 << T << 4\alpha_B^2 T_0$</th><th>$T >> 4\alpha_B^2 T_0$</th></tr>
<tr><td rowspan="2">$\gamma >> \omega_0, \omega_B$</td><td colspan="2">$f_{QC} = \mathrm{e}^{\left[\frac{T_0}{T}\left(1+\frac{\omega_0^2}{\omega_B^2}\right)\left(\Psi\left(1+4\alpha_B\frac{T_0}{T}\right)-\Psi(1)\right)\right]}$</td></tr>
<tr><td>$f_{QC} \approx \left(\frac{4\alpha_B^2 T_0}{T}\right)^{\left(1+\omega_0^2/\omega_B^2\right)(T_0/T)}$</td><td>$f_{QC} \approx \mathrm{e}^{\frac{\hbar}{24}\frac{\omega_0^2+\omega_B^2}{(k_B T)^2}} + \mathcal{O}^4(T,\gamma)$</td></tr>
<tr><td>$\gamma \sim \omega_0, \omega_B$</td><td>$f_{QC} = \frac{\Gamma_G(1-\lambda_B^+/\nu)\Gamma_G(1-\lambda_B^-/\nu)}{\Gamma_G(1-\lambda_0^+/\nu)\Gamma_G(1-\lambda_0^-/\nu)}$</td><td>$f_{QC} \approx \mathrm{e}^{\frac{\hbar}{24}\frac{\omega_0^2+\omega_B^2}{(k_B T)^2}} + \mathcal{O}^4(T,\gamma)$</td></tr>
<tr><td>$\gamma \sim \omega_0, \omega_B$</td><td colspan="2">$f_{QC} = \frac{\omega_B \sinh(\pi\omega_0/\nu)}{\omega_0 \sin(\pi\omega_B/\nu)}\,\mathrm{e}^{\left(\alpha_B\frac{\omega_B}{\nu}\left(\Psi(x_B^+)+\Psi(x_B^-)-\Psi(x_0^+)-\Psi(x_0^-)+\mathcal{O}(\alpha^2)\right)\right.}$</td></tr>
</table>

Table 5.1: Approximations of the quantum correction form factor f_{QC} for different temperature scales, strong ($\gamma >> \omega_0, \omega_B$), moderate ($\gamma \sim \omega_0, \omega_B$) and weak ($\gamma << \omega_0, \omega_B$) damping stengths. $\alpha_B = \gamma/2\omega_B$, $\nu = 2\pi k_B T/\hbar$, Γ_G is the complex Gamma function, Ψ is the Digamma function with $x_B^{\pm} = 1 \pm \frac{\omega_B}{\nu}$, $x_0^{\pm} = 1 \pm i\frac{\omega_B}{\nu}$.

Last but not least, let's quantify the effect of quantum fluctucation on the barrier height E_B in the region of $T >> 4\alpha_B^2 T_0$ and moderate to strong damping. The renormalized

barrier height as a function of temperature reads [104]

$$E_B^{'} = E_B - \frac{\hbar^2}{24}\frac{\omega_0^2 + \omega_B^2}{k_B T} + \mathcal{O}^4(T, \gamma)\,. \tag{5.24}$$

5.9.3 The Transition Temperature T_0

In the limit of $T = T_0$ the denominator of formula (5.22) diverges, indicating a breakdown of the validity of transport in the quasiclassical regime. Larkin and Ovchinnikov [105] argued that a second-order phase transition from classical to quantum decay occurs at T_0, which should be visible as an abrupt change of the transition rate Γ in its temperature dependence and hence experimentally visible from measured currents. In the same paper they show that quantum fluctuations wash out the second-order phase transition within a narrow temperature range around T_0 and make it continuous. Not suprising, as such an abrupt transition has not been reported in experimental studies yet. Phenomenologically, at $T = T_0$, the classical Arrhenius factor $\exp(-E_B/k_B T)$ is replaced by the quantum mechanical factor $\exp(-S/\hbar)$ [80] with the effective action S such that at $T = T_0$ the transition rates match smoothly

$$\Gamma(T = T_0) = A_{CL}\, \mathrm{e}^{-E_B/k_B T_0} \quad \overset{T=T_0}{=} \quad A_{QM}\, \mathrm{e}^{-S/\hbar} = \Gamma(T = T_0) \tag{5.25}$$

where A_{CL} and A_{QM} are prefactors for the classical and quantum regime, respectively.

This brings us to the definition of T_0 originating as a solution of the determinant D_B, a second-order variation operator

$$D_B = \prod_{n=-\infty}^{+\infty} \lambda_n = \prod_{n=-\infty}^{+\infty} \omega_n^2 - \omega_B^2 + \omega_n \hat{\gamma}(\omega_n) \tag{5.26}$$

where the first eigenvalue to change signs is λ_1 and hence [101, 106, 105, 104]

$$\begin{aligned} T_0 &= \frac{\hbar}{2\pi k_B}\omega_R \\ &= \frac{\hbar}{2\pi k_B}\left(\left(\omega_B^2 + \frac{\hat{\gamma}(\omega)^2}{4}\right)^{1/2} - \frac{\hat{\gamma}(\omega)}{2}\right) \end{aligned} \tag{5.27}$$

where ω_R is the dissipation renormalized frequency of small oscillations of an inverted barrier top including the environmental classical damping factor γ, similar to what we have seen above in the classical regime. This yields the **dissipation renormalized frequency-dependent crossover temperature** T_0, which simplifies if frequency independent dissipation $\hat{\gamma}(\omega) = \gamma$ is assumed. Without dissipation, T_0 can simply be estimated from the parabolic curvature ω_B at the barrier top as $T_0 \approx \frac{\hbar\omega_B}{2\pi k_B}$. A pictorial physical interpretation of T_0 can be visualized like this: T_0 is the first temperature which admits an oscillation of the localized charge carrier along a periodic trajectory in the classically forbidden region below the dissipation-renormalized barrier height. This non-classical solution to the tunneling problem is referred to as a bounce, first named by Callan and Coleman [107]. Callan and Coleman were not the first to develop the tool box to tackle tunneling in this way, but Langer [108] did. He was the first to lay out a field theoretical approach to tunneling in a heat bath in a study of classical nucleation theory. In the view of this picture, the result of T_0 should hold independent of whether the potential well is a quantum well with decay into a continuum of states, like discussed in this section, or whether the potential well is a double quantum well, like observed in our experiment. Differentiating between the two types of quantum wells is important since they yield different temperature dependences in the quantum regime! Additionally, from our data it looks like the rate limiting transition process is the volume with its double quantum well structure and not the surface

where tunneling from a localized state into a continuum of states (the metallic electrode) possibly occurs. In summary, dissipation hinders the emergence of quantum mechanical effects by lowering the transition temperature T_0. The higher the dissipation γ the lower the temperatures required to reach the quantum regime.

As explained above, formula (5.22) diverges at the transition temperature $T = T_0$, and hence a perturbative consideration of the bounce action and fluctuation modes is required to obtain the transition rate Γ around T_0, which goes beyond the scope of this work. The interested reader is referred to [101, 105] for a detailed discussion of Γ in this very narrow temperature range at the transition point. For the purpose of completeness, only the end result will be presented

$$\Gamma = \frac{A}{2}\left(\frac{2\pi {S_B}''}{\hbar}\right)^{0.5} \operatorname{erfc}\left(\frac{\hbar {S_B}''}{2}\left(\frac{1}{k_B T} - \frac{1}{k_B T_0}\right)\right) \mathrm{e}^{-\frac{E_B}{k_B T} + \frac{\hbar {S_B}''}{2(k_B T)^2}} \tag{5.28}$$

where erfc is the Gaussian error function, ${S_B}'' = (1/2\pi)(Ma^2\nu/B)$, and A, a, B, ν can be looked up in reference [101].

5.9.4 The Quantum Regime

Lowering the temperature of a system below T_0 puts it into the quantum regime. An additional solution to the effective action S arises, the bounce solution. As mentioned above, the bounce solution is an oscillation of the localized charge carrier in the classically forbidden region of the potential well along a periodic trajectory, in other words quantum mechanical tunneling. Now, technically two separate conduction paths exist. Hopping over the renormalized barrier top (quasiclassical regime) and quantum mechanical tunneling through the classically forbidden barrier. The principle of least action will decide which

conduction path dominates. Evaluating the effective action of the two different conduction paths shows that the effective action due to the bounce solution is strictly lower than the effective action of the hopping solution [104]. Therefore, hopping transport can be disregarded and quantum mechanical tunneling is the leading conduction mechanism below T_0. Only in a narrow vicinity of the transition region T_0 will both conduction paths be contributing to charge transport. In the quantum regime the transition rate Γ takes the form $\Gamma = -(2/\hbar)\,\mathrm{Im}(F)$ [103], in slight contrast to what is used in the quasiclassical regime. Then,

$$\Gamma(T)/\Gamma(T=0) = \frac{\pi}{6}\gamma M\left[\frac{k^2}{\hbar^3}\left(\int_{-\infty}^{+\infty} q_B(\tau, T=0, \hat{\gamma})d\tau\right)^2\right]T^2 \tag{5.29}$$

will be proportinal to T^2 [106, 104], which was measured in macroscopic quantum tunneling experiments in biased Josephson junctions [109]. This result of $\Gamma \propto T^2$ stands in stark contrast to $\Gamma \propto T^{2\alpha-1}$ in equation (5.2). Both cases include dissipation in their derivation. The difference might stem from the fact that equation (5.2) is derived for a double quantum well, while equation (5.29) is derived for a metastable quantum well that decays into a continuum of states, see figure 5.2 and 5.9, respectively.

5.10 Theory of Dissipative Quantum Tunneling in a Double Quantum Well

In this section the theoretical background and the assumptions for dissipative quantum tunneling in the quantum regime ($T < T_0$) for strong dissipation are discussed. Unless otherwise stated, the results presented in this section are a comprehensive summary of the work published specifically in [85] and references therein. Although [85] was not the

first publication on dissipative tunneling in a double quantum well, it is very detailed and to the point. The original works published on a double quantum well appeared simultaneously in [81, 82].

A sketch of a biased double quantum well can be found in this chapter in figure 5.2. The outline of the task is as follows: A localized charge carrier is placed in the left well at $-x_0$ and the right well at $+x_0$ stays empty. Dissipation couples the charge carrier to the environment through a frictional force and only the strong damping regime is to be considered. The environment is modelled as a many-body system, namely a set of harmonic oscillators coupled to the charge carrier in the left well. Calculate the transition rate Γ for the charge carrier to decay away from the metastable state.

The assumptions of the biased double quantum well are $V >> E_0 >> |eV|$ and $E_0 >> k_B T$. The ground state energy of the localized particle is considerably higher than the energy provided by the electric field. It is also considerably lower than the potential barrier height such that thermally activated conduction over the barrier top can safely be neglected. Excitation of the ground state into its first excited state can be neglected as well. In order to calculate the transition rate, the framework of functional path integrals is chosen. A partition function Z will be setup to describe the system in terms of an analytically continued action S, also called Euclidean action S_E. The classical action S_{cl} can only describe classical hopping of a charge carrier over the potential well but not quantum mechanical tunneling through the classically forbidden region below the potential well. Thus, analytically continuing the path integral with its classical action S_{cl} into imaginary time τ by a wick rotation ($t \rightarrow i\tau$), flips the potential landscape upside down and in

such a way allows for a new solution to the Euclidean action S_E [110]. This new solution is the instanton, a pseudoparticle, which acts as the mediator for quantum mechanical tunneling. The mathematical framework is presented next where the upcoming derivations and formulas follow very closely reference [85]. Let's start with the transition rate Γ, the analytically continued free energy F, and the partition function Z

$$\Gamma = -\frac{2}{\hbar}\,\mathrm{Im}(F) \tag{5.30}$$

$$F = -(1/k_B T)\ln Z \tag{5.31}$$

$$Z = \int D(x(\tau))\,\mathrm{e}^{-S_E(x(\tau))/\hbar} \tag{5.32}$$

where τ is the imaginary time and $D(x(\tau))$ means to integrate over all classical field configurations. The paths to be summed by this integral require to be periodic, meaning $x(0) = x(\theta)$ with the period $\theta = (\hbar)/(k_B T)$. The Euclidean action S_E consists of two terms $S_E(x(\tau)) = S_0(x(\tau)) + S_D(x(\tau))$ where S_0 describes the dynamics of the system

$$S_0 = \int_{-\theta/2}^{+\theta/2} d\tau \left(\frac{M}{2}\dot{x}^2 + V(x) \right) \tag{5.33}$$

while S_D constitutes the dissipative term

$$S_D = \frac{1}{2}\int_{-\theta/2}^{+\theta/2} d\tau \int_{-\theta/2}^{+\theta/2} d\tau' k(\tau - \tau') x(\tau) x(\tau') \tag{5.34}$$

incorporating the environment as a non-local action. This is accomplished by the quantum mechanical dissipative kernel $k(\tau)$ which is related to the classical damping factor γ through

$$k(\tau) = \frac{M}{\theta} \sum_{n=-\infty}^{n=+\infty} |\,\omega_n\,|\,\hat{\gamma}(|\,\omega_n\,|)\,\mathrm{e}^{i\omega_n \tau} \tag{5.35}$$

with $\omega_n = 2\pi n/\theta$ the Matsubara frequencies and $\hat{\gamma}(\omega_n)$ the Laplace transform of $\gamma(t)$ which takes the form $\hat{\gamma}(\omega_n) = \int_0^\infty dt \exp(-\omega_n t)\gamma(t)$. Now, the Laplace transform of the classical

damping factor γ is related to the spectral density $J(\omega)$ of the heat bath in microscopic models by

$$\hat{\gamma}(\omega) = \frac{2}{\pi M} \int_0^\infty d\omega \frac{x}{\omega^2 + z^2} \frac{J(\omega)}{\omega}. \tag{5.36}$$

In general $J(\omega)$ will take on different shapes and simplifies to $J(\omega) = \gamma M \omega$ in the case of a Ohmic heat bath ($s = 1$) where the damping γ is frequency independent at low frequencies. For subohmic ($s < 1$) and superohmic ($s > 1$) heat baths $J(\omega)$ takes the form [97]

$$J(\omega) = A\omega^s \, \mathrm{e}^{-\omega/\omega_c} \tag{5.37}$$

with a normalization factor A and a cut-off term $\exp(-\omega/\omega_c)$ where the cut-off frequency ω_c is chosen above the Debye frequency of the system under consideration such that $\exp(-\omega/\omega_c)$ can be neglected for experimental frequencies. Equations (5.30-5.37) set up the stage for quantum mechanical tunneling with coupling to a heat bath consisting of a many-body set of harmonic oscillators.

The instanton solution can be obtained by setting the action $S_0 \stackrel{!}{=} 0$, separating and integrating variables dx and $d\tau$, which yields $x_I(\tau) = -q_0 \tanh(q_0(a/M)^{1/2}(\tau - \tau_0))$, where a is a normalization constant, $-q_0$ and $+q_0$ are the positions of the left and right well, respectively [110]. A graphical representation of the instanton solution is shown in the left part of figure 5.10. A single instanton solution is sufficient for the case of a subohmic and superohmic heat bath, but not for an Ohmic heat bath. Within an Ohmic heat bath, the Euclidean action S_E diverges for a single instanton, because the instanton reaches the right potential well only algebraically slowly in imaginary time τ. This is referred to as infrared divergence, which does not occur for a non-Ohmic heat bath. Luckily, it is possible to circumvent this divergence by pairing an instanton with an anti-instanton, to create a

composite pseudoparticle called the bounce. The anti-instanton can be understood in terms of an instanton travelling in reversed direction. Suppose a particle is placed in the left well and a single bounce occurs, then the particle will have tunneled to the right well, sojourned in the right well, and tunneled back to the left well. The driving force that holds together the composite pseudoparticle is the dissipative interaction with the environment. Furthermore, the composite pseudoparticle is said to have a dipolar structure, since instanton and anti-instanton can be viewed as particles of opposite charge. One underlying assumption of the bounce is that the flip time or tunneling time τ_0 is considerably smaller than the bounce time τ_1, as sketched in the left part of figure 5.10. Now it is possible to think about consecutive bounces, shown in the right part of figure 5.10, in terms of dipole-dipole interactions, which might influence the tunneling process. In principle, this could occur if the bounce separation ρ is on the same time scale as the bounce time τ_1

$$\tau_1 \approx \tau_S = \frac{\hbar}{\pi k_b T} \operatorname{arccot}\left(\frac{1}{\alpha}\frac{\gamma e V}{2\pi k_B T}\right) \sim \rho \approx \Gamma^{-1} \tag{5.38}$$

where ρ varies with the inverse tunneling rate, τ_S is the saddle point solution of the Euclidean action, and α is the dimensionless dissipation constant phenomenologically introduced in equation (5.2) and extracted from the universal scaling behavior. For most experiments it is safe to assume that the bounce time will be shorter than the bounce separation, but in general a limit could be reached where the opposite is true. All in all, dipole-dipole interactions of consecutive bounces are neglected, and we arrive at what is called the dilute bounce gas approximation. Under these assumptions, the one-bounce solution is the first leading correction to the partition function and consecutive bounces contribute negligibly small.

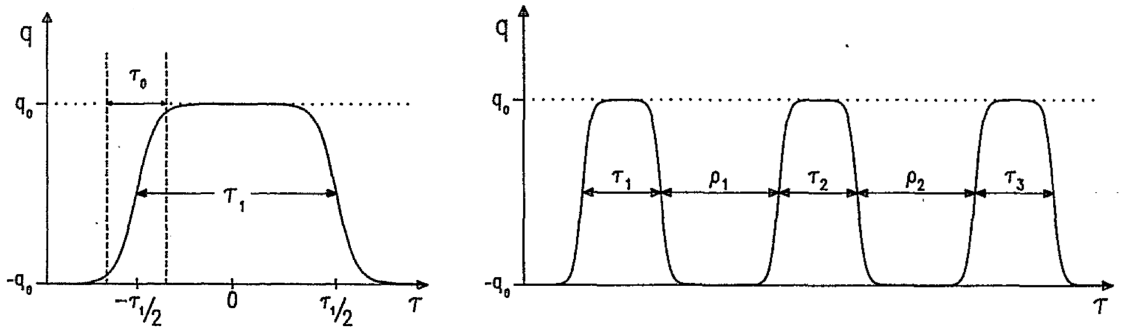

Figure 5.10: Graphical representation of the bounce solution in one dimension. Position of a charge carrier in the left ($x = -q_0$) or right ($x = +q_0$) quantum well versus imaginary time τ. Left: A bounce solution consisting of an instanton at $\tau = -\tau_1/2$ with width τ_0 and anti-instanton at $\tau = +\tau_1/2$. Right: N bounce solution with an average separation ρ from each other. Reprinted with permission from [85].

Cranking the mathematical machinery presented above provides different transition rates for Ohmic and non-Ohmic heat baths. Only the Ohmic heat bath shows a universal scaling behavior according to

$$\Gamma = \frac{\Delta^2}{4\omega_0}\frac{1}{\Gamma(2\alpha)}\left(\frac{2\pi k_B T}{\hbar\omega_0}\right)^{2\alpha-1}\cosh\left(\frac{eV}{2k_BT}\right)\left|\Gamma\left(\alpha + i\frac{eV}{2\pi k_B T}\right)\right|^2 \tag{5.39}$$

where $\Gamma = \Gamma_+ + \Gamma_-$ is the sum of the forward and backward transition rates, $\alpha = (2M\gamma x_0^2)/(\pi\hbar)$ is the dimensionless dissipation constant, and Δ is the tunneling matrix element

$$\Delta = 2\omega_0\left(\frac{M\omega_0 x_0^2}{2\pi\hbar}\,\mathrm{u}(\alpha_0)\,\mathrm{R}(\alpha_0)\right)^{1/2}\mathrm{e}^{-S^0_{B,1}/2\hbar} \tag{5.40}$$

where $\mathrm{u}(\alpha_0)$, $\mathrm{R}(\alpha_0)$ are constants depending on $\alpha_0 = \gamma/2\omega_0$, where α_0 is the dimensionless damping constant, and $S^0_{B,1}$ the action of the instanton and anti-instanton on their own without the interaction between them. $S^0_{B,1}$ reads

$$S^0_{B,1} = 2\hbar\left(\alpha C + \frac{2E_B}{\hbar\omega_0}D(\alpha_0) + \mathcal{O}(1/\omega_0^2\tau_S^2)\right) \tag{5.41}$$

where C and $D(\alpha_0)$ are constants defined in [85]. In order to obtain the current $I = e(\Gamma_+ - \Gamma_-)$ a minor manipulation is required. From the principle of detailed balance (5.3)

follows $\Gamma_+ \pm \Gamma_- = \Gamma_+(1 \pm \mathrm{e}^{-eV/k_BT})$ and hence

$$I = e\Gamma \frac{1 - \mathrm{e}^{-eV/k_BT}}{1 + \mathrm{e}^{-eV/k_BT}} = e\Gamma \tanh\left(\frac{eV}{2k_BT}\right) \tag{5.42}$$

The transition rates for a non-Ohmic heat bath have distinctively different forms and do not exhibit universal scaling behavior. Thus, it is possible to clearly distinguish an Ohmic from a non-Ohmic heat bath by collapse of current voltage characteristics onto a single curve. For purpose of completeness, the general form of the transition rate for non-Ohmic heat baths ($s \neq 1$) is provided

$$\text{Sub-Ohmic}(\, s < 1\,) : \Gamma \approx A_1 \left(\frac{1}{V}\right)^{(1+s)/2} \mathrm{e}^{(B_1/V)^{(1-s)/s}} \left(1 + C_1 \left(\frac{1}{V}\right)^{2/s} T^{1+s} + ...\right) \tag{5.43}$$

$$\text{Super-Ohmic}(\, s > 1\,) : \Gamma \approx A_2 V^{-2} J(\gamma eV/\hbar) = B_2 V^{s-2}\, \mathrm{e}^{-V/\omega_c} \tag{5.44}$$

where A_1, B_1, C_1, A_2, and B_2 can be found in [97] (see formulas 7.15a&b and 7.24 therein). The form of sub-Ohmic cases resembles a close similarity to variable range hopping, and the super-Ohmic formula is only shown within the lowest order expansion.

5.11 Conclusion

Electronic charge transfer in boron-doped diamond at low temperatures is commonly assumed to be of variable range hopping nature. In this work, we observed dissipative quantum tunneling in lowly boron-doped polycrystalline diamond. Current-voltage traces taken from 4.5 K up to 100 K show an universal scaling behavior as a result of collapse of our data onto a single curve when plotting $T^{2\alpha-1}$ versus eV/k_BT . We showed that all assumptions of dissipative quantum tunneling in a double quantum well hold for our system, with an experimentally obtained ground state energy $E_0 = 41.8$ meV for the localized charge

carrier. Above 100 K deviations from the universal scaling behavior appear. We found that the onset of the deviations is in agreement with our calculated dissipation renormalized transition temperature $T_0 = 95 \pm 10$ K, which marks the critical temperature at which the system transitions from quasi-classical behavior to a purely quantum mechanical transport regime. Thus, one of our main results is a quasi-classical to quantum transition of the transport behavior of localized charge carriers within a series of quantum wells. Quantum mechanical tunneling in this experiment is mediated by a composite quasiparticle, consisting of an instanton and anti-instanton, referred to as the bounce solution within this quantum field theoretical tunneling model.

Chapter 6

Memristor

6.1 What defines a Memristor?

In 1971 Chua proposed a fourth fundamental two terminal electronic element, purely based on symmetry considerations of the governing equations of a resistor, a capacitor and an inductor. He labelled it a memristor [111], a contraction between memory and resistance, relating to the fact, that its resistance is dependent on the history of the device, the applied voltage and/or the current. Information can be stored in a conducting low resistive state (LRS) or insulating high resistive state (HRS) and, in addition, the memristor can switch between both states, all in one unit cell.

In electronic circuit theory four fundamental variables can be used to describe the operation of a resistor (i-v), a capacitor (q-v) and an inductor (ϕ-i), where v is the voltage, i is the current, q is the charge and ϕ is the magnetic flux. They are displayed in figure 6.1. Given the above relations, one can infer a fourth relation between magnetic flux and charge such that $d\phi = Mdq$, where M is the memristance given in Ohms. This

yields the relationship governing a memristor. Furthermore, in his original paper, Chua showed through a proof-of-concept realization that an active memristor can be built based on a complex configuration of linear and non-linear resistors, inductors and capacitors. It was pointed out that passivity (lack of internal power supply) might be one of the most important properties of the memristor device and that such a passive memristor device has not been realized yet. From a physical point of view, Chua provided an interpretation of a passive memristor in terms of an expansion of Maxwell's equations, concluding that a first order electric and magnetic field interaction can provide the characteristics of a memristor device and that such a memristor device will be driven by an alternating current source.

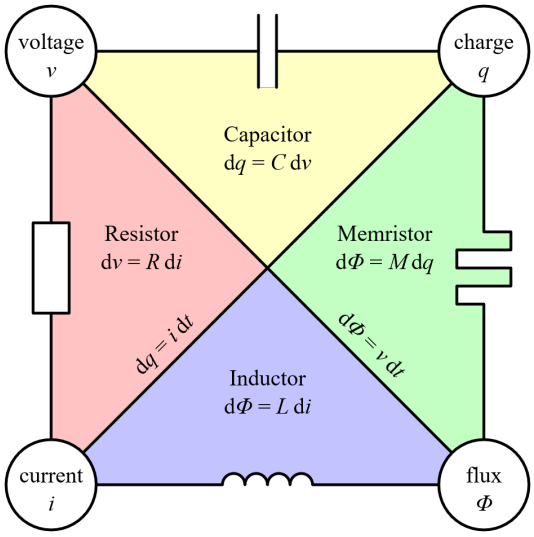

Figure 6.1: Graphical representation of four fundamental circuit variables i,v,q and Φ (corners), their mathematical relations between each other, and their respective circuit diagram symbols (edges). Graphic obtained from [112].

In 2008 Strukov et al. [113] published a letter, which claims to have found the missing memristor, referring to Chua's preceding 1971 paper. The authors provide their own physical model for the underlying working mechanism of a memristor, but agree with Chua

on the functionality of a memristor, which is to store and process memory. Storing memory is accomplished by the existence of a high and low resistive state, even when the voltage is turned off (non-volatility), the device remains in its set state. Processing memory is achieved by switching between high and low resistive states, which is a function of the applied voltage. The physical model for the memristor presented in [113] is based on coupled electronic and ionic transport across an ionic conducting layer, which substantially differs from Chua's model of coupled electric and magnetic first order fields. In general, Strukov's paper has attracted a lot of public attention and scientific scrutiny for several reasons. The underlying question of importance in this discussion can be reduced to 'What can be viewed or defined as a memristor?'. The short answer is, whatever we define it to be. On the one side, Chua provided a very specific definition and physical mechanism for a memristor, which nowadays is referred to as the real/ideal/perfect memristor. Then, Strukov's claim that this specific memristor has been found is misleading, since the real/ideal/perfect memristor according to Chua's 1971 model has not been found, as explained in depth by Vongehr and Meng [114]. This becomes apparent, when one considers the real/ideal/perfect memristor linking magnetic flux and electric charge flow. Vongehr and Meng [114] go as far as to claim that the real/ideal/perfect memristor is likely impossible, because magnetic monopoles might be necessary. On the other side, in 1971 Chua attributed the memristor with certain functionalities, such as the ability to store information in a non-volatile manner, and exhibit switching capabilities. This is really how Strukov's paper interpreted Chua's paper. Strukov viewed the memristor defined by what it can do rather then by the underlying physical principle of operation. Chua clarified in 2011 [115] by stating that a memristor is a two-

terminal device with non-volatile memory characteristics based on resistance switching, where the specific physical model or device material is not of importance. Such a concise statement could have avoided the preceding discussion and confussion of what constitutes a memristor and might have accelerated the development of memristive technology by years or even decades, since measurements of memristive devices have been published over the past 57 years [116, 117, 118], as early as 1962 [119], but they were never characterized as memristors.

6.2 Continuous Operation of an Undoped Polycrystalline Diamond Memristor

It is expected, that undoped diamond stays insulating over a wide range of applied voltages, due to its large indirect bandgap of 5.47 eV, see figure 1.4. Instead, our measurements paint a different picture. We have performed continuous mode current voltage measurements of undoped polycrystalline diamond foils for a diamond-on-graphene heterostructure as well as the bare surface of a diamond foil. In continuous mode the voltage is continuously swept up and down during a measurement procedure. An optical image of a typical device can be found in a previous chapter in the left part of figure 2.10. The right part shows a schematic side view of the device. A representative current voltage curve of our diamond memristor is displayed in figure 6.2. The measurement starts with an upward sweep from $0 \rightarrow 1$ in a high resistive state. After a certain set voltage is passed, the current shows a sudden jump to a preset current compliance value of 10 μA. The device switches into a low resistive state and the voltage is increased until it reaches its turning point at 2.

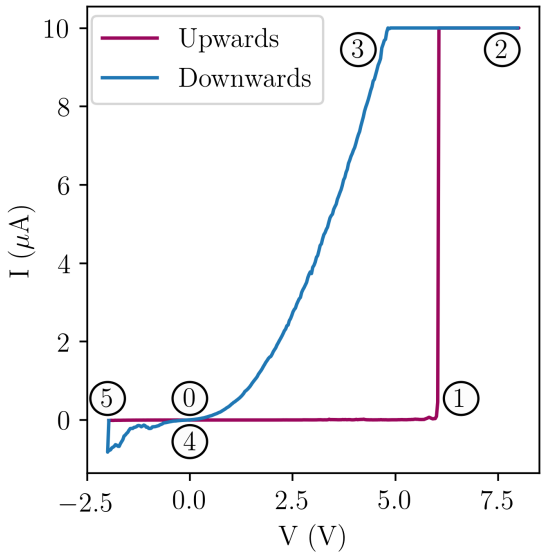

Figure 6.2: Current voltage trace of an undoped polycrystalline diamond-on-graphene heterostructure, operating as a bipolar memristor.

Then, the downsweep begins, where the current first remains at constant compliance value along $2 \rightarrow 3$. After reaching point 3, the current falls off, along $3 \rightarrow 4$, in a non-linear fashion. As it passes zero, it stays in a low resistive state, before it switches back into its high resistive state upon passing a certain reset voltage at 5. Moving along $5 \rightarrow 0$ brings it back to its initial starting point. Such a behavior is characteristic of a **bipolar memristor**. Our device exhibits a hysteresis loop in a I-V diagram in the 1st and 3rd quadrant and as such possesses a high and low resistive state. It is referred to as bipolar, because the reset voltage has an opposite sign compared to the set voltage. Furthermore, setting a value for current compliance in the experiment is extremely crucial, since it regulates the current flow upon the switching event. Too much current runs danger of permanently setting the device into its low resistive state. Next, we performed a series of 100 switching events in order to check for the reliability of our device, which can be found in the left plot of figure 6.3.

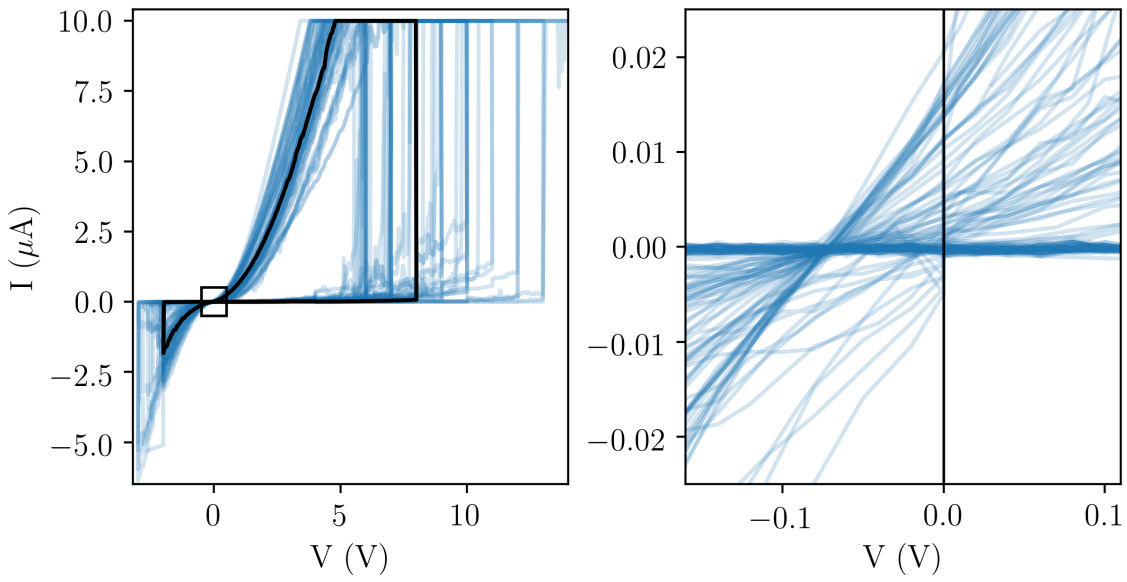

Figure 6.3: Left: One hundred switching events. Right: Zoom in exhibiting a nanobattery effect.

One observes, that the set voltage, the reset voltage, and the resistance in the low or high resistive state exhibit a certain variability. Such a behavior is not uncommon among memristive devices [120]. In general, variability is detrimental for switching applications, because a fixed set and reset voltage are required for faultless device operation. However, it does not always need to be a downside. It was shown recently [121], that variability in device performance can be exploited to operate an artificial neural network in the context of extreme learning machine architectures. The black curve shows a single switching event and the black square box centered around zero is the area which is enlarged in the right part of figure 6.3. Surprisingly, one finds that the zero crossing between LRS and HRS does not occur at 0 V, as indicated by the black horizontal line, but at -73 mV. This is in violation with the passivity requirements of a memristor. The memristor is supposed to be a passive device with a zero crossing property [115], meaning that for zero voltage, zero

current is expected. Such a built up internal voltage, points towards a nanobattery effect. In fact, Valov et al. [122] showed in 2013 that memristive elements based on ionic transport can show a nanobattery effect due to non-equilibirum states within the device and hence the zero-crossing property of a memristor can be violated in principle. They extended the memristor model to account for such an effect and labeled occurrences of memristors with a nanobattery effect as extended memristor systems.

So far, we showed that our undoped diamond memristor can be used to reliably switch between a HRS and a LRS. Switching between two distinct states is one of the requirements for a functional memristor device. Long time memory retention and a high ratio between on and off state are two additional requirements. The left plot of figure 6.4 shows the memory retention time for the low and high resistive state over a timespan of 20 hours. We prepared the memrsitor in its low resistive state and it remained stable over 20 hours (blue curve) at a fixed voltage of 2 V.

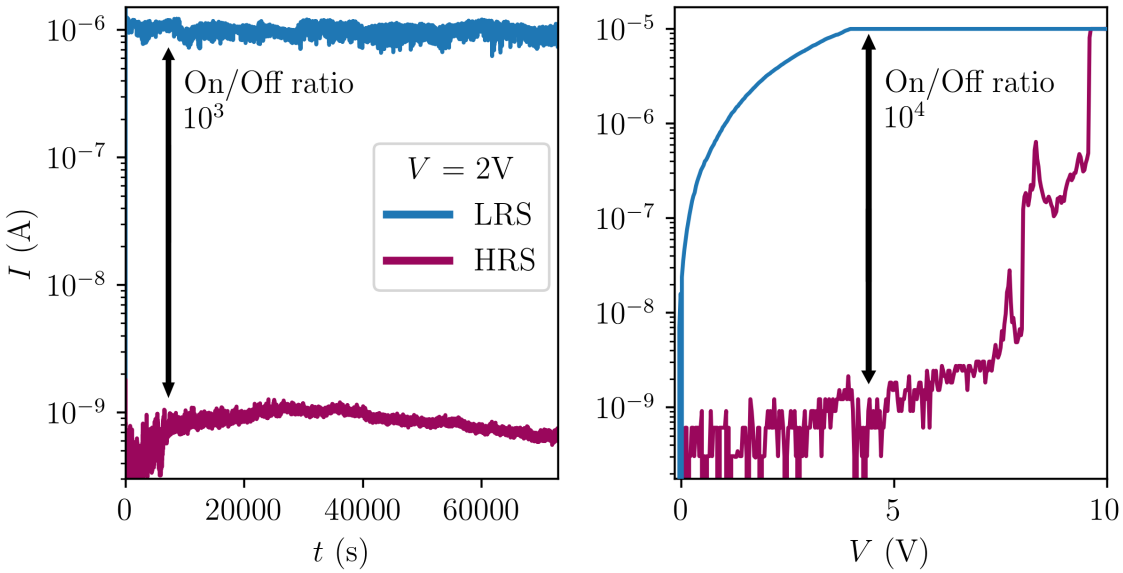

Figure 6.4: Left: Current versus retention time with a typical on and off ratio of 1000. Right: Maximum on and off ratio around 10000 measured.

The same is true for the high resistive state. Applying 2 Volts over 20 hours to the memristor in its HRS leaves it unchanged. Furthermore, we prepared our memristor device in its LRS and turned the external voltage off for 24 hours. We turned the voltage on and observed that our device was still in the LRS, demonstrating that our diamond memristor shows non-volatile memory behavior. A typical on/off ratio achieved in our memristor device is 10^3. In the right plot of figure 6.4 we observed a maximum on/off ratio of 10^4.

All in all, we have shown in this section that our diamond memristor exhibits the functionality of a memristor in continuous operation mode. It possesses a low and high resistive state for storing information in a non-volatile manner with sufficient retention times. Moreover, high on/off ratios and repeatability allow for information processing. An unusual internal build up voltage points to a nanobattery effect, which classifies our device as an extended memristive system.

6.3 A Hydrogen Redox-Based Switching Mechanism

In order to obtain a better picture of the underlying switching mechanism it is instructional to obtain specific information on the chemical composition and structure of our undoped diamond foils and its electrodes. For our memristor studies we have fabricated metal-insulator-metal devices, with bottom graphene and top Cr/Au (3 nm/400 nm) electrodes, see figure 2.10. Moreover, devices with two top electrodes of Cr/Au (3 nm/400 nm) were fabricated as well. During the growth of our undoped diamond foil, only two gases are present in the growth chamber, methane and hydrogen. In consequence, we anticipate our diamond foil to consist of a mix of carbon and hydrogen. Raman measurements

for undoped diamond, shown in figure 3.3, reveal a sharp charactersitic sp^3 diamond peak with a line width of $\sim$ 11 cm^{-1}, indicating structural disorder within the diamond phase. Additionally, a wider band around 1530 cm^{-1} is observed for an excitation wavelength of 532 nm, which is associated with amorphous carbon, more specifically with hydrogenated amorphous carbon a-C:H or ta-c:H [50]. Hydrogenated amorphous carbon is called a-C:H (ta-c:H) if the amount of sp^2 bonds is bigger (smaller) then the amount of sp^3 bonds. Hydrogenated amorphous carbon can be differentiated from non-hydrogenated amorphous carbon a-C, because a-C has a characteristic Raman peak centered around 1560 cm^{-1} for an excitation wavelength of 532 nm [50]. Scanning electron microscopy of the diamond top surface, shown in figure 1.7, reveals that the grain boundaries possess a different mass density than the grains. This observation leads us to presume that most of the a-C:H is situated at the grain boundaries. This assumption does not exclude that a-C:H is present in the grains as well, but with considerable less density. The general picture that we obtain from growth considerations, Raman measurements, and electron microscopy, is that a-C:H is rigidly suspended in a matrix of insulating sp^3 diamond.

Resistive switching of sputtered amorphous carbon films has been reported previously for several amorphous carbon phases, like a-C [123, 124, 125], ta-C [126], a-CO_x [127], and a-C:H [128, 129, 130, 127]. Specifically, a-C:H memristor devices can be either unipolar [129] or bipolar [130]. Both operation modes are considered to be due to the formation of a conductive graphitic sp^2 filament, as was suggested in [130] by showing that the resistance is independent of the electrode area, ruling out interface switching due to charge carrier accumulation over the whole electrode [131]. Yet, the underlying switching

mechanism is different in each case. In unipolar resistive switching the filament ruptures or dissociates during the reset process after an even higher current is passed through the filament than during the formation process. Exceedingly high local temperatures around the nm thin conductive filament break the filament itself. In bipolar resistive switching, Chen et al. proposed [130] a hydrogen redox-based resistive switching mechanism through proton migration for their a-C:H memristor devices. This model is in analogy to the commonly used redox-based mechanism of ion migration in transition metal oxides [132], like HfO_2, ZnO, TiO_2, MoO, Ta_2O_5, Nb_2O_5, MnO, NiO, and CuO, where oxygen anions migrate in terms of oxygen vacancies. Then, in Chen's model, setting and resetting a state is achieved according to dehydrogenation and hydrogenation of carbon-carbon bonds, as depicted in figure 6.5.

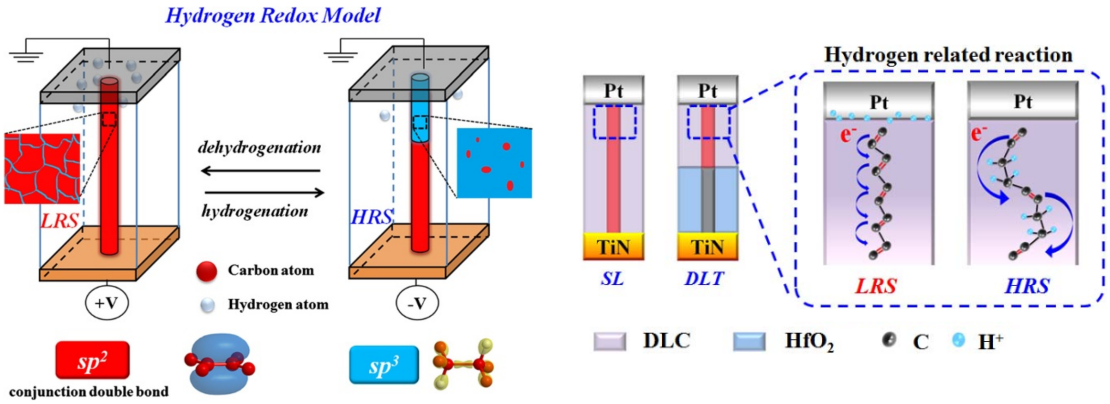

Figure 6.5: Hydrogen redox mechanism for resistive switching in a-C:H. Left: A low resistive state (LRS) and high resistive state (HRS) related through (de)hydrogenation [130]. Right: DLC stands for diamond-like carbon, which is a-C:H in this particular reference. The schematics show how hydrogen ions accumulate at the top electrode for the LRS and how they move back onto the conductive filament in the HRS and displace carbon atoms. Reprinted with permission from [133].

Suppose we start in the HRS. Applying a negative voltage to one of the electrodes attracts hydrogen ions towards the electrode. Given that enough hydrogen ions are with-

drawn from sp^3 bonds, a conductive sp^2 path can be established between top and bottom electrode. Consecutively, the device will switch into its LRS. This process is called dehydrogenation. Turning the voltage off is not sufficient to reverse it. A voltage of reversed polarity is required to reset the device into its off state, which is referred to as hydrogenation. In this model, atomic bonds undergo a transformation from sp^3 to sp^2 bonds, and vice versa. Even though the authors of this model did not explicitly state it in their publications [130, 133], a conversion of one type of bond to another type of bond over a sufficiently large area, can be considered a solid-solid phase transition [134]. Microscopically, the position of the carbon atoms is changed from a disordered towards a more ordered arrangement, which is referred to as displacive phase transition. See the right plot in figure 6.5 for a schematic illustration.

In summary, Chen's hydrogen redox-based resistive switching model allows us to explain our observed internal build up voltage in figure 6.3, in terms of separation of hydrogen ions from its conductive filament when the system is in its LRS. Furthermore, the hydrogen redox-based switching model allows us to explain observed memristive characteristics of our polycrystalline diamond films in terms of electronic and ionic charge transport.

6.4 Pulsed Operation of a Diamond Memristor

Next we investigate the switching behavior in pulsed operation mode. During a pulsed mode measurement the applied voltage is sent out in voltage pulses, as opposed to continuously sweeping the voltage during a continuous mode measurement. A voltage train with two pulse sequences and the response of a diamond memristor device can be seen in

figure 6.6. A single pulse sequence consists of a read (green), write (blue), read, and reset (magenta) progression. For this particular pulse sequence, the read time is 1 s, the write time is 0.5 s, and the reset time is 4 s. Hence, the pulse width t_W = 0.5 s, the pulse separation t_S = 6 s, the pulse amplitude for set and reset is Δ_S = +10 V and Δ_R = -3 V, respectively. High resistive and low resistive states are color encoded in magenta and blue, respectively.

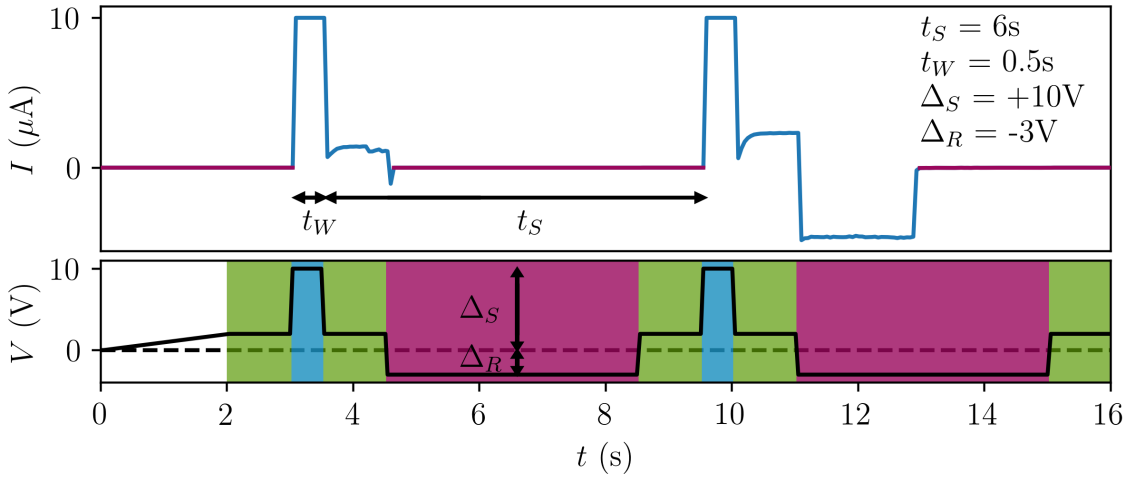

Figure 6.6: Pulse train and device response. Bottom: Voltage versus time showing two consecutive pulse sequences. Green, blue, and magenta colored windows correspond to the read, set, and reset operations. The white background is the ramp up period. Top: Response of a diamond memristor due to the bottom pulse train. HRS and LRS are color encoded in magenta and blue, respectively. Time widths and pulse amplitudes are provided in the legend.

A pulse train with a total of ten pulses and the device's response is shown in figure 6.7. Our memristor device is switched ten times between on and off state. We observe, that the duration for the conductive filament to break and switch the memristor into its off state varies. It either decays steadily (see t = 43 s) over a timescale of seconds or considerably shorter (see t = 18 s) than the timescales measured here. The on state can also persist (see t = 12 s) during the reset process, but it eventually decays. In principle, a study on the fault

tolerance of switching processes can be performed, but in the view of the memristors wide variability of onset voltages, offset voltages, and low resistive states, instead we continue to explore its physiological memory properties in the next section.

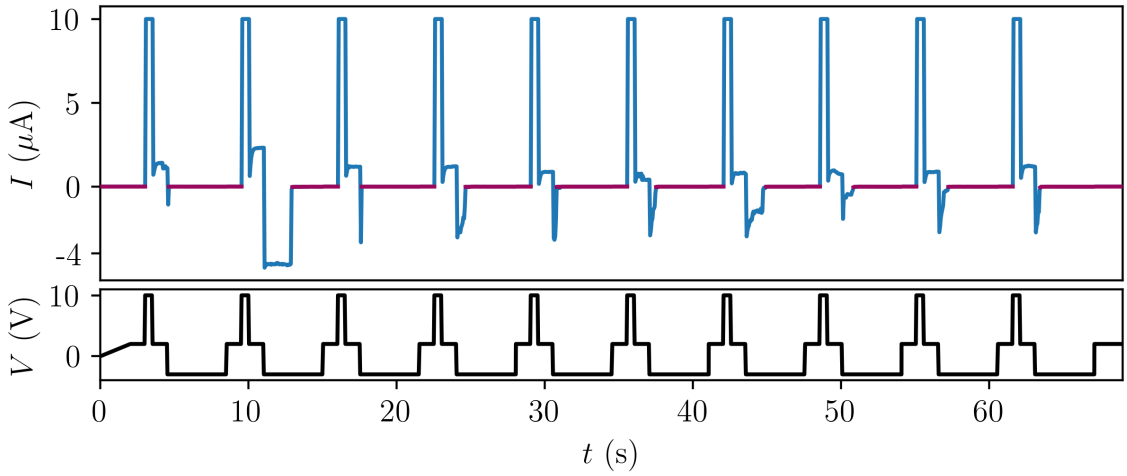

Figure 6.7: Pulse train and device response. Bottom: Voltage versus time showing ten consecutive pulses with $\Delta_S = +10$ V, $\Delta_R =$ -3 V, $t_W = 0.5$ s, and $t_S = 6$ s. Top: Response function of a diamond memristor. HRS and LRS are color encoded in magenta and blue, respectively. Ten switching events are performed.

6.5 The Diamond Memristor: An Inorganic Synapse and the Human Memory Model

In 2011, Ohno et al. [135] presented a AgS_2 memristor device which acts as an inorganic synapse and exhibits memory effects according to the psychological human memory model by Atkinson and Shiffrin [136]. Although, synaptic behavior of memristor devices was shown previously [137], Ohno made a connection to the human memory model, which is shown in the left part of figure 6.8. It is a three stage model which possesses a sensory memory (SM), also referred to as a sensory register, a short term memory (STM), and long term memory (LTM).

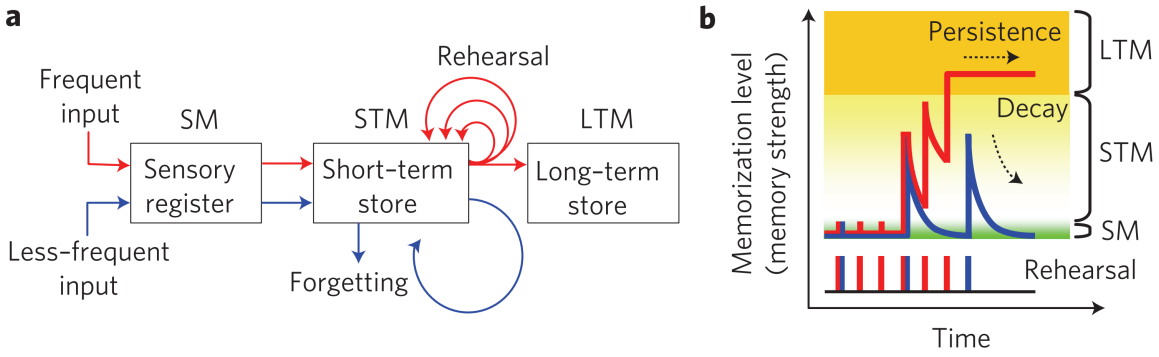

Figure 6.8: a) Human memory model from [135], developed by Atkinson and Shiffrin [136]. b) Response of an inorganic synapse with respect to the human memory model.

Incoming information enters the SM where it is registered. The sensory register acts as a filter and most incoming signals decay and vanish. Only a selected subset of incoming signals is transferred into STM and is stored temporarily. Information in the STM will eventually be forgotten, unless it is rehearsed. Then, the possibility exists to enter into LTM. Long term stored memory can also be passed down into short term memory and can be forgotten. Less frequently incoming information is either sorted out at the SM or STM and as a consequence forgotten, while higher frequently incoming information can result in learning and remembering. SM, STM, and LTM are expressions commonly used in psychology.

In neuroscience a microscopic picture of memory exists in terms of connections between neurons. The interface between two neurons is called a synapse, illustrated in figure 6.9. Two physically connected neurons are commonly referred to as a pre- and post-neuron, with reference to an incoming signal traveling past both neurons. Depending on the coupling between two neurons, a synapse can be conducting or insulating for either electronic or ionic charge transfer. The strength of the coupling is referred to as synaptic strength. Over time, the synaptic coupling between neurons can change, it can become

weaker or stronger, and this property of the synapse is called synaptic plasticity. In particular, spike-timing dependent plasticity can adjust the coupling between two neurons. The more frequently a pre-neuron releases an action potential which reaches the synapse, the stronger the coupling between pre- and post-neuron will be. This behavior is directly linked to the psychological human memory model, where less frequent stimulation results in STM of information, while more frequent stimulation results in LTM storage. In neuroscience the corresponding expressions are short term plasticity (STP) and long term plasticity (LTP), referencing the amount of time (short or long) in which the adjusted synaptic coupling will remain.

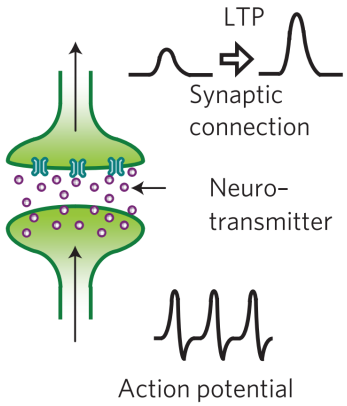

Figure 6.9: A sketch of a biological synapse. An incoming action potential triggers ionic neurotransmitters to cross the interface and establish a conductive electronic coupling between bottom and top neuron. Reprinted from [135].

6.5.1 Sensory Effects

In our memristor device we measure two different types of sensory effects, upon applying a voltage train on the memristor in its HRS. The first is shown in figure 6.10. Applying ten voltage pulses of 8 V for a duration of $t_W = 0.5$ s and a separation of $t_S = 2$ s, leaves the memristor in its HRS. For the duration of the pulse a small leakage current flows

through the device. In terms of the filamentary model with its hydrogen redox reaction this measurement can be interpreted as the filament being not fully hydrogenated. Hence, the metal-insulator-metal memristor constitutes a leaky capacitor.

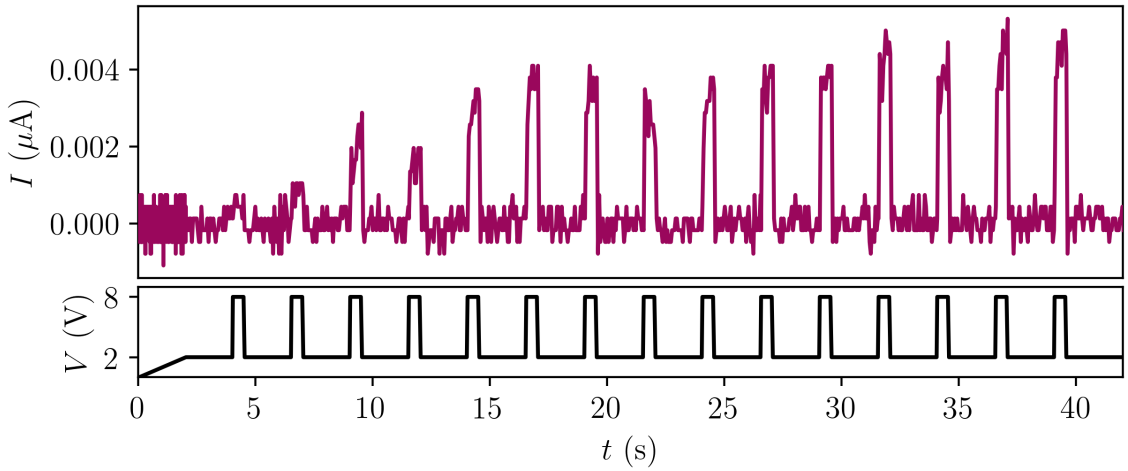

Figure 6.10: Sensory effects of a memristor's high resistive state (type I). Bottom: Applied voltage pulse train with pulse height $\Delta_S = 8$ V. Top: Memristor's response with $t_S = 2$ s, $t_W = 0.5$ s.

On the other hand, figure 6.11 shows the behavior of a non-leaky capacitor. Upon applying the first voltage pulse, two transients are measured. One when the capacitor is charged and one when the capacitor is discharged. Over a sequence of 10 pulses this behavior is reproducible, showing that the filament is fully hydrogenated. Distinguishing between partially and fully hydrogenated filament is important, because a partially hydrogenated filament reduces the onset voltage for the switching event, leading to an increased variability of device characteristics. Therefore, future work into properly hydrogenating a conductive filament could result in improved device performances. In the synaptic picture of our memristor device, the coupling between the two neurons is only very weak or non-existent. An incoming signal is not transmitted to the next neuron.

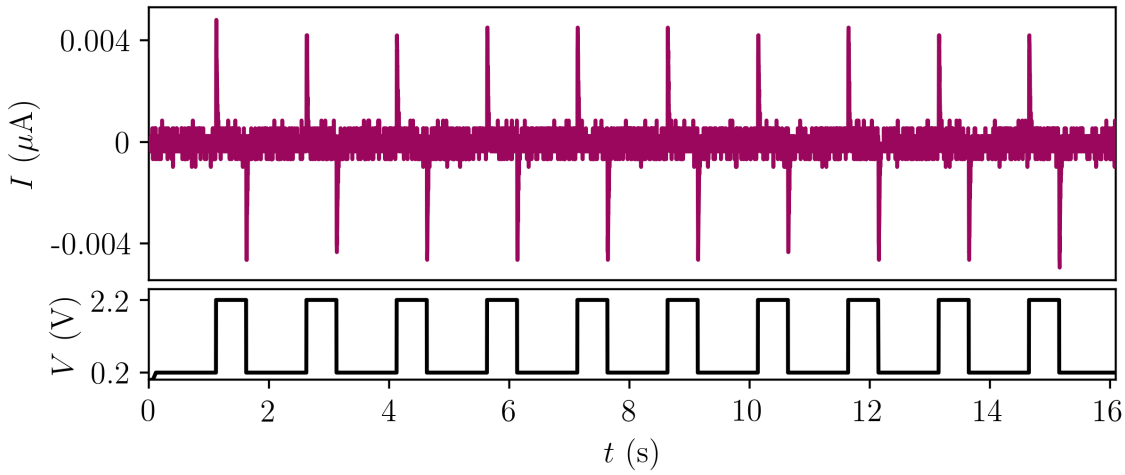

Figure 6.11: Sensory effects of a memristor's HRS (type II). Bottom: Applied pulse train with a pulse height of 2.2 V. Top: The response of the diamond memristor to the bottom pulse train with $t_S = 1$ s, $t_W = 0.5$ s.

Next we will investigate the voltage pulse height dependence of a fully hydrogenated filament. At first, a pulse sequence consisting of 15 separate pulses of pulse height $\Delta_S = 2$ V, pulse width $t_W = 0.3$ s and pulse separation $t_S = 3$ s is applied and its response measured. The pulse height is increased to 3 V and the pulse sequence is repeated. This procedure is continued until a maximum pulse height of 9 V is reached. Our obtained data is presented in figure 6.12. A single pulse and the pulse train are shown in the left and right bottom row, respectively. Color encoded are the different pulse heights ranging from 2 to 9 Volts. The top right plot shows the response of the memristor in its HRS to the pulse train and the top left part shows the response to a single pulse. The transient peak at $t = 2.27$ s is proportional to the pulse height over the whole range of applied voltages. Up to 7 V the response of the memristor resembles a fully hydrogenated filament such that no leaky current passes through the HRS. Only the charging and discharging of a capacitor upon applying a voltage change is measured. For 8 V the filament becomes more conductive during

the applied pulse and a small amount of current is allowed to leak between the electrodes, suggesting the onset of a formation of a conductive sp^2 filament. At 9 V the filament starts to become even more conductive. Dehydrogenation progresses during the pulse to a degree where the current is increased until a steady state is reached. The current response of the memristor to the other 15 pulses of the pulse sequence can be found in appendix A.1.

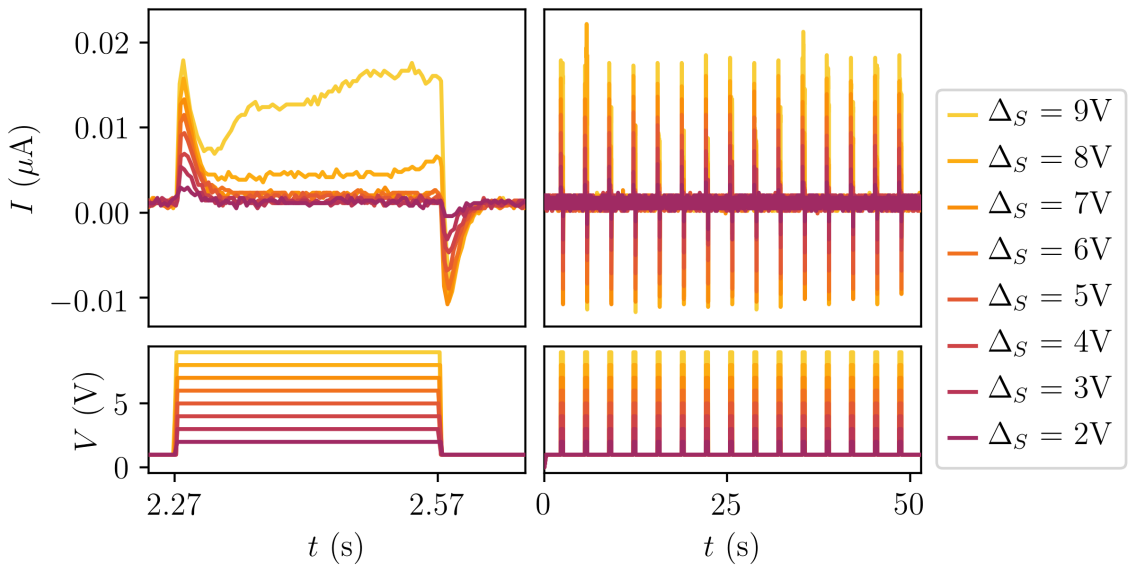

Figure 6.12: Memristor response to a pulse train with varying pulse heights initially prepared in a high resistive state. Bottom left: Single pulse. Bottom right: Applied pulse train with 15 pulses for different pulse heights Δ_S, where $t_S = 3$ s, $t_W = 0.3$ s. Top Right: Response of the diamond memristor to the bottom pulse train. Top Left: Respond of the memristor to a single pulse.

6.5.2 Short Term Memory and Short Term Plasticity

In order to switch from a HRS to a LRS one can experimentally increase the applied voltage, the pulse duration or the total number of pulses. We choose to increase the total number of pulses and decrease the pulse separation. Figure 6.13 shows a sequence of 30 pulses with Δ_S =8 V, $t_S = 2$ s and t_W= 0.5 s on a semi-logarithmic plot for the current flow. As the voltage train proceeds, the measured current potentiates in a non-linear fashion.

Sudden drops in the measured signal are visible, pointing towards an unstable and short term potentiation at the synapse. Such an unstable potentiation could be understood as a precursor for forgetting, but further evidence is required.

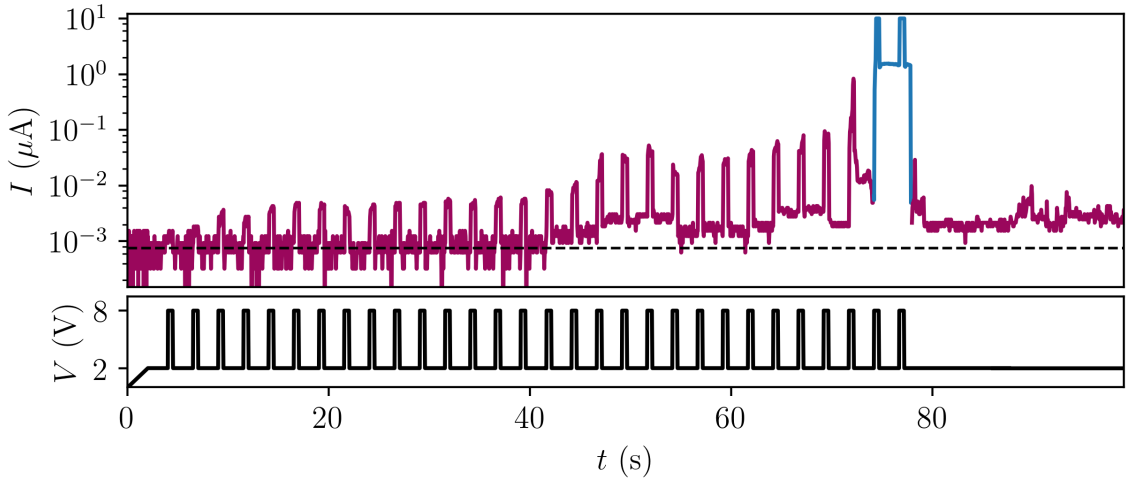

Figure 6.13: Short term memory with forgetting. Bottom: Voltage pulse train consisting of 30 pulses with Δ_S= 8 V, t_S= 2 s and t_W= 0.5 s. Top: Memristor response. Eventually the meristor switches to its low resistive state (blue), but decays into its high resistive state.

Eventually, the memristor switches into its LRS, shown in blue, and decays quickly into its HRS after the pulse sequence ends. The synapse indeed exhibits short term plasticity and the pre- and post-neuron only couple for a short amount of time. In a human memory model this corresponds to forgetting, while switching from the off to the on state corresponds to learning. The tail at the end of the pulse train is under a 2 V bias and shows a stochastic behavior. The experimental voltage pulse height in this section is smaller by 1 Volt than in the previous section 6.12. The question arises of how it is possible that the device switches to its LRS for this pulse train but not in the previous section. At first, we identify, that the sensory register of the memristor is of type I in this measurement, corresponding to a leaky not fully hydrogenated filament. Additionally, the number of pulses is doubled and the

pulse width increased, so the overall delivered energy is greater compared to the previous section. Another explanation could be, that multiple filaments contribute to the overall switching behavior, which results in a variability of the switching process.

6.5.3 Long Term Memory and Long Term Plasticity

Next, the device is turned off by applying a negative voltage of -3 V and then we send out another pulse train consisting of 30 pulses. This time we increase Δ_S slightly to 9 V, and keep the pulse width and separation constant. We observe that the overall current baseline during the readout phase increases continuously on a semi-logarithmic plot, contrary to what was measured in the previous section. From the synaptical point of view, this corresponds to a long term potentiation of the incoming signal pointing towards a long term plasticity effect at the synapse. After the memristor switches into its low resistive state, the result is that it stays in it for an extended time at a constant current level. Indeed, the coupling between the neurons is for the long term.

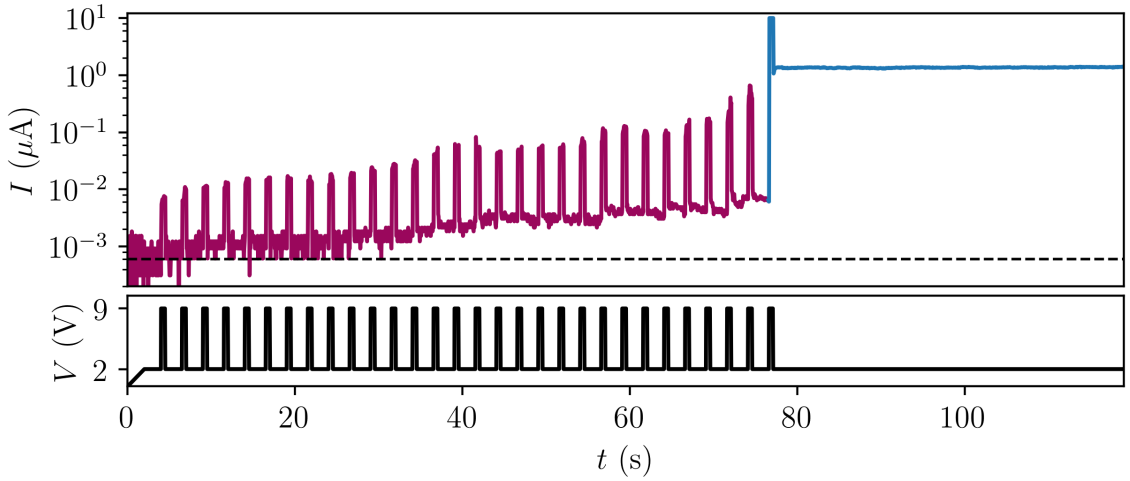

Figure 6.14: Long term memory. Bottom: Voltage pulse train consisting of 30 pulses with $\Delta_S = 9$ V, $t_S = 2$ s and $t_W = 0.5$ s. Top: Memristor response. Its LRS persists.

The incoming signal is stored in a stable filament which translates to long term memory storage in Atkinson and Shiffrin's psychological human memory model. Applying a follow-up pulse train, shown in figure 6.15, does not disturb the LRS significantly nor are any turbulences or stochastic processes visible. The memristor device remains in its LRS. The incoming signal is stored in a long term memory configuration. The inset shows a dip in the measured current after each voltage pulse is turned off, which will be investigated in section 6.7.

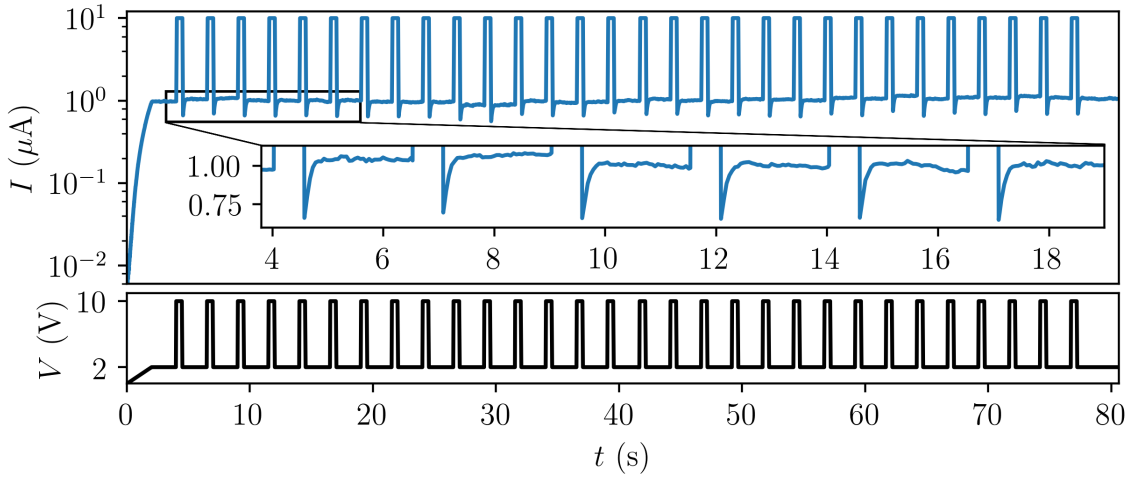

Figure 6.15: Persistence of long term memory. A follow-up voltage train with 30 pulses. The memristor device remains in its low resistive state without bigger turbulences.

6.6 Spike-Timing Dependent Plasticity

There is still one component of the human memory model that needs to be verified experimentally in our diamond memristor, which is its frequency dependence. In neuroscience, spike-timing dependent plasticity refers to adjusting the synaptic connection between two connected neurons. The more frequently a neuron fires a signal, the more probable it is that a synaptic connection is established or enhanced. Likewise, the lower

the frequency of the incoming pulse sequence the lower the probability that the system will change into its LRS. Therefore, we turned the device off by applying a negative voltage of -3 V and then applied the same pulse width of 0.5 s as in the previous section, but we increased the pulse separation from 2 s to 8 s, the pulse height from 9 V to 10 V, and the number of pulses to 56. The total time of the pulse train is 480 s, see figure 6.16. We observe, that the system stays in its HRS over the whole sequence. The baseline increased only marginally on a semi-logarithmic plot, considerably less than in the case of short term and long term potentiation. Hence, this observation confirms the last element of Atkinson and Shiffrin's human memory model, and we conclude that our diamond memristor exhibits the building blocks of a human memory model, which in a neuroscience environment translates into synaptic behavior between physically connected neurons.

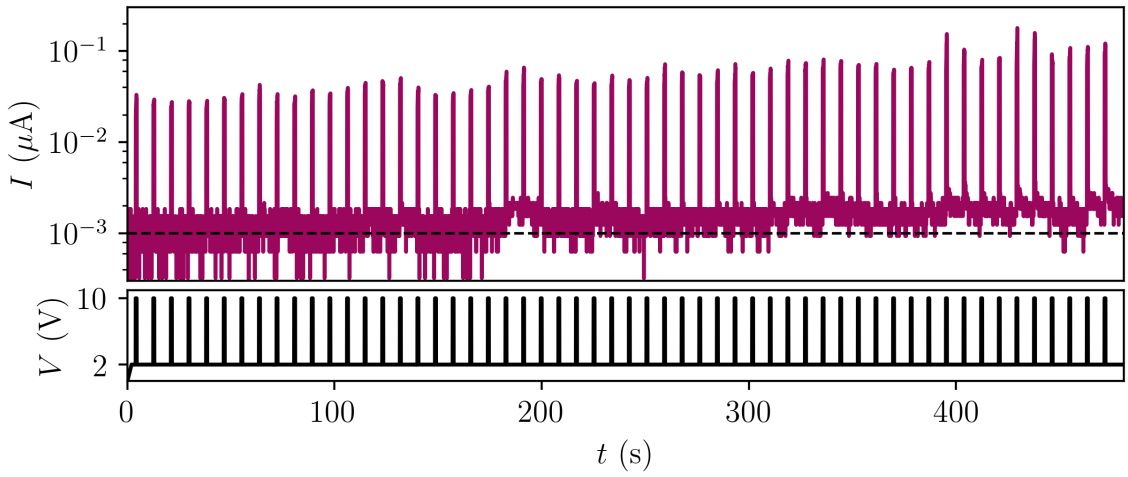

Figure 6.16: Spike-timing dependent plasticity. Bottom: 56 consecutive pulses over a time span of 480 s with $\Delta_S = 10$ V, $t_S = 8$ s and $t_W = 0.5$ s. Top: The system stays in its HRS. The baseline increased only marginally.

I would like to end this section with a short anecdote of a former teacher of mine, that came into my mind at this point. Teacher speaking to students: 'Who do you think

is the best teacher out there?' While the students react suprised about this question the teacher continues: 'Repetition, repetition, repetition.'

6.7 Mimicked Refractory Period

Next, we will investigate the dip observed in the inset of figure 6.15. After the voltage pulse is turned off a dip occurs in the measured current through the memristor device. In order to exclude a parasitic effect from external circuitry, we removed the current compliance and tested a freshly prepared device. The device starts in its HRS and at a voltage of 29 V a small current peak appears which is followed by a larger peak at 31 V, reaching almost 1 mA before it decays again, see left plot in figure 6.17.

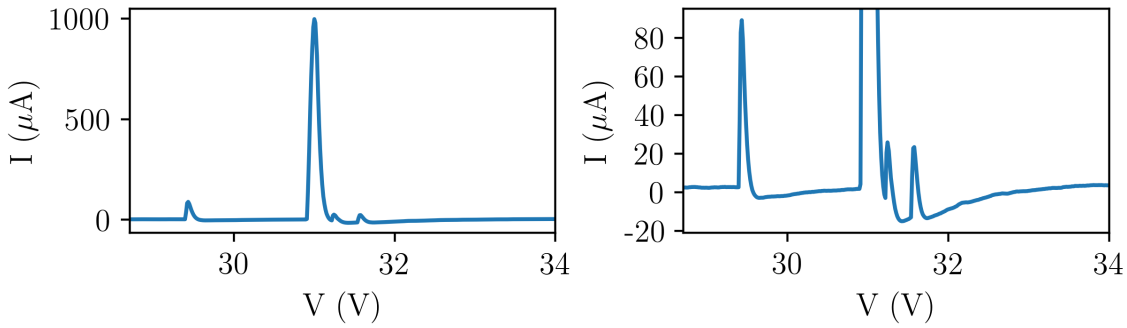

Figure 6.17: Voltage sweep of a freshly prepared memristor device without current compliance. The right plot shows a zoom in of the left plot. Notice that the current dips below zero for the small and the large peak.

The right plot shows a zoom in and it becomes visible, that a dip similar to the one in figure 6.15 appears. Furthermore, the dips goes below zero for both peaks. The larger the peak, the larger the following dip with up to almost -20 μA. While the voltage sweep continues, the current converges towards zero from negative values. It can be concluded, that the observed dip is not due the current compliance and s physical current flows in the

opposite direction.

Figure 6.18 shows a pulse sequence consisting of three pulses with varying pulse height, similar to what was presented in section 6.5.1 figure 6.12, with the difference that here the memristor was initially prepared in its LRS instead of its HRS.

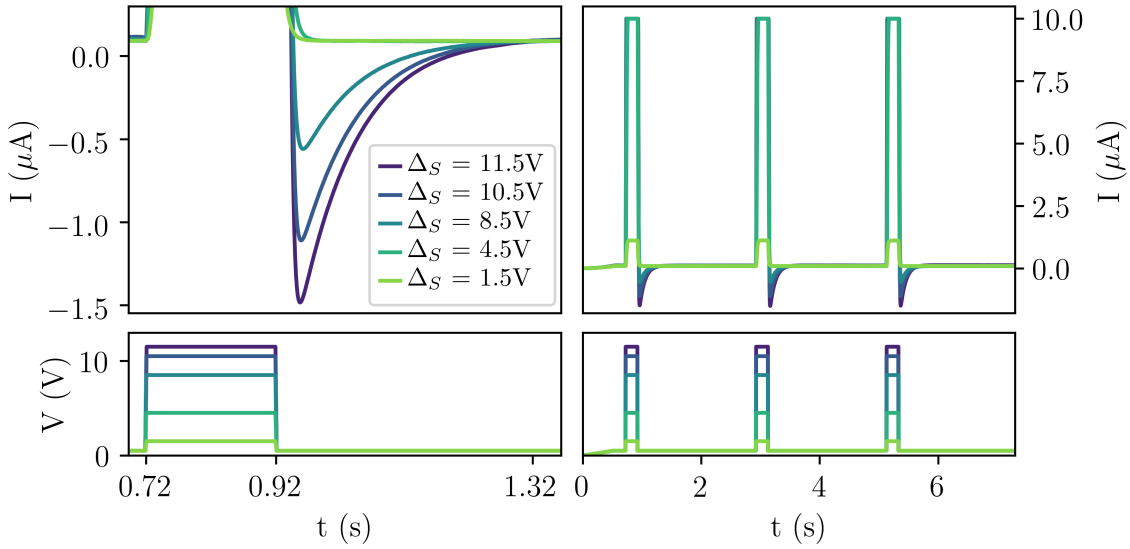

Figure 6.18: Memristor response to a pulse train with varying pulse heights initially prepared in a low resistive state. Bottom left: Single pulse. Bottom right: Applied pulse train with 3 pulses for different pulse heights Δ_S, where $t_S = 2$ s, $t_W = 0.2$ s. Top Right: Response of the diamond memristor to the bottom pulse train. Top Left: Respond of the memristor to a single pulse.

The top left plot shows a clearly visible dip which drops below zero. Only a very low read out voltage of 0.5 V is applied after the pulse. A clear voltage dependence of the dip is visible. The larger the applied voltage pulse, the larger the dip will be. Somewhere between 4.5 V and 8.5 V is a crossover voltage and the dip disappears. The current response of the memristor to the other two pulses of the pulse sequence can be found in appendix A.3. Furthermore, appendix figure A.2 shows clearly how the current dips below zero for the first voltage pulse while the system is decaying from an unstable

short term potentiation state towards the off state of the memristor. A clear separation in time is visible between the dip and dV/dt at the end of the pulse, excluding dV/dt at the end of the pulse as the origin of the dip. Such a behavior of the observed dip can have different origins. Considering the hydrogen redox-based switching model discussed in section 6.5, in combination with the nanobattery effect measured in figure 6.3, we reach the conclusion, that the observed dip is the result of a built up internal potential difference, which is opposite in direction to the applied voltage and which results from the ionic migration of protons through atomic vacancies. Since the current compliance limits the amount of voltage drop along the electronic path, the leftover voltage will cause protons to diffuse away towards the negatively biased electrode. Additionally, this diffusion process is accelerated by the local high temperatures produced by the current carrying filament. While current compliance is not necessary for this effect to occur it is certainly helpful. The ionic liquid of protons produces a build up diffusion potential difference across the device. Based on our results, it is not conclusive to say whether the dip is solely due to an ionic current or a mix of electronic and ionic contribution. But, it can be excluded that it is just due to an electronic current, because protons will relax from their concentrated configuration near the negative electrode, since otherwise a persistent negative current would be measured. Last but not least, we point out, that the build up of a potential difference due to migration of ions is precisely what causes a refractory period when an action potential travels along an axon. In our case we have only one species of migrating ions, namely protons. For the case of axons, sodium and potassium ions are transported across the axon membrane through ion channels, which close and open. Then, the refractory period is a result of build of potential

difference due to difference in the ion concentrations inside and outside the axon, inhibiting the occurrence of a follow-up action potential. Such a parallel between the behavior of our memristor device and the refractory period observed in an action potiental travelling through an axon might suprise at the first sight. However, Chua claimed that the Hodgkin-Huxley axon is made of memristors [138], and hence it should not be uncommon to observe action potential-like behavior in memristive devices.

6.8 Conclusion

We have successfully fabricated the first diamond-based memristor. The underlying switching mechanism is a filamentary hydrogen-redox based hydrogenation and dehydrogenation process of hydrogenated amorphous carbon within the diamond film. Furthermore, we showed that our diamond-based memristor exhibits sufficient retention times and high on and off ratios required for logic operations. An unusual internal nanobattery effect categorizes our devices as an extended memristive system. We observed resistive switching behavior on three different devices. Each them showed an undesired device variability, which needs to be addressed in future studies. Additionally, we found that our memristor behaves like an inorganic synapse, which shows effects of long time, short time, and sensory memory, according to the psychological multi-stage human memory model. The effects of learning and forgetting were demonstrated as well. Spike-timing dependent plasticity in our inorganic synapse displayed the frequency dependent effect of incoming signals on the ability to learn and remember. Last but not least, we observed that our inorganic synapse mimicks a refractory period commonly observed when neurons fire off action potentials. We

concluded that the origin of this mimicked refractory period results from an internal build up potential difference due to the migration of protons, very similar to the migration of ions into and out of an axon during an action potential.

Chapter 7

Barristor

In this study, we present the first realization of a diamond-on-graphene barristor. Lowly boron-doped diamond, with 266 ppm boron to carbon atoms, was used in this study as a p-type semiconductor. In particular, we were interested in the high temperature operability of the diamond-on-graphene heterostructure up to 300°C. At elevated temperatures silicon based electronics breaks down, due to material degradation and due to the fact that thermally excited charge carriers are able to hop over the barrier height in a semiconductor. Thus, diamond and graphene should provide enhanced performance characteristics at elevated temperatures, owing to their exceptionally high thermal conductivities. An exemplary device layout and optical image of a diamond-on-graphene device can be found in section 2.3.11, figure 2.9. Our device is capped of with 3 μm of PMMA in order to prevent chemical reaction with any surrounding nitrogen flowing through the furnace and to make sure that diamond sticks well to graphene.

7.1 Graphene-on-Silicon Barristor

A barristor is a variable barrier height diode. The first barristor was fabricated by Yang et al. in 2012 in the form of a triode device [139]. Yang et al. showed that the interface of a two terminal graphene-on-silicon (p-doped or n-doped) heterostructure constitutes a diode. Furthermore, a third terminal was used as a top gate in order to tune the Fermi level of graphene through the electric field effect. Tuning the Fermi level of graphene resulted in adjustment of the barrier height of the diode itself. Therefore, the first operable graphene-on-silicon barristor, and the first barristor in general, was realized. Moreover, their barristor showed large enough on/off ratios of $\sim 10^5$ to meet the requirements of logic transistor operations.

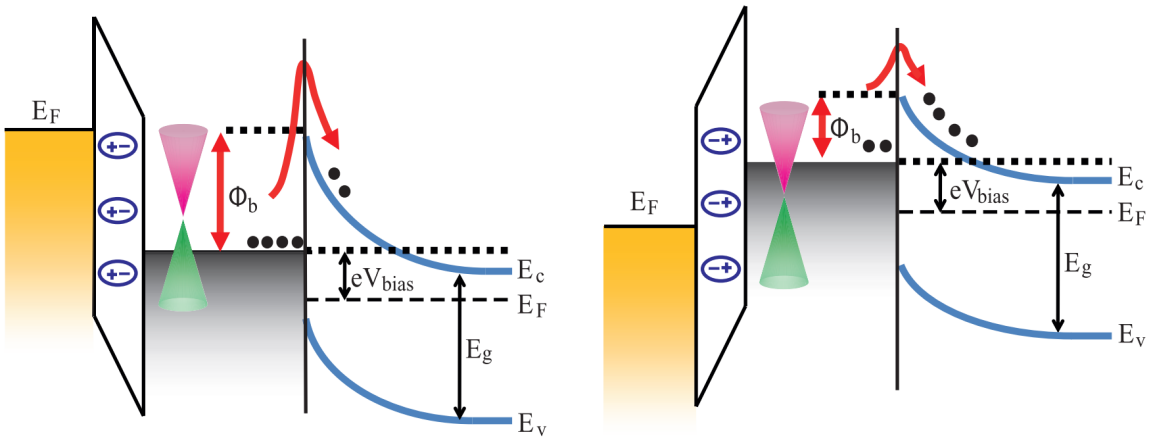

Figure 7.1: Schematics of a barristor device under constant voltage V_{bias}. Left: The Dirac cone represents the graphene sheet which is capacitively coupled to the top gate (yellow). In blue one sees the valence and conduction band of silicon. Right: Upon changing the Fermi level in graphene the barrier height Φ_b is lowered and more current flows through the device. Reprinted with permission from [139].

A schematics showing the barristor's principle of operation is presented in figure 7.1. The barristor device is under constant bias V_{bias} and the Fermi level is coupled capacitively to the backgate (yellow). Graphene forms a Schottky barrier Φ_b with silicon, whose

valence and conduction band are shown in blue. Changing the backgate voltage, while holding the bias voltage constant, tunes graphene's Fermi level and changes the Schottky barrier height, such that either more or less current can flow through the barristor.

7.2 Measurement protocol

Our measurement protocol for high temperature measurements of current-voltage (IVs) traces has 9 steps and it alternates between holding and sweeping temperatures as follows:

1. Hold at 22°C and measure backgate (±60 V) dependence of IVs.
2. Sweep from 22°C to 100°C and take IVs at $V_G = 0$ V.
3. Hold at 100°C and measure backgate (±60 V) dependence of IVs.
4. Sweep from 100°C to 200°C and take IVs at $V_G = 0$ V.
5. Hold at 200°C and measure backgate (±60 V) dependence of IVs.
6. Sweep from 200°C to 300°C and take IVs at $V_G = 0$ V.
7. Hold at 300°C and measure backgate (±60 V) dependence of IVs.
8. Sweep down from 300°C to 22°C and take IVs at $V_G = 0$ V.
9. Hold at 22°C and measure backgate (±60 V) dependence of IVs.

Essentially, the temperature is raised from 22°C to 300°C successively with stops at 100°C, 200°C, and 300°C, before the system is cooled down again. A visualization of the temperature sequence can be found in 3.7.

7.3 Diamond-on-Graphene Barristor

Figure 7.2 shows IV traces of a lowly boron-doped (266 ppm) diamond-on-graphene barristor at room temperature exhibiting a slightly leaky diode behavior. A clear tunability of the Schottky barrier height is visible, owing to the adjustment of graphene's Fermi level due to a capacitve coupling between graphene and the applied backgate voltage. The tunability of the barrier height was not strong enough to turn off the device completely within the range of applied backgate voltages.

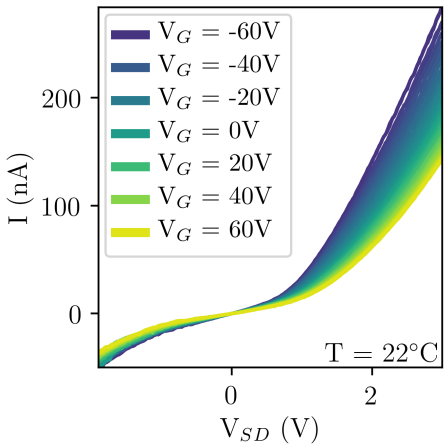

Figure 7.2: Step 1. Room temperature tunability of a diamond-on-graphene heterostructure. The backgate is tuned between ±60 V.

During the next step in the measurement protocol, step 2, the temperature is raised from 22°C to 100°C, the back gate dependence is set to zero, and IV traces are obtained, see the left plot of figure 7.3. It is observed, that up to 80°C very little changes in the IV traces and that upon passing 80°C the IV characteristics transition towards an enhanced diode behavior. The current is strongly rectified for a forward bias and suppressed for a backward bias. The corresponding Arrhenius plot resulting from the low bias conductance is shown in the right plot of figure 7.3. It shows that the diamond-on-graphene interface exhibits

a constant conductance up to 80°C, indicating metallic behavior. This might stem from the hydrogen terminated diamond surface in combination with a H_3O^+ adsorbate layer, which is known to produce a metallic conductive surface layer on diamond [77, 140]. Once this thin water adlayer, originating from the environment during the fabrication process, is removed, for example through placing the sample in a high vacuum [77], or potentially, like in our case, through heating up the sample in an inert and encapsulated environment, the conductance is expected to decrease. This is what we observe above 80°C.

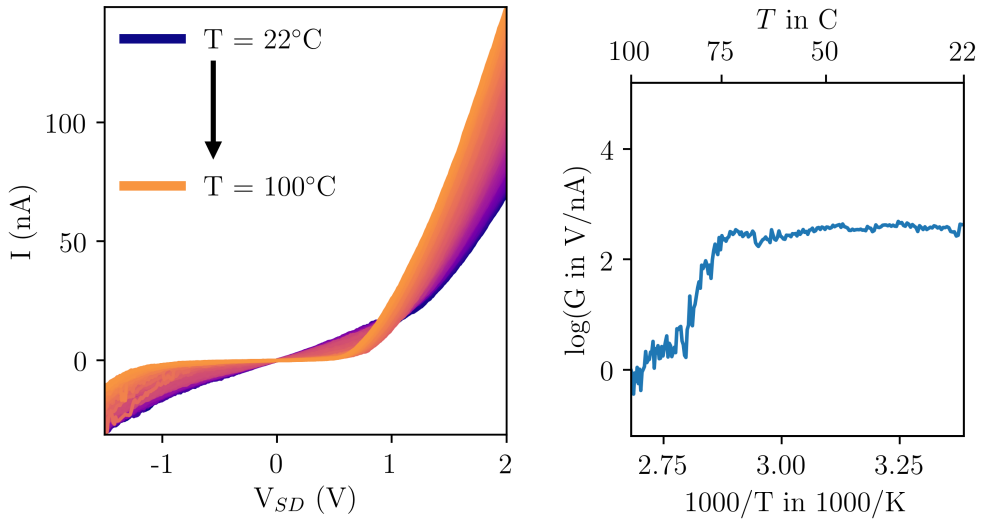

Figure 7.3: Step 2. Left: IVs recorded from 22°C to 100°C. Right: Arrhenius plot of the low bias conductance. A top axis is included for better readability.

Step 3 investigates the backgate dependence at 100°C in figure 7.4. Our diamond-on-graphene device shows a strong diode behavior and tunability of the Schottky barrier. This constitutes an operable high temperature diamond-on-graphene barristor. Unfortunately, compared to room temperature the tunability of the Fermi level is decreased and again no propper off state can be achieved through the backgate. On the other hand, a proper off state could be achieved by alternating the polarity of the source drain bias, but

this would simply correspond to a regular diode and burn off a considerable amount of power, since the direction of charge carriers is constantly changed. Hence, a tunability of the backgate is desired.

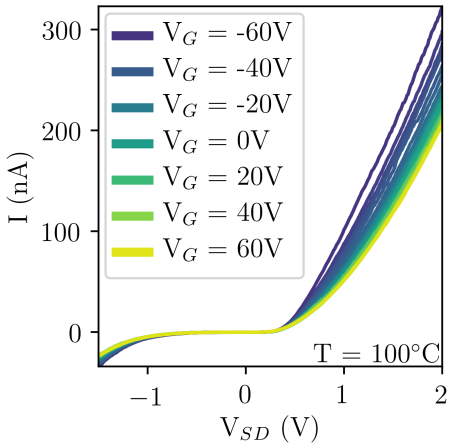

Figure 7.4: Step 3. Barristor behavior at 100°C.

We continue to increase the temperature from 100°C to 200°C, shown in figure 7.5. On the Arrhenius plot the conductivity increases with increasing temperature in a non-linear fashion. This indicates that electronic transport is semiconducting and differs from nearest neighbour hopping. A non-linear Arrhenius plot at elevated temperatures is indicative of variable range hopping, see section 4.3. The conductance reaches a maximum shortly before 200°C. From the IV traces we observe that the diode behavior is steadily lost towards 200°C, where the IV trace becomes almost symmetric.

Surprisingly, step 5, the backgate dependence at 200°C, shows and enhanced tunability of the Schottky barrier height, and the diode reversed its direction of operation, see figure 7.6. Current is preferably transferred at negative V_{SD} and partially blocked at positive V_{SD} at high positive backgate voltages.

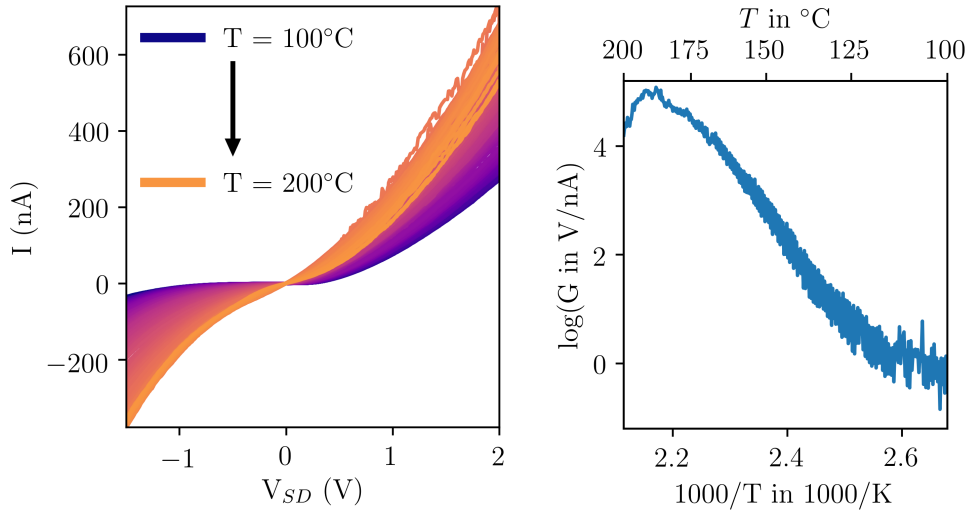

Figure 7.5: Step 4. Left: IVs recorded from 100°C to 200°C. The diode behavior is gradually lost as the IV traces become symmetric. Right: Arrhenius plot of the low bias conductance showing semiconducting properties. A top axis is included for better readability.

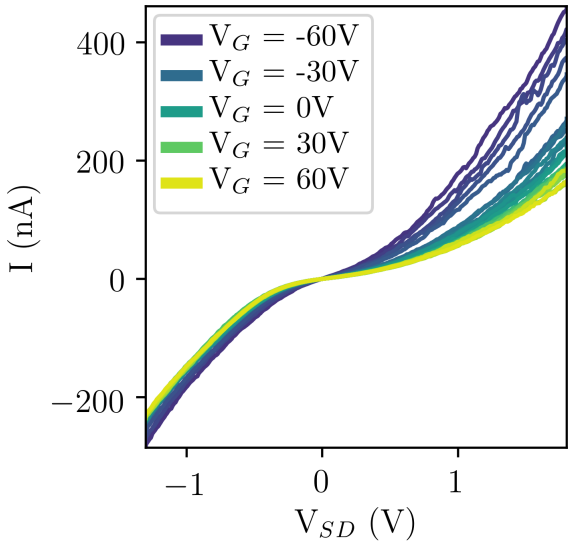

Figure 7.6: Step 5. Current voltage characteristics at 200°C.

This behavior continues in step 6, see left plot in figure 7.7 in particular at T = 200°C. Upon increasing the temperature to 300°C the IV traces become more noisy. The Arrhenius plot shows that the low bias conductance stays fairly constant up to 260°C, corresponding to metallic behavior, before it slightly increases again. It is not clear at

this point what initiates the changes in the electronic behavior of the diamond-on-graphene device for the conductance and the IV traces, but we speculate that possibly a surface reconstruction at the diamond-graphene interface occurs.

In step 7, the noise of the IV traces is increased and the tunability of the Fermi level of graphene is lost and the diode behavior as well, since the IV traces are symmetric around zero.

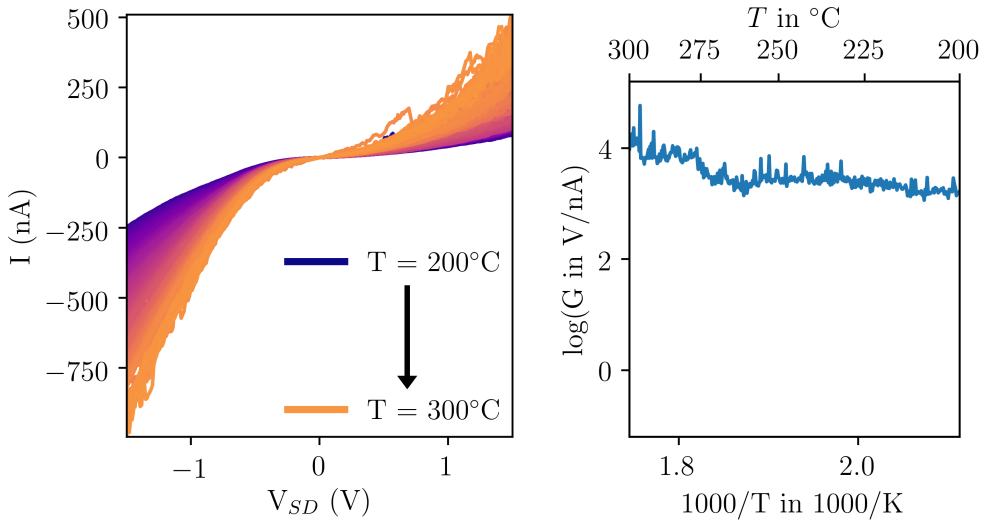

Figure 7.7: Step 6. Left: IVs recorded from 200°C to 300°C. Right: Arrhenius plot of the low bias conductance. A top axis is included for better readability.

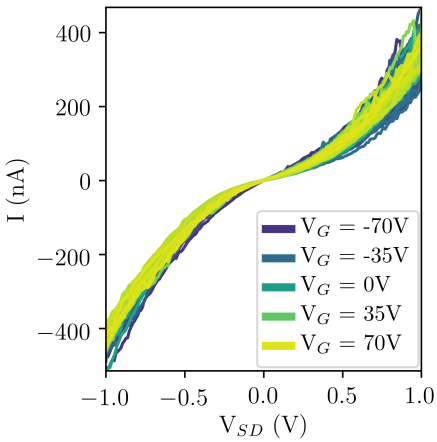

Figure 7.8: Step 7. Barristor behavior is completely lost at 300°C.

In order to make sure that no leakage current occurs between the backgate and the two terminals connecting graphene and diamond, we measured the current towards the backgate upon reaching 300°C and found that leakage currents to be absent, within the range of applied backgate voltages.

Next, the temperature was lowered from 300°C to 30°C. During that process the samples looses all its conductivity around 260°C. This can be observed as a sharp dip in the Arrhenius plot in the right plot of figure 7.9. Likewise, the left plot shows how the noisy IV traces decay towards zero with decreasing temperature. The signal only recovers after applying an elevated voltage of 3 V and shows a low noise level (high conductive orange trace in the left plot). The middle plot shows the remaining temperature range from 246°C to 30°C, where the conductivity follows a linear trend in the Arrhenius plot until 140°C. Below 140°C the conductance is below the noise level of the measurement setup.

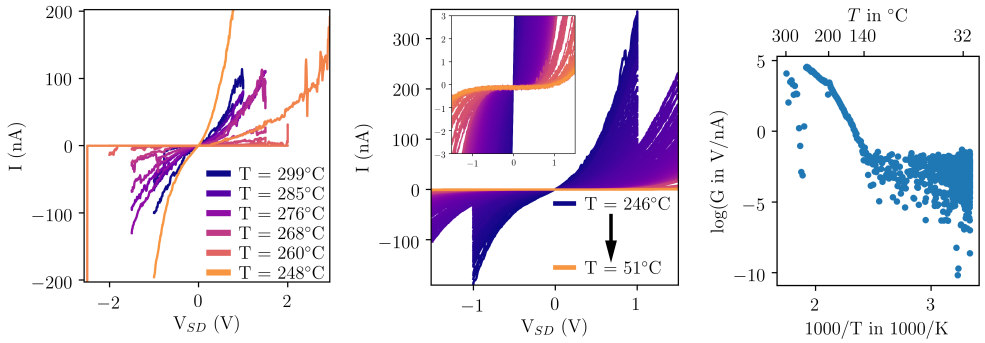

Figure 7.9: Step 8. IV traces from 300°C to 30°C in the left and middle plot. The right plot shows the Arrhenius figure with a dip around 260°C, where the samples looses its conductivity.

Such a behavior can be explained possibly in terms of thermally annealing the diamond structure, where a reconstruction of the lattice can occur. For a defect rich diamond structure, either the recovery of an insulating diamond lattice or graphitization of the diamond lattice has been reported [23] upon annealing in a temperature range around

300°C to 600°C [22], where activation energies of $\sim$ 0.7±0.1 eV have been extracted. See section 1.5 for further details.

Last but not least, the back gate dependence of IV traces has been measured at room temperature after one high temperature heat cycle, see figure 7.10. Only after zooming in a slight backgate dependence becomes visible as well as a diode behavior of the sample. Therefore, a slight barristor behavior is still observerd even after one high temperature heat cycle. For larger V_{SD}, the tunability of the Fermi level is not clearly visible anymore neither is the diode behavior. The diamond-on-graphene interface has degraded after a heat cycle. This could be due to thermal expansion of diamond and graphene as well as influence of the PMMA capping layer after it passes its glass transition temperature. Then, the adhesion between diamond and graphene becomes more loose and more susceptible to effects of thermal expansion of graphene, diamond, quartz or PMMA.

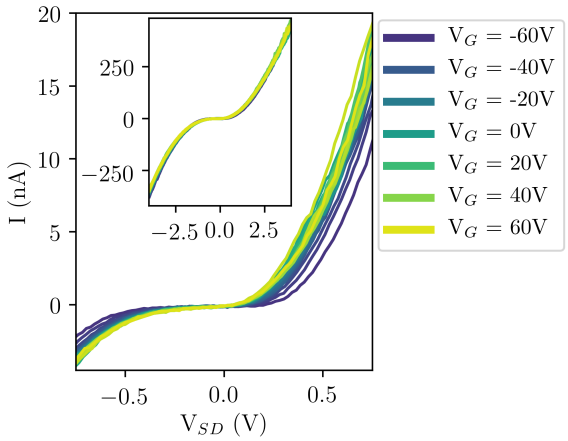

Figure 7.10: Step 9. Barristor behavior at 22°C after one high temperature cycle.

7.4 Conclusion

We have realized the first diamond-on-graphene barristor. Our barristor exhibits an optimal operation behavior between room temperature and 100°C. At room temperature the tunability of the Schottky barrier is the largest. With increasing temperature the tunability degrades and is eventually lost. At 100°C the diode characteristics of the diamond-graphene interface is the most pronounced. An unusual behavior occurs at 200°C, where the polarity of the diode changes directions. Our barristor device is not able to turn off the current completely to achieve high on off ratios for logic operations when tuning the backgate voltage. This will require future work as well as more detailed control of the temperature dependance on the sample properties. Our work layed out the first steps towards high temperature diamond and graphene based electronics for switching applications.

Bibliography

[1] K. S. Novoselov, D. Jiang, F. Schedin, T. J. Booth, V. V. Khotkevich, S. V. Morozov, and A. K. Geim. Two-dimensional atomic crystals. *Proceedings of the National Academy of Sciences*, 102(30):10451–10453, 2005.

[2] V. Meunier, A. G. Souza Filho, E. B. Barros, and M. S. Dresselhaus. Physical properties of low-dimensional sp^2-based carbon nanostructures. *Rev. Mod. Phys.*, 88:025005, May 2016.

[3] Jfmelero. Formation of hybrid atomic orbitals, https://www.quirkyscience.com/, 2014.

[4] Kevin Yager. Lattice:diamond, http://gisaxs.com/index.php, 2016.

[5] W. Saslow, T. K. Bergstresser, and Marvin L. Cohen. Band structure and optical properties of diamond. *Phys. Rev. Lett.*, 16:354–356, Feb 1966.

[6] Frank Herman, Richard L. Kortum, and Charles D. Kuglin. Energy band structure of diamond, cubic silicon carbide, silicon, and germanium. *International Journal of Quantum Chemistry*, 1(S1):533–566, 1967.

[7] R. M. Chrenko. Boron, the dominant acceptor in semiconducting diamond. *Phys. Rev. B*, 7:4560–4567, May 1973.

[8] R.G. Farrer. On the substitutional nitrogen donor in diamond. *Solid State Communications*, 7(9):685 – 688, 1969.

[9] Satoshi Koizumi and Mariko Suzuki. n-type doping of diamond. *physica status solidi (a)*, 203(13):3358–3366, 2006.

[10] Alan T. Collins. The fermi level in diamond. *Journal of Physics: Condensed Matter*, 14(14):3743–3750, Mar 2002.

[11] Dieter M. Gruen. Nanocrystalline diamond films. *Annual Review of Materials Science*, 29(1):211–259, 1999.

[12] James E. Butler and Anirudha V. Sumant. The cvd of nanodiamond materials. *Chemical Vapor Deposition*, 14(7-8):145–160, 2008.

[13] O.A. Williams. Nanocrystalline diamond. *Diamond and Related Materials*, 20(5):621 – 640, 2011.

[14] In-D. Jeon, Chang J. Park, Doh-Y. Kim, and Nong M. Hwang. Effect of methane concentration on size of charged clusters in the hot filament diamond cvd process. *Journal of Crystal Growth*, 223(1):6 – 14, 2001.

[15] R.E. Clausing, L. Heatherly, L.L. Horton, E.D. Specht, G.M. Begun, and Z.L. Wang. Textures and morphologies of chemical vapor deposited (cvd) diamond. *Diamond and Related Materials*, 1(5):411 – 415, 1992. Proceedings of the Second European Conference on Diamond, Diamond-like and Related Coatings.

[16] W. Zhu, P. C. Yang, and J. T. Glass. Oriented diamond films grown on nickel substrates. *Applied Physics Letters*, 63(12):1640–1642, 1993.

[17] H.-G. Busmann and I.V. Hertel. Vapour grown polycrystalline diamond films: Microscopic, mesoscopic and atomic surface structures. *Carbon*, 36(4):391 – 406, 1998.

[18] Ferrari Andrea Carlo and Robertson Jhon. Raman spectroscopy of amorphous, nanostructured, diamond-like carbon, and nanodiamond. *Philosophical Transactions of the Royal Society of London. Series A: Mathematical, Physical and Engineering Sciences*, 362:2477–2512, 2004.

[19] A. C. Ferrari and J. Robertson. Interpretation of raman spectra of disordered and amorphous carbon. *Phys. Rev. B*, 61:14095–14107, May 2000.

[20] Pierre Lespade, André Marchand, Michel Couzi, and Francis Cruege. Caracterisation de materiaux carbones par microspectrometrie raman. *Carbon*, 22(4):375 – 385, 1984.

[21] T.R. Anthony. Metastable synthesis of diamond. *Vacuum*, 41(4):1356 – 1359, 1990. Selected proceedings of the 11th international vacuum congress (IVC-11) 7th international conference on solid surfaces (ICSS-7).

[22] A. Reznik, V. Richter, and R. Kalish. Kinetics of the conversion of broken diamond (sp^3) bonds to graphitic (sp^2) bonds. *Phys. Rev. B*, 56:7930–7934, Oct 1997.

[23] C. Uzan-Saguy, C. Cytermann, R. Brener, V. Richter, M. Shaanan, and R. Kalish. Damage threshold for ion-beam induced graphitization of diamond. *Applied Physics Letters*, 67(9):1194–1196, 1995.

[24] A. V. Palnichenko, A. M. Jonas, J.-C. Charlier, A. S. Aronin, and J.-P. Issi. Diamond formation by thermal activation of graphite. *Nature*, 402(162), 1999.

[25] Luca Banszerus, Michael Schmitz, Stephan Engels, Jan Dauber, Martin Oellers, Federica Haupt, Kenji Watanabe, Takashi Taniguchi, Bernd Beschoten, and Christoph Stampfer. Ultrahigh-mobility graphene devices from chemical vapor deposition on reusable copper. *Science Advances*, 1(6), 2015.

[26] Oleg Martynov. *Production and Characterization of Carbon Nanoscrolls*. PhD thesis, UC Riverside, 2016.

[27] Seiichiro Matsumoto, Yoichiro Sato, Masayuki Tsutsumi, and Nobuo Setaka. Growth of diamond particles from methane-hydrogen gas. *Journal of Materials Science*, 17(11):3106–3112, Nov 1982.

[28] Mutsukazu Kamo, Yoichiro Sato, Seiichiro Matsumoto, and Nobuo Setaka. Diamond synthesis from gas phase in microwave plasma. *Journal of Crystal Growth*, 62(3):642 – 644, 1983.

[29] Yukio Saito, Shinpe Matsuda, and Shunsuke Nogita. Synthesis of diamond by decomposition of methane in microwave plasma. *Journal of Materials Science Letters*, 5(5):565–568, May 1986.

[30] Nong M. Hwang, Jun H. Hahn, and Duk Y. Yoon. Charged cluster model in the low pressure synthesis of diamond. *Journal of Crystal Growth*, 162(1):55 – 68, 1996.

[31] Nong M. Hwang and Duk Y. Yoon. Thermodynamic approach to the paradox of diamond formation with simultaneous graphite etching in the low pressure synthesis of diamond. *Journal of Crystal Growth*, 160(1):98 – 103, 1996.

[32] Nong Moon Hwang. *Non-Classical Crystallization of Thin Films and Nanostructures in CVD and PVD Processes, Ch.5 and 6*, volume 60 of *Springer Series in Surface Sciences*. Springer, Dordrecht, 2016.

[33] A. Glasner and S. Skurnik. A new mechanism for the crystallization and growth of ionic crystals, with special reference to kcl in the presence of pb2+ ions. *Israel Journal of Chemistry*, 6(1):69–72, 1968.

[34] Ichiro Sunagawa. Growth and morphology of diamond crystals under stable and metastable contitions. *Journal of Crystal Growth*, 99(1, Part 2):1156 – 1161, 1990.

[35] Nong-Moon Hwang and Dong-Kwon Lee. Charged nanoparticles in thin film and nanostructure growth by chemical vapour deposition. *Journal of Physics D: Applied Physics*, 43(48):483001, 2010.

[36] P. Blake, E. W. Hill, A. H. Castro Neto, K. S. Novoselov, D. Jiang, R. Yang, T. J. Booth, and A. K. Geim. Making graphene visible. *Applied Physics Letters*, 91(6):063124, 2007.

[37] Filippo Pizzocchero, Lene Gammelgaard, Bjarke S. Jessen, José M. Caridad, Lei Wang, James Hone, Peter Bøggild, and Timothy J. Booth. The hot pick-up technique for batch assembly of van der waals heterostructures. *Nature Communications*, 7:11894, Jun 2016.

[38] Joe Nabity. Nanometer pattern generation system, https://www.jcnabity.com/, 2019.

[39] R. Bogdanowicz, M. Ficek, M. Sobaszek, A. Nosek, Ł. Gołuński, J. Karczewski, A. Jaramillo-Botero, W. A. Goddard III, M. Bockrath, and T. Ossowski. Growth and isolation of large area boron-doped nanocrystalline diamond sheets: A route toward diamond-on-graphene heterojunction. *Advanced Functional Materials*, 29(3):1805242, 2019.

[40] C. V. Raman and K. S. Krishnan. A new type of secondary radiation. *Nature*, 121:501–502, Mar 1928.

[41] Nobel Media AB 2019. The nobel prize in physics 1930. nobelprize.org, 1930.

[42] Ewen Smith and Geoffrey Dent. *Modern Raman spectroscopy : a practical approach*. J. Wiley, 2005.

[43] A. C. Ferrari, J. C. Meyer, V. Scardaci, C. Casiraghi, M. Lazzeri, F. Mauri, S. Piscanec, D. Jiang, K. S. Novoselov, S. Roth, and A. K. Geim. Raman spectrum of graphene and graphene layers. *Phys. Rev. Lett.*, 97:187401, Oct 2006.

[44] A. C. Ferrari and D. M. Basko. Raman spectroscopy as a versatile tool for studying the properties of graphene. *Nature Nanotechnology*, 8:235–246.

[45] Diane S. Knight and William B. White. Characterization of diamond films by raman spectroscopy. *Journal of Materials Research*, 4(2):385–393, 1989.

[46] Shiv K. Sharma, H. K. Mao, P. M. Bell, and J. A. Xu. Measurement of stress in diamond anvils with micro-raman spectroscopy. *Journal of Raman Spectroscopy*, 16(5):350–352, 1985.

[47] S. Prawer, K. W. Nugent, and P. S. Weiser. Polarized raman spectroscopy of chemically vapor deposited diamond films. *Applied Physics Letters*, 65(18):2248–2250, 1994.

[48] A. C. Ferrari and J. Robertson. Origin of the $1150 - \mathrm{cm}^{-1}$ raman mode in nanocrystalline diamond. *Phys. Rev. B*, 63:121405, Mar 2001.

[49] C Q Wu, R T Fu, Z Q Li, and Y Kawazoe. An ab initio approach to phonon spectrum of trans-polyacetylene. *Journal of Physics: Condensed Matter*, 10(16):3695–3695, apr 1998.

[50] A. C. Ferrari and J. Robertson. Resonant raman spectroscopy of disordered, amorphous, and diamondlike carbon. *Phys. Rev. B*, 64:075414, Jul 2001.

[51] N. Wada, P.J. Gaczi, and S.A. Solin. "diamond-like" 3-fold coordinated amorphous carbon. *Journal of Non-Crystalline Solids*, 35-36:543 – 548, 1980.

[52] Steven Prawer and Robert J. Nemanich. Raman spectroscopy of diamond and doped diamond. *Philosophical Transactions of the Royal Society of London. Series A: Mathematical, Physical and Engineering Sciences*, 362(1824):2537–2565, 2004.

[53] Koichi Ushizawa, Kenji Watanabe, Toshihiro Ando, Isao Sakaguchi, Mikka Nishitani-Gamo, Yoichiro Sato, and Hisao Kanda. Boron concentration dependence of raman spectra on 100 and 111 facets of b-doped cvd diamond. *Diamond and Related Materials*, 7(11):1719 – 1722, 1998.

[54] G. Busch and H. Labhart. Üeber den mechanismus der elektrischen leitfähigkeit des siliciumcarbids. *Helv. phys. acta*, 14:463, 1946.

[55] N.F. Mott and W.D. Twose. The theory of impurity conduction. *Advances in Physics*, 10(38):107–163, 1961.

[56] H. Fritzsche. Electrical properties of germanium semiconductors at low temperatures. *Phys. Rev.*, 99:406–419, Jul 1955.

[57] H. Fritzsche. Resistivity and hall coefficient of antimony-doped germanium at low temperatures. *Journal of Physics and Chemistry of Solids*, 6(1):69 – 80, 1958.

[58] Nobel Media AB 2019. NobelPrize.org. The nobel prize in physics 1977, 1977.

[59] P. W. Anderson. Absence of diffusion in certain random lattices. *Phys. Rev.*, 109:1492–1505, Mar 1958.

[60] R. Dalichaouch, J.P. Armstrong, S. Schultz, P.M. Platzman, and S.L. McCall. Microwave localization by two-dimensional random scattering. *Nature*, 354:53–55, Nov 1991.

[61] R.L. Weaver. Anderson localization of ultrasound. *Wave Motion*, 12(2):129 – 142, 1990.

[62] H. Hu, A. Strybulevych, J.H. Page, S.E. Skipetrov, and B.A. van Tiggelen. Localization of ultrasound in a three-dimensional elastic network. *Nature*, 4:945–948, Oct 2008.

[63] Juliette Billy, Vincent Josse, Zhanchun Zuo, Alain Bernard, Ben Hambrecht, Pierre Lugan, David Clément, Laurent Sanchez-Palencia, Philippe Bouyer, and Alain Aspect. Direct observation of anderson localization of matter waves in a controlled disorder. *Nature*, 453:891–894, Jun 2008.

[64] Felix Bloch. Über die quantenmechanik der elektronen in kristallgittern. *Zeitschrift für Physik*, 52(7):555–600, Jul 1929.

[65] Issai Shlimak. *Is Hopping a Science?* World Scientific, 2015.

[66] Ferdinand Evers and Alexander D. Mirlin. Anderson transitions. *Rev. Mod. Phys.*, 80:1355–1417, Oct 2008.

[67] N. F. Mott. Conduction in non-crystalline materials. *The Philosophical Magazine: A Journal of Theoretical Experimental and Applied Physics*, 19(160):835–852, 1969.

[68] A. H. Clark. Electrical and optical properties of amorphous germanium. *Phys. Rev.*, 154:750–757, Feb 1967.

[69] P.A. Walley and A.K. Jonscher. Electrical conduction in amorphous germanium. *Thin Solid Films*, 1(5):367 – 377, 1968.

[70] P.A. Walley. Electrical conduction in amorphous silicon and germanium. *Thin Solid Films*, 2(4):327 – 336, 1968.

[71] N. F. Mott. *Charge transport in non-crystalline semiconductors*, pages 22–45. Springer Berlin Heidelberg, Berlin, Heidelberg, 1969.

[72] E. M. Hamilton. Variable range hopping in a non-uniform density of states. *The Philosophical Magazine: A Journal of Theoretical Experimental and Applied Physics*, 26(4):1043–1045, 1972.

[73] M. Pollak. A percolation treatment of dc hopping conduction. *Journal of Non-Crystalline Solids*, 11(1):1 – 24, 1972.

[74] N. Apsley and H. P. Hughes. Temperature-and field-dependence of hopping conduction in disordered systems. *The Philosophical Magazine: A Journal of Theoretical Experimental and Applied Physics*, 30(5):963–972, 1974.

[75] N. Apsley and H. P. Hughes. Temperature- and field-dependence of hopping conduction in disordered systems, ii. *The Philosophical Magazine: A Journal of Theoretical Experimental and Applied Physics*, 31(6):1327–1339, 1975.

[76] M Pollak and I Riess. A percolation treatment of high-field hopping transport. *Journal of Physics C: Solid State Physics*, 9(12):2339–2352, jun 1976.

[77] F. Maier, M. Riedel, B. Mantel, J. Ristein, and L. Ley. Origin of surface conductivity in diamond. *Phys. Rev. Lett.*, 85:3472–3475, Oct 2000.

[78] B. Massarani, J. C. Bourgoin, and R. M. Chrenko. Hopping conduction in semiconducting diamond. *Phys. Rev. B*, 17:1758–1769, Feb 1978.

[79] A.G. Zabrodskii and K.N. Zinov'eva. Low-temperature conductivity and metal-insulator transition in compensate n-ge. *Zh. Eksp. Teor. Fiz.*, 86:425–433, Feb 1984.

[80] A.O Caldeira and A.J Leggett. Quantum tunnelling in a dissipative system. *Annals of Physics*, 149(2):374 – 456, 1983.

[81] Hermann Grabert and Ulrich Weiss. Quantum tunneling rates for asymmetric double-well systems with ohmic dissipation. *Phys. Rev. Lett.*, 54:1605–1608, Apr 1985.

[82] Matthew P. A. Fisher and Alan T. Dorsey. Dissipative quantum tunneling in a biased double-well system at finite temperatures. *Phys. Rev. Lett.*, 54:1609–1612, Apr 1985.

[83] Nicolas Camus, Enderalp Yakaboylu, Lutz Fechner, Michael Klaiber, Martin Laux, Yonghao Mi, Karen Z. Hatsagortsyan, Thomas Pfeifer, Christoph H. Keitel, and Robert Moshammer. Experimental evidence for quantum tunneling time. *Phys. Rev. Lett.*, 119:023201, Jul 2017.

[84] U.S. Sainadh, H. Xu, X. Wang, A. Atia-Tul-Noor, W.C. Wallace, N. Douguet, A. Bray, I. Ivanov, K. Bartschat, A. Kheifets, R. T. Sang, and I.V. Litvinyuk. Attosecond angular streaking and tunnelling time in atomic hydrogen. *Nature*, 568:75–77, Apr 2019.

[85] Ulrich Weiss, Hermann Grabert, Peter Hänggi, and Peter Riseborough. Incoherent tunneling in a double well. *Phys. Rev. B*, 35:9535–9551, Jun 1987.

[86] Marc Bockrath, David H. Cobden, Jia Lu, Andrew G. Rinzler, Richard E. Smalley, Leon Balents, and Paul L. McEuen. Luttinger-liquid behaviour in carbon nanotubes. *Nature*, 397(6720):598–601, Feb 1999.

[87] A. N. Aleshin, H. J. Lee, Y. W. Park, and K. Akagi. One-dimensional transport in polymer nanofibers. *Phys. Rev. Lett.*, 93:196601, Nov 2004.

[88] E. Slot, M. A. Holst, H. S. J. van der Zant, and S. V. Zaitsev-Zotov. One-dimensional conduction in charge-density-wave nanowires. *Phys. Rev. Lett.*, 93:176602, Oct 2004.

[89] Jonathan D. Yuen, Reghu Menon, Nelson E. Coates, Ebinazar B. Namdas, Shinuk Cho, Scott T. Hannahs, Daniel Moses, and Alan J. Heeger. Nonlinear transport in semiconducting polymers at high carrier densities, June 2009.

[90] A. J. Kronemeijer, E. H. Huisman, I. Katsouras, P. A. van Hal, T. C. T. Geuns, P. W. M. Blom, S. J. van der Molen, and D. M. de Leeuw. Universal scaling in highly doped conducting polymer films. *Phys. Rev. Lett.*, 105:156604, Oct 2010.

[91] Kamal Asadi, Auke J. Kronemeijer, Tobias Cramer, L. Jan Anton Koster, Paul W. M. Blom, and Dago M. de Leeuw. Polaron hopping mediated by nuclear tunnelling in semiconducting polymers at high carrier density. *Nature Communications*, 4:1710, Apr 2013.

[92] Kyung Ho Kim, Samuel Lara-Avila, Hojin Kang, Hans He, Johnas Ekl f, Sung Ju Hong, Min Park, Kasper Moth-Poulsen, Satoshi Matsushita, Kazuo Akagi, Sergey Kubatkin, and Yung Woo Park. Apparent power law scaling of variable range hopping conduction in carbonized polymer nanofibers. *Scientific Reports*, 6, Nov 2016.

[93] G. L. Pearson and J. Bardeen. Electrical properties of pure silicon and silicon alloys containing boron and phosphorus. *Phys. Rev.*, 75:865–883, Mar 1949.

[94] Klaus Thonke. The boron acceptor in diamond. *Semiconductor Science and Technology*, 18(3):S20–S26, feb 2003.

[95] Peter Hanggi. Escape from a metastable state. *Journal of Statistical Physics*, 42(1):105–148, Jan 1986.

[96] Robert H. Windschitl Viktor T. Toth. A curious result, http://www.rskey.org/cms/index.php/the-library/11, 2019.

[97] A. J. Leggett, S. Chakravarty, A. T. Dorsey, Matthew P. A. Fisher, Anupam Garg, and W. Zwerger. Dynamics of the dissipative two-state system. *Rev. Mod. Phys.*, 59:1–85, Jan 1987.

[98] Hermann Grabert, Peter Olschowski, and Ulrich Weiss. Quantum decay rates for dissipative systems at finite temperatures. *Phys. Rev. B*, 36:1931–1951, Aug 1987.

[99] Svante Arrhenius. Über die Dissociationswärme und den Einfluss der Temperatur auf den Dissociationsgrad der Elektrolyte. *Z. f. Phys. Chem.*, pages 96–116, Jan 1889.

[100] H.A. Kramers. Brownian motion in a field of force and the diffusion model of chemical reactions. *Physica*, 7(4):284 – 304, 1940.

[101] Hermann Grabert and Ulrich Weiss. Crossover from thermal hopping to quantum tunneling. *Phys. Rev. Lett.*, 53:1787–1790, Nov 1984.

[102] James L. Skinner and Peter G. Wolynes. General kinetic models of activated processes in condensed phases. *The Journal of Chemical Physics*, 72(9):4913–4927, 1980.

[103] Ian Affleck. Quantum-statistical metastability. *Phys. Rev. Lett.*, 46:388–391, Feb 1981.

[104] P. Hänggi. Dissipative tunneling. *Zeitschrift für Physik B Condensed Matter*, 68(2):181–191, Jun 1987.

[105] A.I. Larkin and Yu. N. Ovchinnikov. Quantum-mechanical tunneling sith dissipation. the pre-exponential factor. *Zh. Eksp. Teor. Fiz*, 86:719–726, Feb 1984.

[106] Hermann Grabert, Ulrich Weiss, and Peter Hanggi. Quantum tunneling in dissipative systems at finite temperatures. *Phys. Rev. Lett.*, 52:2193–2196, Jun 1984.

[107] Curtis G. Callan and Sidney Coleman. Fate of the false vacuum. ii. first quantum corrections. *Phys. Rev. D*, 16:1762–1768, Sep 1977.

[108] J.S Langer. Theory of the condensation point. *Annals of Physics*, 41(1):108 – 157, 1967.

[109] S. Washburn, R. A. Webb, R. F. Voss, and S. M. Faris. Effects of dissipation and temperature on macroscopic quantum tunneling. *Phys. Rev. Lett.*, 54:2712–2715, Jun 1985.

[110] Hilmar Forkel. A Primer on instantons in QCD. 2000.

[111] L. Chua. Memristor-the missing circuit element. *IEEE Transactions on Circuit Theory*, 18(5):507–519, Sep. 1971.

[112] Parcly Taxel. Relations between the four fundamental electronic variables and devices that implement these relations, https://en.wikipedia.org/wiki/Memristor, 2013.

[113] Dmitri B. Strukov, Gregory S. Snider, Duncan R. Stewart, and R. Stanley Williams. The missing memristor found. *Nature*, 453(80), May 2008.

[114] Sascha Vongehr and Xiangkang Meng. The missing memristor has not been found. *Scientific Reports*, 5, 2015.

[115] Leon Chua. Resistance switching memories are memristors. *Applied Physics A*, 102(4):765–783, Mar 2011.

[116] G Dearnaley, A M Stoneham, and D V Morgan. Electrical phenomena in amorphous oxide films. *Reports on Progress in Physics*, 33(3):1129–1191, sep 1970.

[117] Yooichi Hirose and Haruo Hirose. Polarity-dependent memory switching and behavior of ag dendrite in ag-photodoped amorphous as2s3 films. *Journal of Applied Physics*, 47(6):2767–2772, 1976.

[118] A. Beck, J. G. Bednorz, Ch. Gerber, C. Rossel, and D. Widmer. Reproducible switching effect in thin oxide films for memory applications. *Applied Physics Letters*, 77(1):139–141, 2000.

[119] T. W. Hickmott. Low frequency negative resistance in thin anodic oxide films. *Journal of Applied Physics*, 33(9):2669–2682, 1962.

[120] A. Chen and M. Lin. Variability of resistive switching memories and its impact on crossbar array performance. In *2011 International Reliability Physics Symposium*, pages MY.7.1–MY.7.4, April 2011.

[121] M. Suri and V. Parmar. Exploiting intrinsic variability of filamentary resistive memory for extreme learning machine architectures. *IEEE Transactions on Nanotechnology*, 14(6):963–968, Nov 2015.

[122] I. Valov, E. Linn, S. Tappertzhofen, S. Schmelzer, J. van den Hurk, F. Lentz, and R. Waser. Nanobatteries in redox-based resistive switches require extension of memristor theory. *Nature Communications*, 4:1771, Apr 2013.

[123] Y. Chai, Y. Wu, K. Takei, H. Chen, S. Yu, P. C. H. Chan, A. Javey, and H. . P. Wong. Nanoscale bipolar and complementary resistive switching memory based on amorphous carbon. *IEEE Transactions on Electron Devices*, 58(11):3933–3939, Nov 2011.

[124] Abu Sebastian, Andrew Pauza, Christophe Rossel, Robert M Shelby, Arantxa Fraile Rodríguez, Haralampos Pozidis, and Evangelos Eleftheriou. Resistance switching at the nanometre scale in amorphous carbon. *New Journal of Physics*, 13(1):013020, jan 2011.

[125] Jianlong Xu, Dan Xie, Tingting Feng, Chenhui Zhang, Xiaowen Zhang, Pinggang Peng, Di Fu, He Qian, Tian ling Ren, and Litian Liu. Scaling-down characteristics of nanoscale diamond-like carbon based resistive switching memories. *Carbon*, 75:255 – 261, 2014.

[126] A K Ott, C Dou, U Sassi, I Goykhman, D Yoon, J Wu, A Lombardo, and A C Ferrari. Tetrahedral amorphous carbon resistive memories with graphene-based electrodes. *2D Materials*, 5(4):045028, sep 2018.

[127] Claudia A. Santini, Abu Sebastian, Chiara Marchiori, Vara Prasad Jonnalagadda, Laurent Dellmann, Wabe W. Koelmans, Marta D. Rossell, Christophe P. Rossel, and Evangelos Eleftheriou. Oxygenated amorphous carbon for resistive memory applications. *Nature Communications*, 6:8600, 2015.

[128] F. Zhuge, W. Dai, C. L. He, A. Y. Wang, Y. W. Liu, M. Li, Y. H. Wu, P. Cui, and Run-Wei Li. Nonvolatile resistive switching memory based on amorphous carbon. *Applied Physics Letters*, 96(16):163505, 2010.

[129] L. Dellmann, A. Sebastian, P. Jonnalagadda, C. A. Santini, W. W. Koelmans, C. Rossel, and E. Eleftheriou. Nonvolatile resistive memory devices based on hydrogenated amorphous carbon. In *2013 Proceedings of the European Solid-State Device Research Conference (ESSDERC)*, pages 268–271, Sep. 2013.

[130] Yi-Jiun Chen, Hsin-Lu Chen, Tai-Fa Young, Ting-Chang Chang, Tsung-Ming Tsai, Kuan-Chang Chang, Rui Zhang, Kai-Huang Chen, Jen-Chung Lou, Tian-Jian Chu, Jung-Hui Chen, Ding-Hua Bao, and Simon M. Sze. Hydrogen induced redox mechanism in amorphous carbon resistive random access memory. *Nanoscale Research Letters*, 9:52, Jan 2014.

[131] Akihito Sawa. Resistive switching in transition metal oxides. *Materials Today*, 11(6):28 – 36, 2008.

[132] Mohammad Baker, Jaoude Maguy Abi, Kumar Vikas, Al Homouz Dirar Mohammad, Nahla Heba Abu, Al-Qutayri Mahmoud, and Christoforou Nicolas. State of the art of metal oxide memristor devices. *Nanotechnology Reviews*, 5:311, Jan 2016.

[133] Y. Chen, K. Chang, T. Chang, H. Chen, T. Young, T. Tsai, R. Zhang, T. Chu, J. Ciou, J. Lou, K. Chen, J. Chen, J. Zheng, and S. M. Sze. Resistance switching induced by hydrogen and oxygen in diamond-like carbon memristor. *IEEE Electron Device Letters*, 35(10):1016–1018, Oct 2014.

[134] J. Gaudin, O. Peyrusse, J. Chalupský, M. Toufarová, L. Vyšín, V. Hájková, R. Sobierajski, T. Burian, Sh. Dastjani-Farahani, A. Graf, M. Amati, L. Gregoratti, S. P. Hau-Riege, G. Hoffmann, L. Juha, J. Krzywinski, R. A. London, S. Moeller, H. Sinn, S. Schorb, M. Störmer, Th. Tschentscher, V. Vorlíček, H. Vu, J. Bozek, and C. Bostedt. Amorphous to crystalline phase transition in carbon induced by intense femtosecond x-ray free-electron laser pulses. *Phys. Rev. B*, 86:024103, Jul 2012.

[135] Takeo Ohno, Tsuyoshi Hasegawa, Tohru Tsuruoka, Kazuya Terabe, James K. Gimzewski, and Masakazu Aono. Short-term plasticity and long-term potentiation mimicked in single inorganic synapses. *Nature Materials*, 10:591, June 2011.

[136] R.C. Atkinson and R.M. Shiffrin. Human memory: A proposed system and its control processes. volume 2 of *Psychology of Learning and Motivation*, pages 89 – 195. Academic Press, 1968.

[137] Sung Hyun Jo, Ting Chang, Idongesit Ebong, Bhavitavya B. Bhadviya, Pinaki Mazumder, and Wei Lu. Nanoscale memristor device as synapse in neuromorphic systems. *Nano Letters*, 10:1297–1301, Apr 2010.

[138] LEON CHUA, VALERY SBITNEV, and HYONGSUK KIM. Hodgkin–huxley axon is made of memristors. *International Journal of Bifurcation and Chaos*, 22(03):1230011, 2012.

[139] Heejun Yang, Jinseong Heo, Seongjun Park, Hyun Jae Song, David H. Seo, Kyung-Eun Byun, Philip Kim, InKyeong Yoo, Hyun-Jong Chung, and Kinam Kim. Graphene barristor, a triode device with a gate-controlled schottky barrier. *Science*, 336(6085):1140–1143, 2012.

[140] Antonis N. Andriotis, Giannis Mpourmpakis, Ernst Richter, and Madhu Menon. Surface conductivity of hydrogenated diamond films. *Phys. Rev. Lett.*, 100:106801, Mar 2008.

[141] A. O. Caldeira and A. J. Leggett. Influence of dissipation on quantum tunneling in macroscopic systems. *Phys. Rev. Lett.*, 46:211–214, Jan 1981.

[142] Isaac Abraham. The case for rejecting the memristor as a fundamental circuit element. *Scientific Reports*, 8(1), July 2018.

[143] M. M. Fogler and R. S. Kelley. Non-ohmic variable-range hopping transport in one-dimensional conductors. *Phys. Rev. Lett.*, 95:166604, Oct 2005.

[144] A. S. Rodin and M. M. Fogler. Apparent power-law behavior of conductance in disordered quasi-one-dimensional systems. *Phys. Rev. Lett.*, 105:106801, Sep 2010.

[145] A. S. Rodin and M. M. Fogler. Hopping transport in systems of finite thickness or length. *Phys. Rev. B*, 84:125447, Sep 2011.

[146] Kyung Ho Kim, Samuel Lara-Avila, Hojin Kang, Hans He, Johnas Ekl f, Sung Ju Hong, Min Park, Kasper Moth-Poulsen, Satoshi Matsushita, Kazuo Akagi, Sergey Kubatkin, and Yung Woo Park. Apparent power law scaling of variable range hopping conduction in carbonized polymer nanofibers. *Scientific Reports*, 6:1–8, Nov 2016.

[147] K. Shimakawa. Multiphonon hopping of electrons on defect clusters in amorphous germanium. *Phys. Rev. B*, 39:12933–12936, Jun 1989.

[148] Masatoshi Imada, Atsushi Fujimori, and Yoshinori Tokura. Metal-insulator transitions. *Rev. Mod. Phys.*, 70:1039–1263, Oct 1998.

[149] D. Belitz and T. R. Kirkpatrick. The anderson-mott transition. *Rev. Mod. Phys.*, 66:261–380, Apr 1994.

[150] Said Boutiche. Variable Range Hopping Conductivity: Case of the non-constant density of states. presented at: Solar Energy Conference, Sharjah, UAE. Feb. 19-22 (2001)., 2001.

[151] F. Cleri, P. Keblinski, L. Colombo, D. Wolf, and S. R. Phillpot. On the electrical activity of sp 2 -bonded grain boundaries in nanocrystalline diamond. *EPL (Europhysics Letters)*, 46(5):671, 1999.

Appendix A

Memristor

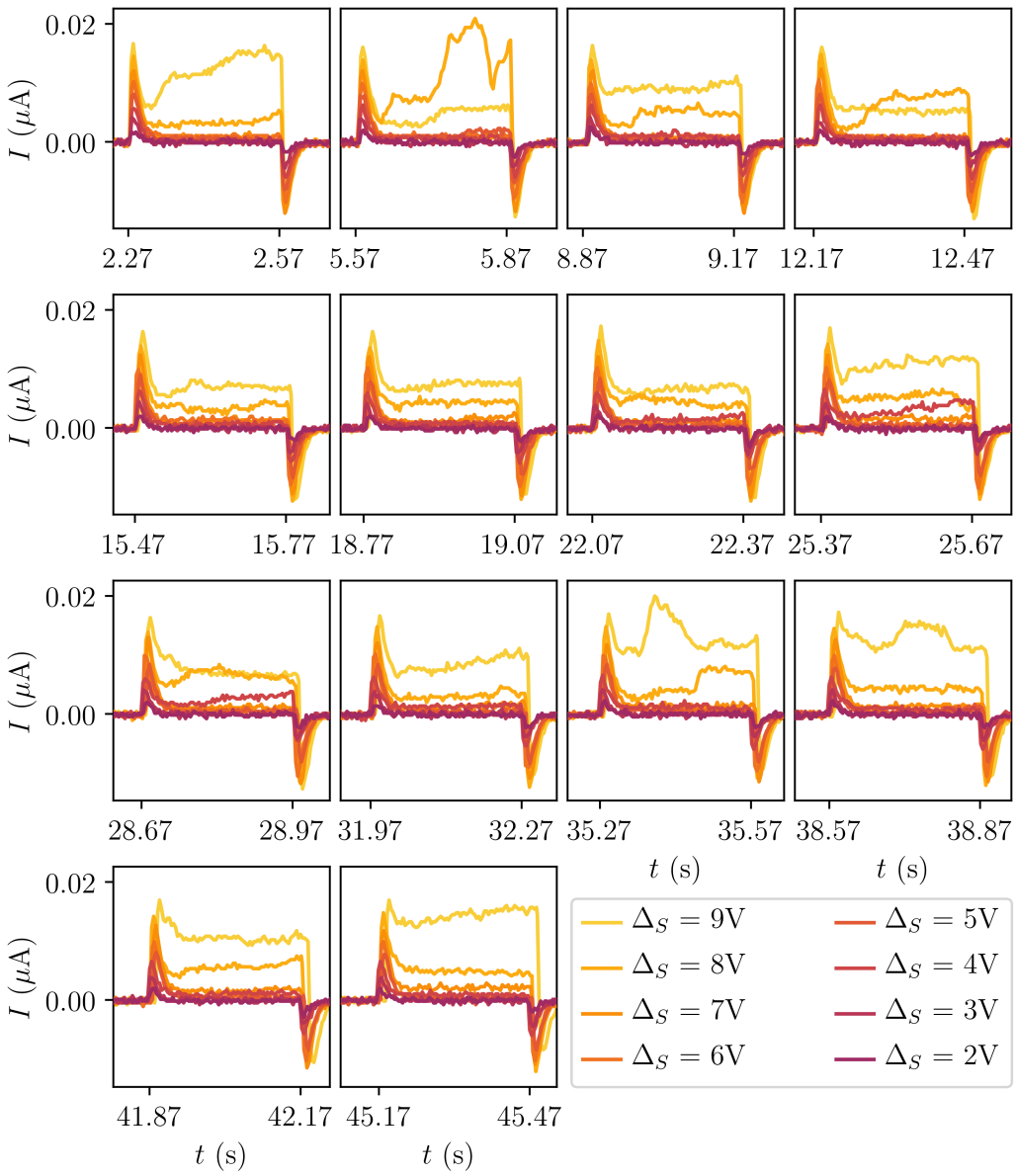

Figure A.1: Memristor response to a pulse train with varying pulse heights initially prepared in a high resistive state. Respond of the memristor to a single pulse from the pulse train applied in 6.12.

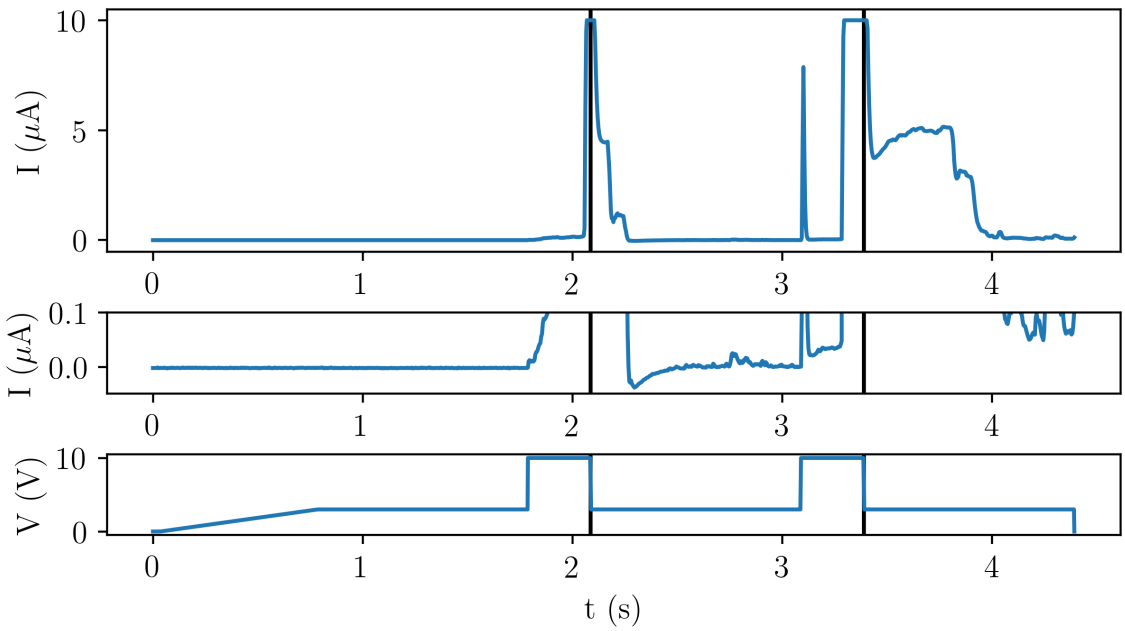

Figure A.2: Measurement showing that the dip is not due to dV/dt. The system is decaying from an unstable short term potentiation for both pulses. After the first pulse the current eventualls dips below zero. A clear separation in time is visible between the dip and dV/dt at the end of the pulse, excluding dV/dt at the end of the pulse as the origin of the dip.

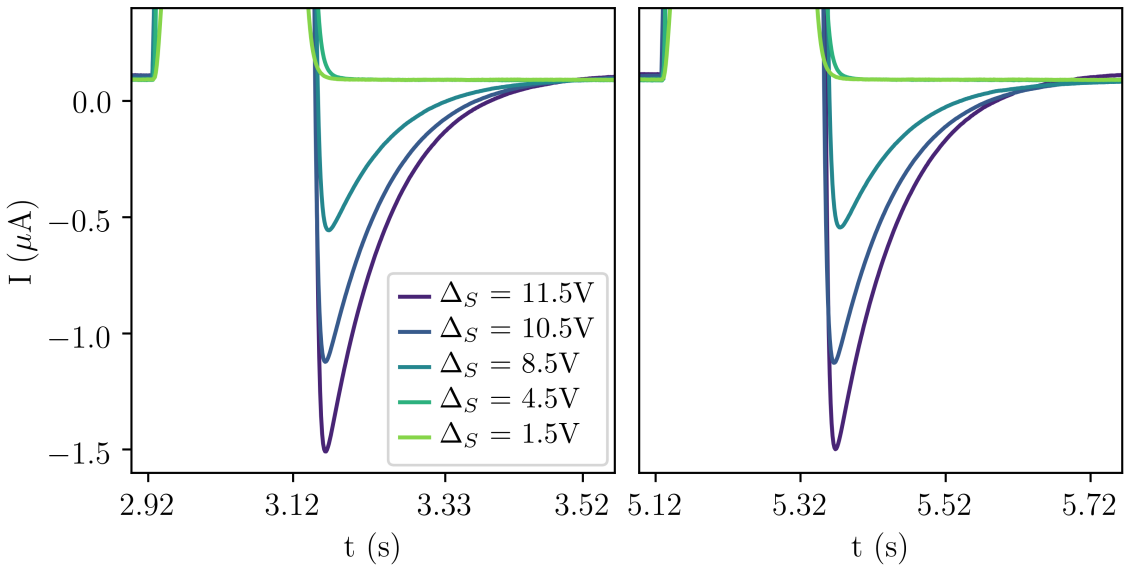

Figure A.3: Reproducibility of the current dipping below zero. Response of the memristor to the other two pulses of the pulse sequence shown in figure 6.18.